

**INTERPRETING IMPEDANCE SPECTRA OF
THIN-FILM ELECTROCHEMICAL CELLS:
A TWO-DIMENSIONAL NUMERICAL MODELING STUDY**

by

Benjamin E. McNealy

A dissertation submitted to the Faculty of the University of Delaware in partial fulfillment of the requirements for the degree of Doctor of Philosophy in Mechanical Engineering

Fall 2017

© 2017 Benjamin E. McNealy
All Rights Reserved

**INTERPRETING IMPEDANCE SPECTRA OF
THIN-FILM ELECTROCHEMICAL CELLS:
A TWO-DIMENSIONAL NUMERICAL MODELING STUDY**

by

Benjamin E. McNealy

Approved: _____
Ajay K. Prasad, Ph.D.
Chair of the Department of Mechanical Engineering

Approved: _____
Babatunde A. Ogunnaike, Ph.D.
Dean of the College of Engineering

Approved: _____
Ann L. Ardis, Ph.D.
Senior Vice Provost for Graduate and Professional Education

I certify that I have read this dissertation and that in my opinion it meets the academic and professional standard required by the University as a dissertation for the degree of Doctor of Philosophy.

Signed:

Joshua L. Hertz, Ph.D.
Professor in charge of dissertation

I certify that I have read this dissertation and that in my opinion it meets the academic and professional standard required by the University as a dissertation for the degree of Doctor of Philosophy.

Signed:

Suresh G. Advani, Ph.D.
Member of dissertation committee

I certify that I have read this dissertation and that in my opinion it meets the academic and professional standard required by the University as a dissertation for the degree of Doctor of Philosophy.

Signed:

Ajay K. Prasad, Ph.D.
Member of dissertation committee

I certify that I have read this dissertation and that in my opinion it meets the academic and professional standard required by the University as a dissertation for the degree of Doctor of Philosophy.

Signed:

Yushan Yan, Ph.D.
Member of dissertation committee

ACKNOWLEDGMENTS

This work would not have been possible without the contributions and support of many people: my advisor, Dr. Joshua Hertz; my committee members, Dr. Suresh Advani, Dr. Ajay Prasad, and Dr. Yushan Yan; my fellow research group members, Dr. Weida Shen, Dr. Ning Ye, Dr. Jun Jiang, and Phil Zandona; Lisa Katzmire, Letitia Toto, and Ann Connor from the Department of Mechanical Engineering office; all my friends and colleagues at UD; my parents and grandparents, my sister Grace, and the rest of my family; and of course Sophie le Blanc. Acknowledgment is also due to Air Products and Chemicals, Inc. for funding part of this work, which was much appreciated. Thank you to you all.

TABLE OF CONTENTS

LIST OF TABLES	viii
LIST OF FIGURES	ix
ABSTRACT	xvii

Chapter

1	INTRODUCTION	1
1.1	Solid State Electrochemistry	1
1.1.1	Solid Oxide Fuel Cells.....	1
1.1.2	Solid Electrolytes.....	2
1.1.3	Cathode Performance	3
1.1.3.1	Limiting and Co-Limiting Reaction Steps	5
1.1.3.2	The Triple Phase Boundary	8
1.1.3.3	Microelectrodes	10
1.1.4	The Pt/YSZ Model System.....	11
1.1.4.1	Bulk Versus Surface Path and the TPB	12
1.1.4.2	Limiting Processes.....	14
1.2	Impedance Spectroscopy	19
1.2.1	Equivalent Circuits and the Brick Layer Model	21
1.2.2	Constant Phase Elements.....	23
1.2.3	Issues Complicating the Use of Equivalent Circuits	26
1.2.3.1	Non-Ideal Microstructures.....	26
1.2.3.2	Ambiguity of Impedance Features	29
1.3	Modeling Solid State Electrochemical Systems	34
1.3.1	Electrolyte Impedance Models	35
1.3.2	Empirical Electrode Models	36
1.3.3	More Detailed Physicochemical Models.....	37

1.4	Summary of Existing Literature	42
2	PROCEDURE	45
2.1	General Modeling Approach	45
2.2	Grain Boundary Heterogeneity Study	47
2.2.1	Model Framework	47
2.2.2	Material Properties	52
2.2.3	Impedance Spectra.....	55
2.3	Phenomenological Electrode Modeling Study	56
2.3.1	Model Setup.....	56
2.3.2	Mesh	61
2.3.3	Fitting Procedure	61
2.3.4	Experimental.....	61
2.4	Diffusion-Reaction Electrode Modeling Study	62
2.4.1	Model Setup.....	63
2.4.2	Impedance.....	73
2.4.3	Mesh	74
2.4.4	Parameter Values.....	74
3	RESULTS	77
3.1	Grain Boundary Heterogeneity Study	77
3.1.1	Sample Results	77
3.1.2	Heterogeneous Conductivity	80
3.1.3	Heterogeneous Permittivity	84
3.1.4	Heterogeneous Conductivity and Permittivity	88
3.2	Phenomenological Electrode Modeling Study	90
3.2.1	Sample Results	90
3.2.2	Parametric Studies	93
3.3	Diffusion-Reaction Electrode Modeling Study	102
3.3.1	Sample Results	103
3.3.1.1	Impedance.....	103
3.3.1.2	IV Curve	104

3.3.1.3	Potential, Current, and Species Concentrations	106
3.3.2	Parametric Studies	109
3.3.2.1	Rate Constants	110
3.3.2.2	Diffusivity.....	120
3.3.2.3	Geometry	123
4	DISCUSSION.....	128
4.1	Grain Boundary Heterogeneity Study	128
4.1.1	Estimation of Average Grain Boundary Conductivity	128
4.1.2	Estimation of Average Grain Boundary Permittivity	131
4.1.3	Estimation of Heterogeneity.....	134
4.2	Phenomenological Electrode Modeling Study	135
4.2.1	Fitting	136
4.2.2	Validity of Eq. 67	145
4.2.3	Comparison to Equivalent Circuit Models	148
4.3	Diffusion-Reaction Model.....	149
4.3.1	Comparison Between Models.....	150
4.3.2	TPB Size.....	152
4.3.3	Rate Constants.....	157
5	CONCLUSIONS	160
5.1	Grain Boundary Heterogeneity Study	160
5.2	Microelectrode Model	161
5.3	Diffusion-Reaction Model.....	162
5.4	Future Work.....	163
	REFERENCES	165
Appendix		
A	MATLAB CODE	174
B	PERMISSIONS FOR REPRINTED MATERIAL.....	176

LIST OF TABLES

Table 1. Summary of experimental studies of the rate limiting step for Pt, O ₂ YSZ in the intermediate to high P_{O_2} range.	17
Table 2. Properties of the Pt/YSZ and Pt/GDC samples	62
Table 3. Model parameters	75
Table 4. Properties of thin film YSZ and GDC specimens as reported in the literature.....	138

LIST OF FIGURES

<p>Figure 1. Schematic of possible transport pathways (arrows) of oxygen vacancies (V_{O}^{2+}), electrons (e^-), oxygen gas (O_2), and adsorbed oxygen (O_{ad}) in the vicinity of the electrode-electrolyte-gas triple phase boundary, as well as possible reaction sites (numbered circles): (1) electrode-electrolyte interface, (2) triple phase boundary, (3) electrolyte bulk or electrolyte surface.....</p>	4
<p>Figure 2. Normalized concentration profiles predicted by (2) for the indicated values of the ratio k / D in m^{-2}.....</p>	7
<p>Figure 3. Current density predicted by (2) at the electrode-electrolyte interface as a function of surface exchange coefficient for the indicated values of the diffusion coefficient in m^2/s.....</p>	8
<p>Figure 4. Schematic illustrating the possible physical extent of the electrochemically active area, indicated by the shaded region. Three possible current paths are shown: (1) active area extending along electrode-electrolyte interface, (2) active area confined to TPB, and (3) active area extending along free electrolyte surface.....</p>	9
<p>Figure 5. Schematic of a thin film electrochemical cell with interdigitated microelectrodes.....</p>	11
<p>Figure 6. Simulated impedance spectrum for the electrical network shown in the inset. Circuit parameter values are $R_1 = 100 \Omega$, $R_2 = 250 \Omega$, $C_1 = 10$ pF, $C_2 = 100$ nF. $R_{DC} = 350 \Omega$ represents the resistance observed via a DC measurement, which conceals the separate contributions of R_1 and R_2.....</p>	20
<p>Figure 7. Simulated impedance spectrum obtained by solving Poisson's equation at varied frequency for a single repeat unit of an ideal "brick layer" polycrystal. A fit to the data using an ideal RC-RC equivalent circuit is also shown. Model parameters were $\sigma_{grain} = 10^{-4}$ S/m, $\sigma_{gb} = 10^{-7}$ S/m, $\epsilon_{grain} = \epsilon_{gb} = 25$, grain size = 10 μm, and grain boundary thickness = 1 nm (chosen so that the grain and grain boundary resistances are equal).....</p>	22

Figure 8. Hypothetical impedance spectrum for a polycrystalline electrolyte (squares), along with best-fit curves (dashed and solid lines) corresponding to the indicated equivalent circuits.	25
Figure 9. A distorted grain boundary semicircle resulting from an inhomogeneous grain size distribution in a sample with resistive grain boundaries. Figure reprinted from Reference 52 (© 2004 Kluwer Academic Publishers) with permission of Springer.	28
Figure 10. An ambiguous impedance spectrum caused by current constriction near the three phase boundary, with the true constricted electrolyte resistance indicated. Figure reprinted from Reference 50 (© 1998) with permission from Elsevier.	30
Figure 11. Sample impedance spectrum for a Pt/GDC specimen with an electrolyte thickness of 30 nm and electrode spacing and width of 25 μm . A possible equivalent circuit to fit the spectrum is shown in the inset.	32
Figure 12. Two possible mechanisms for the intermediate frequency arc: (a) low frequency current constriction at TPB; (b) low frequency current spreading at electrode-electrolyte interface.	32
Figure 13. Schematic of a thin film electrochemical cell with interdigitated microelectrodes. The 3D geometry (a) can be reduced to the 2D geometry (d) as shown by slicing along the dashed lines shown in parts (a), (b), and (c).	46
Figure 14. Schematic of the two-dimensional modeling domain illustrating the polycrystalline electrolyte geometry, key model parameters, and boundary conditions.	48
Figure 15. Selected probability density functions for distributions of (a) grain boundary conductivity (with population standard deviations S indicated) and (b) grain boundary permittivity used in the model (with the values of distribution parameter b indicated). Also included, below the PDF plots, are sample sets of grain boundary parameters corresponding to each of the distribution functions shown.	53
Figure 16. Model boundary conditions. All unlabeled boundaries obey the zero current condition given by (26).	57
Figure 17. Model domain. Thickness of surface and interfacial layers has been exaggerated for visibility.	64

Figure 18. (a) Current lines and (b) distributions of electrical potential in a specimen with heterogeneous grain boundary conductivity and homogeneous permittivity. The conductivity of each grain boundary in the sample is indicated in part (a) according to the scale shown on the right. Results are shown for three different frequencies.....	79
Figure 19. Representative impedance spectrum for a polycrystalline electrolyte with homogeneous grain boundary permittivity and heterogeneous grain boundary conductivity, along with the best fit parameters for the R-CPE equivalent circuit. The conductivity values follow a log-normal distribution with a standard deviation of 1. Frequencies of a few relevant data points are indicated.	80
Figure 20. Equivalent circuit parameter n_{gb} as a function of standard deviation of $\log(\sigma_{gb})$ for specimens with heterogeneous grain boundary conductivity. Grain size is indicated by symbol.....	81
Figure 21. Apparent grain boundary conductivity of specimens with heterogeneous grain boundary conductivity, calculated from the equivalent circuit parameter R_{gb} using (20), vs. standard deviation of $\log(\sigma_{gb})$. The mean grain boundary conductivity is indicated by a dashed line.	83
Figure 22. Apparent grain boundary permittivity of specimens with heterogeneous grain boundary conductivity, calculated from the equivalent circuit parameter Q_{gb} using (22), plotted as a function of the standard deviation of $\log(\sigma_{gb})$. The actual (homogeneous) value of ε_{gb} is indicated with a dashed line.	84
Figure 23. Equivalent circuit parameter n_{gb} as a function of $\varepsilon_{ideal} - \varepsilon_{mean}$, a measure of the spread of ε_{gb} , for specimens with heterogeneous grain boundary permittivity. Results are shown for three different grain sizes, indicated by symbol.....	85
Figure 24. Apparent grain boundary conductivity of specimens with heterogeneous grain boundary permittivity, calculated from the equivalent circuit parameter R_{gb} using (20), vs. $\varepsilon_{ideal} - \varepsilon_{mean}$, a measure of the spread of ε_{gb} . The actual (homogeneous) grain boundary conductivity is indicated by a dashed line.	86
Figure 25. Apparent grain boundary permittivity of specimens with heterogeneous grain boundary permittivity, calculated from the equivalent circuit parameter Q_{gb} using (22), vs. $\varepsilon_{ideal} - \varepsilon_{mean}$, a measure of the spread of ε_{gb} . The mean grain boundary permittivity is indicated by a dashed line.	88

Figure 26. Grain boundary impedance arcs for four related cases: homogeneous σ_{gb} and ϵ_{gb} , heterogeneous ϵ_{gb} , heterogeneous σ_{gb} , and heterogeneous σ_{gb} and ϵ_{gb} . The CPE exponent n_{gb} obtained from equivalent circuit fitting in each case is indicated.	89
Figure 27. Impedance response predicted by the model for a 25 nm film at 700°C with $L_{ode} = L_s = 12.5 \mu\text{m}$, $\sigma = 10^{-5} \text{ S/cm}$, $J_0 = 10^{-4} \text{ mA/cm}^2$, $C_{DL} = 100 \mu\text{F/cm}^2$, and $\epsilon = 10$. The intermediate frequency region is enlarged in the inset. The frequencies of a few key points are indicated.	91
Figure 28. Contours of electrical potential in mV, indicated by black and white color scale, in the electrode, electrolyte, and substrate at $f = 0.126 \text{ Hz}$ and 31.6 Hz . The vertical dimension has been exaggerated and the substrate truncated to aid visualization. The distribution of current in the electrolyte is also shown via solid lines.	92
Figure 29. Low and intermediate frequency portions of the impedance spectra for specimens with the indicated electrolyte thickness and $L_{ode} = L_s = 12.5 \mu\text{m}$. The figure has been cropped and re-zeroed on the real axis in order to ignore the high frequency impedance arc. Note change of scale for the 1 nm specimen.	94
Figure 30. Resistance R_2 vs. L_{yte} / h for various values of h , with $\sigma = 10^{-3} \text{ S/m}$ and $J_0 = 10^{-4} \text{ mA/cm}^2$. The electrode finger width and spacing are equal. The dashed line is a plot of the semi-empirical expression indicated.	97
Figure 31. Impedance spectra for the three indicated values of L_{ode} / L_{yte} (i.e., the ratio of the electrolyte surface that is covered by the electrode).	98
Figure 32. Resistance R_2 vs. L_{ode} / L_{yte} for three different electrolyte aspect ratios, with $L_{yte} = 10 \mu\text{m}$ (filled symbols) and $25 \mu\text{m}$ (open symbols). The semi-empirical linear expression shown is also plotted for each electrolyte aspect ratio as indicated via dashed line.	99
Figure 33. Impedance spectra for specimens with the indicated values of exchange current density in $\mu\text{A/cm}^2$	100
Figure 34. Value of R_2 as a function of exchange current density J_0 for various values of electrolyte conductivity in S/cm. The specimen dimensions are $L_{ode} = 12.5 \mu\text{m}$, $L_s = 12.5 \mu\text{m}$, and $h = 25 \text{ nm}$. The linear expression for R_2 shown in the upper right is plotted for each value of σ , indicated via dashed line. The condition $R_{ode} > R_{yte}$ is satisfied within the shaded region.	101

Figure 35. R_2 as a function of resistivity $1 / \sigma$ for several different values of exchange current density in mA/cm^2 . The specimen dimensions are $L_{ode} = L_s = 12.5 \mu\text{m}$ and $h = 25 \text{ nm}$. The dashed line is a plot of the linear expression for R_2 indicated.....	102
Figure 36. Simulated Nyquist and Bode impedance plots for a specimen with $k_{-1}^0 = 10 \text{ m}^3/\text{mol}\cdot\text{s}$, $k_2^0 = 4.1 \times 10^{-7} \text{ mol}\cdot\text{s}/(\text{kg}\cdot\text{m}^2)$, and $h_{act} = 1 \text{ nm}$	104
Figure 37. Simulated IV curve for a specimen with $k_{-1}^0 = 10 \text{ m}^3/\text{mol}\cdot\text{s}$, $k_2^0 = 4.1 \times 10^{-7} \text{ mol}\cdot\text{s}/(\text{kg}\cdot\text{m}^2)$, and $h_{act} = 1 \text{ nm}$. The electrode length is $L_{ode} = 25 \text{ nm}$	106
Figure 38. Potential distribution and representative current streamlines for the specimen modeled in Figure 36 at the frequencies indicated. The scale of the potential distribution is given in millivolts.	107
Figure 39. Centerline ABD through the surface layer and TPB, indicated by dashed line.	109
Figure 40. Concentration of adsorbed oxygen along the centerline ABD (shown in Figure 39) for the values of k_2^0 given in $\text{mol}\cdot\text{s}/(\text{kg}\cdot\text{m}^2)$ under cathodic DC polarization with $\eta = -1 \text{ mV}$. The dashed line marks the bend at the electrode corner B , and the shaded area denotes the TPB.	109
Figure 41. Simulated impedance spectra for $k_{-1}^0 = 10 \text{ m}^3/\text{mol}\cdot\text{s}$ and four different values of k_2^0 in $\text{mol}\cdot\text{s}/(\text{kg}\cdot\text{m}^2)$, plotted on a logarithmic scale. The frequency range is $10^{-2} \text{ Hz} \leq f \leq 10^9 \text{ Hz}$	111
Figure 42. Simulated impedance spectra for $k_{-1}^0 = 0.1 \text{ m}^3/\text{mol}\cdot\text{s}$ and three different values of k_2^0 in $\text{mol}\cdot\text{s}/(\text{kg}\cdot\text{m}^2)$, plotted on a logarithmic scale. The frequency range is $10^{-2} \text{ Hz} \leq f \leq 10^9 \text{ Hz}$	113
Figure 43. Simulated impedance spectra for $k_{-1}^0 = 1000 \text{ m}^3/\text{mol}\cdot\text{s}$ and five different values of k_2^0 in $\text{mol}\cdot\text{s}/(\text{kg}\cdot\text{m}^2)$, plotted on a linear scale. The frequency range is $10^{-2} \text{ Hz} \leq f \leq 10^9 \text{ Hz}$	114
Figure 44. Simulated impedance spectra for $k_2^0 = 4.1 \times 10^{-9} \text{ mol}\cdot\text{s}/(\text{kg}\cdot\text{m}^2)$ and three different values of k_{-1}^0 in $\text{m}^3/\text{mol}\cdot\text{s}$, plotted on a logarithmic scale. The frequency range is $10^{-2} \text{ Hz} \leq f \leq 10^9 \text{ Hz}$	117
Figure 45. Simulated impedance spectra for $k_2^0 = 4.1 \times 10^{-7} \text{ mol}\cdot\text{s}/(\text{kg}\cdot\text{m}^2)$ and three different values of k_{-1}^0 in $\text{m}^3/\text{mol}\cdot\text{s}$, plotted on a logarithmic scale. The frequency range is $10^{-2} \text{ Hz} \leq f \leq 10^9 \text{ Hz}$	118

- Figure 46. Quasi-DC resistance R_{total} as a function of the reaction rate constants k_{-1}^0 (in $\text{m}^3/\text{mol}\cdot\text{s}$) and k_2^0 (in $\text{mol}\cdot\text{s}/(\text{kg}\cdot\text{m}^2)$) for a specimen with $L_{yte} = 50$ nm, $L_{ode} = 25$ nm, $h_{yte} = 10$ nm, and $h_{act} = 1$ nm..... 119
- Figure 47. Simulated impedance spectra for three specimens with $k_{-1}^0 = 10$ $\text{m}^3/\text{mol}\cdot\text{s}$, $k_2^0 = 4.1\times 10^{-7}$ $\text{mol}\cdot\text{s}/(\text{kg}\cdot\text{m}^2)$, and the respective values of D_{Oad} indicated (in m^2/s). The geometric parameters are $L_{yte} = 50$ nm, $L_{ode} = 25$ nm, $h_{yte} = 10$ nm, and $h_{act} = 1$ nm..... 121
- Figure 48. Simulated impedance spectra for three specimens with $k_{-1}^0 = 10$ $\text{m}^3/\text{mol}\cdot\text{s}$, $k_2^0 = 0.41$ $\text{mol}\cdot\text{s}/(\text{kg}\cdot\text{m}^2)$, and the respective values of D_{Oad} indicated (in m^2/s). The geometric parameters are $L_{yte} = 50$ nm, $L_{ode} = 25$ nm, $h_{yte} = 10$ nm, and $h_{act} = 1$ nm..... 122
- Figure 49. Normalized adsorption rate along the centerline of the electrode surface layer and TPB (see Figure 39) for a specimen with $k_{-1}^0 = 10$ $\text{m}^3/\text{mol}\cdot\text{s}$, $D_{Oad} = 10^{-12}$ m^2/s , and the indicated values of k_2^0 in $\text{mol}\cdot\text{s}/(\text{kg}\cdot\text{m}^2)$ under a cathodic DC polarization of $\eta = -1$ mV. The dashed line indicates the bend at the electrode corner B , and the shaded area represents the TPB. The maximum adsorption rates in $\text{mol}/(\text{m}^3\cdot\text{s})$ are 3.1×10^5 for $k_2^0 = 4.1\times 10^{-7}$ and 2.8×10^7 for $k_2^0 = 0.41$ 123
- Figure 50. Impedance spectra for three specimens with $k_{-1}^0 = 10$ $\text{m}^3/\text{mol}\cdot\text{s}$, $k_2^0 = 4.1\times 10^{-7}$ $\text{mol}\cdot\text{s}/(\text{kg}\cdot\text{m}^2)$, and the respective values of h_{yte} indicated. The electrolyte dimensions are $L_{yte} = 50$ nm and $L_{ode} = 25$ nm for all specimens. 125
- Figure 51. Impedance spectra for three specimens with $k_{-1}^0 = 10$ $\text{m}^3/\text{mol}\cdot\text{s}$, $k_2^0 = 4.1\times 10^{-7}$ $\text{mol}\cdot\text{s}/(\text{kg}\cdot\text{m}^2)$, and the respective values of L_{ode} indicated. The electrolyte dimensions are $L_{yte} = 50$ nm and $h_{yte} = 10$ nm for all specimens. 126
- Figure 52. Electrode resistance vs. finger width ratio for two different values of k_2^0 . The electrolyte dimensions are $L_{yte} = 50$ nm and $h_{yte} = 10$ nm, and $k_{-1}^0 = 10$ $\text{m}^3/\text{mol}\cdot\text{s}$ for all specimens..... 127
- Figure 53. Apparent grain boundary conductivity calculated from (20) vs. actual mean conductivity for all specimens. Data are shown for samples with heterogeneous conductivity and homogeneous permittivity (circles), heterogeneous permittivity and homogeneous conductivity (triangles), and both heterogeneous conductivity and permittivity (squares). The mean grain boundary conductivity is indicated by a dashed line..... 129

Figure 54. Percent error in apparent conductivity calculated from (20) vs. equivalent circuit exponent n_{gb} . Data are shown for samples with heterogeneous conductivity and homogeneous permittivity (circles), heterogeneous permittivity and homogeneous conductivity (triangles), and both heterogeneous conductivity and permittivity (squares). 130

Figure 55. Apparent grain boundary permittivity vs. actual mean permittivity for all specimens. Apparent permittivity was calculated using one of three capacitance expressions: the assumption $C_{gb} = Q_{gb}$ (triangles), Brug's equation (9) (circles), and a new empirical equation (70) (Xs). The mean permittivity is indicated by a dashed line. 132

Figure 56. Equivalent circuit parameter n_{gb} vs. (a) standard deviation of $\log(\sigma_{gb})$ and (b) $\epsilon_{ideal} - \epsilon_{mean}$, a measure of the spread of ϵ_{gb} , for all samples with 1 μm grains. These samples include those with heterogeneous conductivity only (circles), heterogeneous permittivity only (triangles), and both heterogeneous conductivity and permittivity (squares). 135

Figure 57. Bode and Nyquist plots of the impedance of a Pt/GDC specimen at 652°C, along with the model fit. 137

Figure 58. Arrhenius plot of electrolyte conductivity for (a) YSZ and (b) GDC thin films obtained by model fitting, compared to literature results for similar thin film specimens as well as bulk ceramics. The thin film specimens selected from the literature are compiled in Table 4. The bulk conductivities were obtained by linear regression of several sets of data as explained in the text. The activation energy obtained from the model results, as well as the bulk activation energy, is indicated in each plot. 139

Figure 59. Arrhenius plot of exchange current density for Pt electrodes on (a) YSZ and (b) GDC. Model fit results from the present work are shown along with values reported previously in the literature. 141

Figure 60. Resistance scaling factor K as a function of aspect ratio h / L_{ode} for the case where $R_{ode} \gg R_{yte}$. Results are shown for three different values of the electrode spacing ratio L_s / L_{ode} . Also shown are plots of the same quantity calculated using (72) and (73). The value $K = 1/3$ is indicated by a dashed line. 146

Figure 61. Percent error in intermediate frequency resistance (R_2) estimate calculated using (67) as a function of the dimensionless number S 147

Figure 62. Simulated impedance spectrum generated using model C with $k_{-1}^0 = 10 \text{ m}^3/\text{mol}\cdot\text{s}$ and $k_2^0 = 4.1 \times 10^{-7} \text{ mol}\cdot\text{s}/(\text{kg}\cdot\text{m}^2)$ compared to spectrum generated using model B with $\sigma = 4.3 \times 10^{-4} \text{ S/cm}$, $\varepsilon = 37$, $C_{DL} = 6400 \text{ }\mu\text{F/cm}^2$, and $J_0 = 236 \text{ mA/cm}^2$	151
Figure 63. Two different formulations of the TPB extension: (a) single-parameter and (b) two-parameter.	153
Figure 64. Simulated impedance spectra for $k_{-1}^0 = 10 \text{ m}^3/\text{mol}\cdot\text{s}$, $k_2^0 = 4.1 \times 10^{-7} \text{ mol}\cdot\text{s}/(\text{kg}\cdot\text{m}^2)$, and three different values of the TPB size h_{act} as indicated. The TPB geometry has been defined as shown in Figure 63a. The shaded portion of the spectrum is enlarged in the inset to clarify the intermediate frequency behavior.....	154
Figure 65. Simulated impedance spectra for $k_{-1}^0 = 1 \text{ m}^3/\text{mol}\cdot\text{s}$, $k_2^0 = 4.1 \times 10^{-7} \text{ mol}\cdot\text{s}/(\text{kg}\cdot\text{m}^2)$, and three different values of the TPB size h_{act} as indicated. The TPB geometry has been defined as shown in Figure 63b.....	156
Figure 66. The resistance ratio R_2 / R_1 vs. k_2^0 for the indicated values of k_{-1}^0 , in $\text{m}^3/\text{mol}\cdot\text{s}$. The reaction can be considered to be jointly limited by adsorption and charge transfer within the region indicated by dashed lines.	158

ABSTRACT

Thin film solid state electrochemical systems have numerous applications in clean/alternative energy technologies including fuel cells, batteries, advanced solar cells, and other devices. However, enhancing the performance of such devices is often hindered by an incomplete understanding of the underlying electrochemistry. Here, two-dimensional continuum numerical modeling was used to simulate the electrochemistry of thin film cells with a goal of aiding the researcher in interpreting experimental results for such cells—particularly electrochemical impedance spectroscopy (EIS). EIS is often useful in understanding the electrochemical processes governing a cell's overall performance, but EIS spectra can be misleading and difficult to interpret.

Three related models were developed to clarify various aspects of the thin film cell behavior. First, the effect of grain boundary heterogeneity in polycrystalline electrolytes was studied by simulating grain boundaries with randomly assigned conductivity and/or permittivity according to pre-chosen distributions. The study revealed that EIS is capable of characterizing the mean grain boundary conductivity within 30% using a simple equivalent circuit model, and estimating the variation between individual grain boundaries is also possible in some cases.

In the second part of the study, the electrolyte model was extended to also include a phenomenological description of the electrode reaction based on the Butler-Volmer equation. The model was validated by fitting previously reported impedance

spectra obtained for Pt/YSZ and Pt/GDC cells and was able to reproduce all salient features. Further, the model was able to capture a previously unexplained intermediate frequency arc seen in the experimental results. A parametric study enabled the mechanism of the intermediate frequency feature to be identified as a spreading resistance in the electrolyte that vanishes at high frequencies due to low-impedance dielectric transport of current across the electrode-electrolyte interface.

In the last part of the work, a physicochemical model based on the Poisson-Nernst-Planck equations was developed for the Pt/YSZ interface. The model included adsorption/desorption, diffusion, and charge transfer, and was able to produce qualitatively realistic impedance spectra matching those obtained from the phenomenological model. A parametric study demonstrated that the physical processes considered may all influence the overall impedance, and the idea of a single limiting step at the Pt/YSZ interface is inaccurate. Practical upper bounds on the reaction rate constants were established based on the model results. With enhanced computing power, necessitated by the computational cost of full-scale modeling, the model will be of great use in better interpreting the experimentally obtained impedance spectra.

Chapter 1

INTRODUCTION

1.1 Solid State Electrochemistry

In recent decades, solid state electrochemistry has become important in a number of vital areas including many of the most promising clean and alternative energy technologies. Compared to traditional aqueous electrochemistry, solid state systems are more thermally and mechanically robust, do not suffer from liquid containment or leakage issues, and are well suited to thin-film processing techniques, allowing practical fabrication of microscale devices.¹ With these advantages, solid electrochemical systems have important applications in advanced energy technologies including batteries, fuel cells, and advanced solar cells, as well as other areas including chemical sensors, “smart windows,” and other devices. The continuing study and improvement of such systems is thus an area of great importance.

1.1.1 Solid Oxide Fuel Cells

While all solid state electrochemical devices operate under similar principles, and the results gained herein will be useful across multiple areas, the present work is focused specifically on solid oxide fuel cells (SOFCs). Like other types of fuel cell, SOFCs are a promising alternative/clean energy technology which operate on the principle of converting the chemical energy in a fuel (often hydrogen) directly to electricity via electrochemical reaction. Some of the advantages of fuel cells include high efficiency and few moving parts relative to conventional energy sources. In

addition, they produce no harmful emissions if pure hydrogen fuel is used. If the hydrogen is produced using a clean, renewable energy source (e.g. wind, solar, etc.), fuel cells have the potential to be a completely green technology. Additionally, SOFCs share the advantages inherent to solid state devices: mechanical durability, suitability to microscale fabrication techniques, and the lack of leakage issues associated with other types of fuel cell (which typically use liquid or hydrated polymer electrolytes).

The key characteristic of solid oxide fuel cells is the use of a solid ceramic electrolyte which conducts oxygen ions (O^{2-}). Because conventional SOFC electrolyte materials such as yttria stabilized zirconia (YSZ) have a high thermal activation barrier to oxide ion conduction, SOFCs are generally operated at temperatures greater than 500°C . This makes them primarily of use for stationary power applications, though lower-temperature cells suitable for other application areas have also been developed.² The ability to fabricate devices using thin film processing techniques like sputtering, chemical vapor deposition, etc. also makes SOFCs of interest to microscale power applications.

1.1.2 Solid Electrolytes

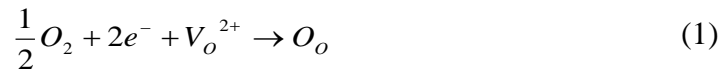
The primary metric of the SOFC electrolyte is its ionic conductivity, or ability to conduct oxygen ions. High electrolyte conductivity is essential to reducing Ohmic losses in the fuel cell. The most common SOFC electrolyte material is YSZ, which is zirconia (ZrO_2) doped with 8–10 mol% of yttria (Y_2O_3) in order to introduce oxygen vacancies into the zirconia crystal lattice. The vacancies allow conduction of oxygen ions through the electrolyte. The conductivity of YSZ is comparable to conventional liquid electrolytes at high temperatures ($> 700^{\circ}\text{C}$), but much lower at the reduced temperatures necessary for smaller-scale SOFC applications. Many other electrolyte

materials have been developed, including other types of doped zirconia, bismuth oxide, and ceria, particularly gadolinium doped ceria (GDC), and more exotic oxides like LaSrGaMgO (LSGM). Some of these materials have improved ionic conductivity compared to YSZ, especially at lower temperatures, but may incur tradeoffs on mechanical stability or chemical and/or thermal compatibility with the other fuel cell materials.²

Bulk ionic conductivity is not the only property relevant to the electrolyte performance. Most SOFC electrolyte materials are polycrystalline, especially when fabricated using processes like sputtering. Therefore grain boundary effects can influence the overall electrolyte properties, often significantly. For example, the resistance associated with conduction across grain boundaries is often as large as or larger than that of the bulk material. Alternatively, in some cases grain boundaries may offer a less resistive conduction path compared to the bulk due to increased free volume, and so conductivity may be improved by the presence of grain boundaries. Due to the importance of these effects, researchers often wish to characterize the grain boundary properties as well as those of the bulk electrolyte.

1.1.3 Cathode Performance

Electrolyte losses can contribute significantly to the overall performance of SOFCs, but are typically dwarfed by losses associated with the electrode reactions. In particular, the cell performance is often limited by the oxygen reduction reaction, which occurs at the cathode. This makes cathode material selection particularly important. However, efforts toward optimizing SOFC cathodes are complicated by the fact that their kinetics are complex and not yet fully understood. In a solid oxide fuel cell, the cathode reaction can be expressed as



where O_2 represents oxygen gas, e^- are electrons, V_o^{2+} is an oxygen vacancy, and O_o denotes a filled oxygen site. In general, this reaction involves some or all of the following mechanisms: (1) transport of oxygen vacancies in the electrolyte, (2) diffusion of oxygen in the gas phase, (3) conduction of electrons in the electrode, (4) oxygen dissociation, (5) adsorption of oxygen on the electrode and/or electrolyte surfaces, (6) diffusion of adsorbed oxygen on the electrode and/or electrolyte surfaces, (7) oxygen diffusion in the electrode and/or electrolyte bulk, (8) transport of oxygen vacancies in the electrode, (9) conduction of electrons in the electrolyte, and (10) the charge transfer reaction itself.³ These possible reaction steps are illustrated schematically in Figure 1.

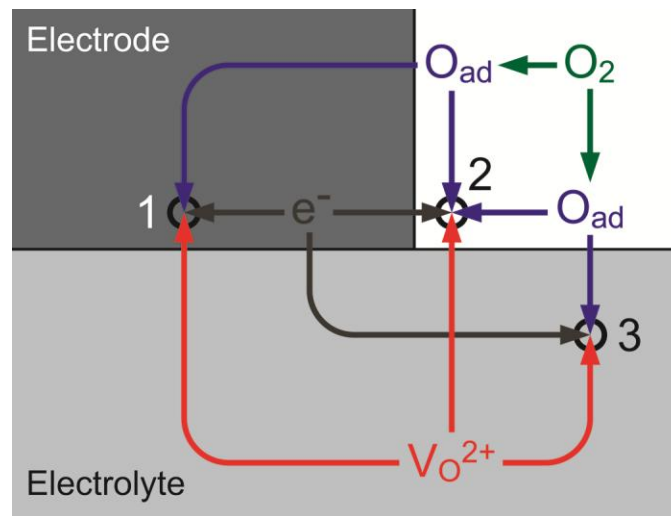


Figure 1. Schematic of possible transport pathways (arrows) of oxygen vacancies (V_o^{2+}), electrons (e^-), oxygen gas (O_2), and adsorbed oxygen (O_{ad}) in the vicinity of the electrode-electrolyte-gas triple phase boundary, as well as possible reaction sites (numbered circles): (1) electrode-electrolyte interface, (2) triple phase boundary, (3) electrolyte bulk or electrolyte surface.

In a real device, it is likely that many or all of these processes occur to some extent. However, many of the possible reaction steps can be expected to have a negligible effect on the electrode performance as a whole. For instance, a very slow reaction step that occurs in parallel with a faster step will not limit the overall reaction rate, while a very fast step occurring in series with a slower (limiting) step will not limit the overall rate either. In general, the overall rate of the electrode reaction is expected to be controlled by just a few key processes. Which mechanisms do influence the overall kinetics of a given electrode, and which are negligible, has been the subject of considerable study, which will be detailed in Sections 1.1.4.1–1.1.4.5.

1.1.3.1 Limiting and Co-Limiting Reaction Steps

It is well known from basic chemistry that when a chemical reaction proceeds via a number of sequential steps, the overall reaction rate is determined by the slowest step in the reaction. Therefore, in electrochemistry, identifying the limiting step in the electrode reaction is of critical importance in improving the overall kinetics as well as interpreting experimental results. However, in certain cases it is also possible for electrode kinetics to be simultaneously limited by more than one reaction step, which can significantly complicate understanding of an electrochemical system. Since this will turn out to be highly relevant to the present study, it is worth taking a moment to explain how such a situation can arise.

For illustrative purposes, consider diffusion of an arbitrary adsorbed species A along a one-dimensional electrode surface. A schematic of the relevant geometry is shown in Figure 2. At the electrode-electrolyte interface ($x = 0$), the concentration c of species A is fixed at zero due to a fast charge transfer reaction which generates a current proportional to the flux of A . A long distance from the interface ($x = L$), the

concentration is fixed at an equilibrium value, c_0 . The concentration gradient along the electrode surface provides a driving force for diffusion of A toward the electrode-electrolyte interface. Additionally, at locations where $c < c_0$, a driving force exists for adsorption of A from the atmosphere. The governing equation for this simple case is given by

$$\frac{\partial c}{\partial t} = D \frac{\partial^2 c}{\partial x^2} + k(c_0 - c) \quad (2)$$

where D is the diffusion coefficient and k is the surface exchange coefficient. Selected steady state solutions of (2) corresponding to various values of the ratio k / D are presented in Figure 2. As the figure shows, the size of the region where $c < c_0$ depends strongly on k / D . When diffusion is slow relative to adsorption (e.g. $k / D = 10^4$), the A -depleted region is small and all adsorption takes place close to the electrode-electrolyte interface. Conversely, when diffusion is relatively fast, a larger portion of the surface is available for adsorption and the average diffusion distance increases. A balance therefore exists between the diffusive and adsorptive processes, which jointly regulate the reaction rate.

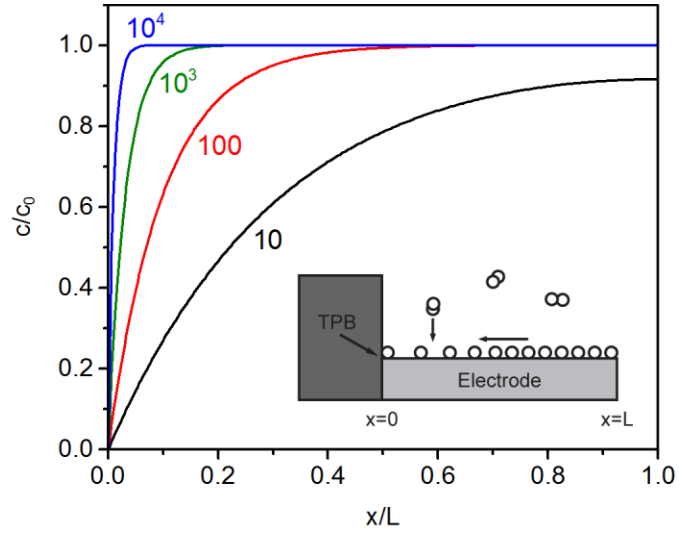


Figure 2. Normalized concentration profiles predicted by (2) for the indicated values of the ratio k / D in m^{-2} .

The co-limiting effect of adsorption and diffusion is demonstrated conclusively in Figure 3, which plots current density at the electrode-electrolyte interface vs. k for various values of the diffusion coefficient. It can be observed clearly from the figure that the current decreases with decreasing k as well as with decreasing D . More precisely, it can be shown that the current is proportional to \sqrt{kD} .⁴ Other types of co-limited reactions are also possible.

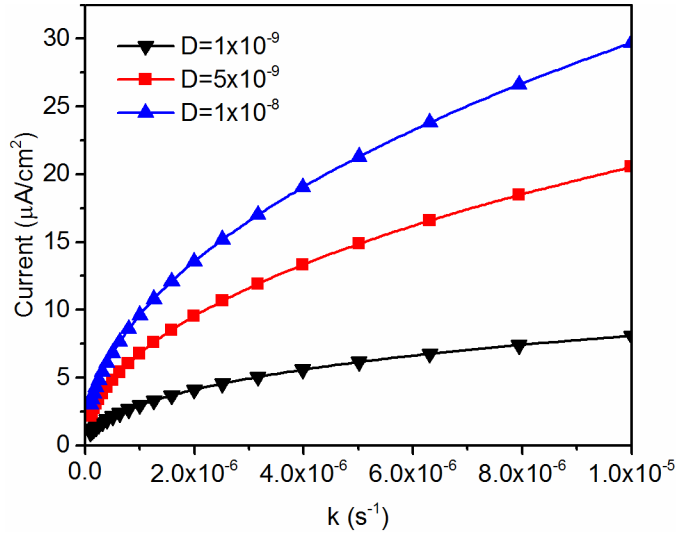


Figure 3. Current density predicted by (2) at the electrode-electrolyte interface as a function of surface exchange coefficient for the indicated values of the diffusion coefficient in m^2/s .

1.1.3.2 The Triple Phase Boundary

Electrode half-reactions in electrochemical cells occur at the electrode-electrolyte interface in the presence of a reductant (i.e., fuel) or oxidant. It is therefore intuitive, and also well-established in classical liquid electrochemistry,⁵ that the charge-transfer reaction at a gas electrode is confined to the triple phase boundary (TPB) where the electrode, electrolyte, and gas phase all come into contact. The same effect has also been observed for many solid-state electrochemical cells, whose performance often scales with TPB length rather than interfacial area. In order to proceed, the reaction requires spatial coexistence of gaseous oxygen, oxygen sites in the electrolyte lattice, and electrons. Assuming negligible conduction of electrons in the electrolyte (which is desirable in order to prevent current crossover losses), the TPB is the only point at which all three reactants are available. As a theoretical construct, the TPB is a purely one-dimensional boundary between phases. However,

intuition dictates that current flow requires a finite cross-section, and therefore the actual electrochemically active region is not truly one-dimensional, but has a finite extension along the electrode-electrolyte interface, the free electrode surface, or both.⁶ This is illustrated schematically in Figure 4.

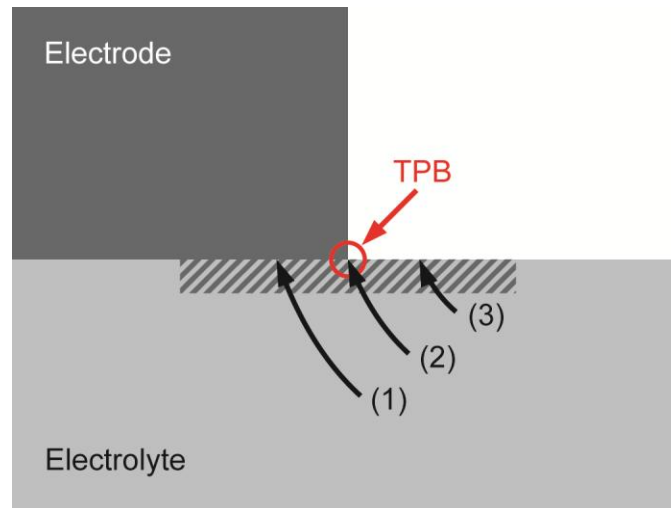


Figure 4. Schematic illustrating the possible physical extent of the electrochemically active area, indicated by the shaded region. Three possible current paths are shown: (1) active area extending along electrode-electrolyte interface, (2) active area confined to TPB, and (3) active area extending along free electrolyte surface.

The dependence of the electrode performance on TPB length means that in practical devices, it is preferable to increase this parameter as much as possible. This is generally accomplished using a porous, mixed conducting cathode material such as lanthanum strontium manganite (LSM) or lanthanum strontium cobalt ferrite (LSCF). Since these materials conduct both ions and electrons, and the pore structure allows oxygen to permeate, the three phase contact area is greatly enhanced compared to

more traditional electrode materials like platinum. However, the geometry of the TPB in porous electrodes is also very difficult to characterize, and repeatability between specimens may be poor since TPB length can vary by up to three orders of magnitude depending on electrode morphology.⁶ It is especially difficult to fabricate a series of porous electrode specimens with varying TPB sizes.⁷

1.1.3.3 Microelectrodes

For the reasons described in Section 1.1.3.2, porous electrodes are not well suited to studies where understanding the underlying electrochemistry, rather than maximizing performance, is the main objective. Instead, researchers conducting fundamental investigations generally prefer model systems with well-defined electrode and interfacial geometries. Microelectrodes⁷ have various applications in electrochemistry, including, in recent years, increasing use in fundamental electrochemical studies of SOFC materials.⁸⁻¹² Non-porous point or pattern microelectrodes have precisely defined geometries and can be fabricated in a straightforward and repeatable fashion using thin film processes. The simple geometry of the electrodes allows the electrode-electrolyte contact area and TPB length to be easily quantified^{8,13} and easily varied from specimen to specimen.

One particularly straightforward microelectrode geometry to fabricate consists of interdigitated electrodes patterned on the electrolyte surface using photolithography. A schematic of such electrodes is shown in Figure 5. This geometry allows both electrodes to be fabricated using a single photolithography step (if the same material is used for both) and does not suffer from the electrode alignment issues that may affect planar or radial geometries. The relative ease and repeatability of fabrication makes this interdigitated geometry an excellent choice for fundamental

studies, though the very large ratio of electrode area to TPB length negatively affects the performance of practical devices. Since the present study is not focused on practical applications, interdigitated surface electrodes will be considered throughout the majority of the work.

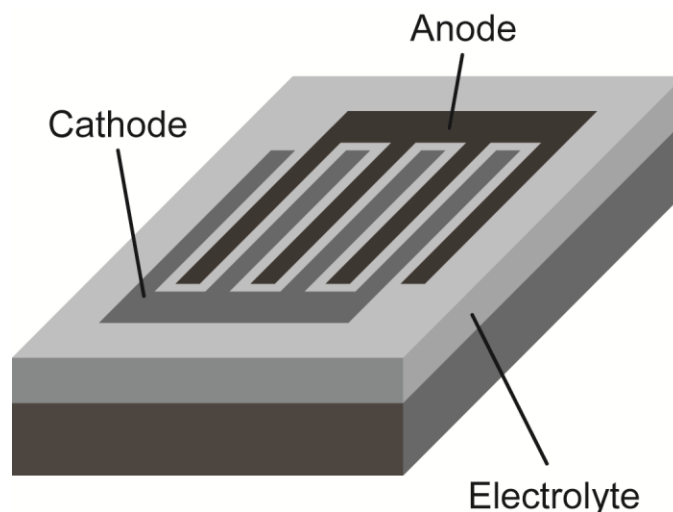


Figure 5. Schematic of a thin film electrochemical cell with interdigitated microelectrodes.

1.1.4 The Pt/YSZ Model System

While electrode morphology is naturally of considerable importance in fundamental electrochemical studies, the choice of electrode and electrolyte materials is also important. In order to be well suited as a model system, the materials need to be relatively simple in composition, easy to prepare, and stable over a wide range of temperatures and chemical surroundings. For the present work, the Pt, O₂|YSZ system; that is, platinum electrodes on a YSZ electrolyte in the presence of oxygen gas, is an ideal choice. This was one of the earliest solid state electrochemical systems to be

studied¹⁴ and has continued to attract significant research attention into the 21st century.¹⁵ Due to the large volume of related literature spanning more than a century, Pt, O₂|YSZ can be thought of as the “default” SOFC cathode even though the use of platinum electrodes in practical SOFCs is uncommon. Pt, O₂|YSZ cells do have practical applications as well (e.g. oxygen sensors), but they are more often studied as a model system.¹⁶ Despite the vast amount of research attention the system has received, its kinetics are complex and still poorly understood.

1.1.4.1 Bulk Versus Surface Path and the TPB

Pt, O₂|YSZ is often said to be a “surface path” system in which all reactions take place on the surface of the electrode and ion incorporation occurs only at the triple phase boundary. Experimental results have confirmed that this is indeed the case¹⁷—or, at least, that surface processes dominate the overall reaction. However, as discussed in Section 1.1.3.2, it is likely that the effective electrochemically active region extends somewhat beyond the TPB itself, and the width of this region is clearly important in determining the performance of the electrode. Despite this, there have been relatively few efforts to quantify the width of the active region or determine its physical location relative to the actual point of three-phase contact— whether it extends into the electrode-electrolyte interface, onto the free electrolyte surface, or both, or whether it extends beyond the surface into the bulk electrode or electrolyte (see Figure 4).

Some researchers have hypothesized that it should be possible to estimate the TPB size by measuring the resistance due to current constriction near the TPB. Under DC polarization, the current constriction resistance is “hidden” as part of the overall DC resistance, which also includes IV drop in the electrolyte, electrode polarization,

and other losses. However, the resistive contributions of these different processes can often be separated using the experimental technique of electrochemical impedance spectroscopy. (The theory and potential pitfalls of this technique will be discussed much more fully in Section 1.2.) Fleig et al. performed numerical simulations¹⁸ showing that a hypothetical current constriction close to the TPB did indeed constitute an observable relaxation process, supporting the idea that the TPB size could be measured using impedance measurements. Fleig later confirmed¹⁹ that current constriction does produce a distinct impedance feature, but only when the capacitance associated with the TPB is large compared to that of the electrode-electrolyte interface. Otherwise, the constriction resistance disappears into the overall electrode resistance.

Fleig's modeling work provided a possible means of estimating the TPB size for actual Pt/YSZ cells. However, putting these ideas into practice proved difficult. Hertz et al.²⁰ did observe an intermediate-frequency impedance feature that was qualitatively similar to the current constriction impedance predicted by Fleig. However, when they compared their experimental data to a quasi-DC current constriction model, the predicted resistances were smaller than those experimentally observed even when unrealistically small TPB sizes were assumed. This put in doubt whether the observed impedance was actually due to current constriction at all. Furthermore, impedance spectra reported for Pt/YSZ cells reported by other researchers often do not show an intermediate frequency feature (see for example Reference 12), In such cases there is little hope of applying Fleig's technique.

One other notable attempt to measure the TPB size took a completely different approach. Rather than impedance measurements, Opitz et al.^{21,22} used ¹⁸O isotopic

tracer experiments to investigate oxygen incorporation at the Pt|YSZ interface. At low temperature (300–330°C) they observed that the active area was located under the electrode at low overpotential and extended onto the free YSZ surface at higher overpotential. Using the tracer incorporation data, they were able to estimate a TPB width of approximately 1 μm after accounting for profile broadening due to ^{18}O diffusion in the YSZ. However, this broadening effect made it impossible to accurately apply the same technique at the higher temperatures typically encountered in SOFCs. Although the TPB size at high temperatures remains unknown, the work did provide clear evidence that it is possible for the electrochemically active area to extend along both the Pt-YSZ interface and the free YSZ surface.

1.1.4.2 Limiting Processes

Like many other chemical and electrochemical processes, the oxygen reduction reaction at the Pt/YSZ interface has often been discussed in terms of a rate limiting step. While it was initially believed that the reaction rate was controlled by charge transfer at the TPB, as would be the case in a conventional aqueous system, more recent research has demonstrated that this is not the case. Since reactions of this type may be co-limited by multiple steps (as discussed in Section 1.1.3.1), and different processes can dominate under different operating conditions, the overall electrode kinetics may be quite complex. More than 40 years of research has yielded some progress in understanding the nature of the Pt/YSZ cathode reaction, but total consensus has not yet emerged.

Early experimental investigations of platinum electrodes on solid oxides²³ under ambient conditions similar to SOFC operating conditions ($P_{\text{O}_2} \approx 1 \text{ atm}$, $500 < T < 1000^\circ\text{C}$) showed that the electrode polarization can be fitted using an equation in the

form of the Butler-Volmer relation, which in traditional aqueous electrochemistry²⁴ governs the current-potential relationship of an electrode when mass transport limitations are negligible. According to this equation, the electrode current density J is given by

$$J = J_0 \left[\exp\left(\frac{\beta z F}{RT} \eta\right) - \exp\left(-\frac{(1-\beta) z F}{RT} \eta\right) \right] \quad (3)$$

where J_0 is the exchange current density, β is a symmetry factor, z is the charge number of the electrolyte charge carrier, F is the Faraday constant, R is the gas constant, T is the absolute temperature, and η is the activation overpotential

$$\eta = \varphi - \varphi_{eq} \quad (4)$$

where φ is the absolute potential of the electrode and φ_{eq} is the equilibrium potential. The similarity of behavior led to the belief that the limiting step in Pt, O₂|YSZ systems is the same as in aqueous electrochemical systems: the charge transfer reaction. However, when it was studied by AC impedance²⁵, electrode capacitances as high as 550 $\mu\text{F}/\text{cm}^2$ were observed in some cases. Since the maximum estimated double layer capacitance was approximately 190 $\mu\text{F}/\text{cm}^2$, the measured capacitance was much too large to be explained via the double-layer mechanism at the root of Butler-Volmer kinetics.

In 1983, Verkerk et al. studied Pt/YSZ cells using both DC polarization measurements and AC impedance spectroscopy. Both studies provided evidence that the rate-limiting step at the electrode was not the charge transfer reaction. In the DC study, it was observed that the electrode resistance was proportional to $P_{O_2}^{\pm 1/2}$, whereas a $P_{O_2}^{\pm 1/4}$ dependence is expected if charge transfer is the rate limiting step.²⁶ Using AC impedance spectroscopy, the researchers also observed that the electrode

response could be modeled using a Warburg impedance, which is characteristic of diffusion-controlled processes.²⁷ (Impedance spectroscopy and equivalent circuits will be explained more fully in Section 1.2.) Both of these results were believed to point to a rate limiting step involving diffusion rather than charge transfer.

Mizusaki et al. later compiled a number of previous studies, including Verkerk's, showing that the researchers had reported various relationships between electrode resistance and P_{O_2} , including $P_{O_2}^{\pm 1/4}$, $P_{O_2}^{\pm 3/8}$, and $P_{O_2}^{\pm 1/2}$ dependences, along with a corresponding divergence of opinion as to the rate limiting step. However, Mizusaki et al. were able to fit all of the reported data for $T \geq 600^\circ\text{C}$ with a model assuming diffusion of adsorbed oxygen on the electrode surface as the rate limiting step. They were also able to fit data for $T \leq 500^\circ\text{C}$ with a model assuming dissociative adsorption of oxygen as the rate limiting step. Based on these results, it was concluded that these two steps controlled the reaction rate within their respective regimes.^{28,29} Schwandt and Weppner performed a similar study and also came to the conclusion that adsorbed oxygen diffusion was the rate limiting step based on the relationship between the electrode conductivity and P_{O_2} . Unlike Mizusaki, they believed their surface diffusion model adequately explained the reported behavior at all temperatures, without the need to invoke a different limiting step at $T \leq 500^\circ\text{C}$.³⁰

In a transient DC study, Robertson and Michaels observed that the Faradaic current decay in Pt/YSZ cells was proportional to $t^{-1/2}$. This Cottrell behavior was found to be consistent with a model assuming oxygen reaches the TPB via diffusion on the electrode surface, and is reduced only at the TPB. The results were inconsistent with a contrasting model in which oxygen is reduced over the entire electrode-electrolyte interface. In addition to clarifying the location of the oxygen reduction

reaction, this study provided evidence for adsorption and diffusion as limiting reaction steps when $T \leq 600^\circ\text{C}$. For higher temperatures, the transient current response was too fast to draw any meaningful conclusions.¹⁷

While most researchers limited their modeling efforts to steady state or transient DC experiments, Mitterdorfer and Gauckler sought to develop a model which was capable of explaining the AC impedance behavior of the Pt, O₂|YSZ system.^{31–33} Their model was solved numerically in state space and incorporated adsorption, surface diffusion, and charge transfer steps. The researchers showed that their model was able to match experimental results and provide estimates of the model parameters (diffusivity and reaction rate coefficients) that were consistent with the literature. Based on these findings, it was concluded that the adsorption/diffusion process and charge transfer each contribute a substantial portion of the total impedance at high oxygen partial pressure ($P_{O_2} \approx 1$ atm) and high temperature ($T \geq 800^\circ\text{C}$). At lower temperatures or lower P_{O_2} , the influence of charge transfer diminished, leaving adsorption and diffusion as the predominant processes. An additional process became notable for $P_{O_2} \leq 10^{-3}$ atm which was presumed to be gas-phase diffusion, although this was not investigated quantitatively. Mitterdorfer and Gauckler’s study helped to explain some of the earlier confusion as to the rate limiting reaction step since the reaction appears to be co-limited by multiple steps as discussed in Section 1.1.3.1.

Table 1. Summary of experimental studies of the rate limiting step for Pt, O₂|YSZ in the intermediate to high P_{O_2} range.

Study	T (°C)	P _{O₂} (atm)	Limiting step	Ref
Bauerle 1969	400–800	1.5×10^{-5} –1	Charge transfer	25

Mizusaki 1987	400–800	10^{-4} –1	Adsorption or diffusion	28,29
Robertson 1990	600–800	10^{-5} –0.21	Diffusion	17
Schwandt 1997	500–900	10^{-5} –1	Diffusion	30
Mitterdorfer 1999	700–800	10^{-4} –1	Multiple	31–33

The above work has considered porous electrodes exclusively, but some more recent studies have utilized microfabricated dense platinum electrodes in hopes of reducing the confusion associated with the ill-defined morphology of porous electrodes. EIS investigations by Opitz et al.^{12,34} found a change in activation energy of the electrode resistance moving from low to high temperature. The polarization resistance at low temperature (300–400°C) was found to scale with electrode area, while at higher temperature (550–700°C) the resistance instead scaled with TPB length. These results indicate two reaction pathways operating in parallel: one along the electrode surface, which dominates at high temperature, and one through the bulk electrode (probably along grain boundaries), which becomes important at low temperature. Steady-state DC measurements¹⁶ and low-temperature ¹⁸O tracer experiments²² provided additional evidence for this bulk pathway. There is also some evidence^{16,21} that the surface path kinetics in these experiments may in fact have been limited by diffusion through an impurity phase at the TPB (e.g. silicon), so the results must be interpreted cautiously in drawing conclusions about the Pt|YSZ system. Opitz et al. also noted the possibility of a thermoelectric voltage arising from temperature gradients in the YSZ, which can also complicate the interpretation of experimental results.^{12,35} Clearly, even for well-defined geometries, the electrode kinetics remain poorly understood.

1.2 Impedance Spectroscopy

Several studies incorporating electrochemical impedance spectroscopy (EIS) measurements were mentioned in Section 1.1.4.2. In fact, since the 1960s, EIS has become one of the most commonly used techniques for quantifying properties of solid ion conductors, and it is of central importance to the present work. In an EIS experiment, a sinusoidal electrical potential $\varphi(t)$ is applied to a sample under specified ambient conditions and the resulting current $I(t)$ is measured, allowing the complex impedance Z of the sample to be determined. The measurement is repeated over a range of frequencies to obtain an impedance spectrum $Z(f)$. While fuel cells and other electrochemical devices operate under DC conditions, the EIS technique makes it possible, at least in theory, to deconvolute the contributions of different processes to the overall DC resistance based on their differing relaxation times.²⁵ For example, an impedance spectrum for a simple electrical network with two parallel resistor-capacitor elements in series is shown in Figure 6. The spectrum is displayed as a plot of the negative imaginary impedance Z'' versus the real part Z' of the complex impedance over a range of frequencies, also known as a Nyquist plot. Because the two parallel resistor-capacitor elements have different time constants $\tau = RC$, their responses can be deconvoluted as distinct arcs in frequency space. It is now possible to quantify the individual contributions R_1 and R_2 , whereas a DC conductivity measurement reveals only the total resistance $R_1 + R_2$.

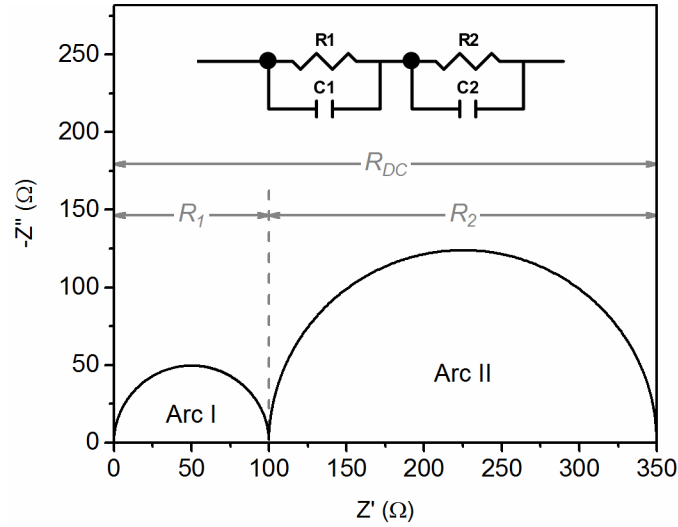


Figure 6. Simulated impedance spectrum for the electrical network shown in the inset. Circuit parameter values are $R_1 = 100 \Omega$, $R_2 = 250 \Omega$, $C_1 = 10 \text{ pF}$, $C_2 = 100 \text{ nF}$. $R_{DC} = 350 \Omega$ represents the resistance observed via a DC measurement, which conceals the separate contributions of R_1 and R_2 .

The impedance behavior of a solid electrochemical cell is qualitatively similar. Such spectra typically include a low frequency arc associated with the electrode reaction, which vanishes at higher frequencies as displacement current is able to short-circuit the electrode-electrolyte interface, and a high frequency arc associated with the bulk electrolyte. An additional arc associated with grain boundaries can also appear in polycrystalline materials. In an ideal case the resulting spectrum would appear very similar to Figure 6, with fully separated semicircular arcs, and the relevant system parameters can be quantified in a straightforward manner by fitting a simple equivalent circuit model as will be explained in Section 1.2.1. However, due to the many physical non-idealities that can occur in solid state electrochemistry, impedance spectra observed in the laboratory often show very different behaviors including

depressed, distorted, partial, or overlapping arcs, which can be difficult to interpret in light of the many different processes that can occur in solid state systems.

1.2.1 Equivalent Circuits and the Brick Layer Model

In order to quantify the relevant properties of an electrochemical system using EIS, the experimentally obtained impedance spectrum must be fitted with an appropriate physical model. However, the choice of model is nontrivial and requires careful justification as any number of models may fit the EIS data equally well.³⁶ An especially common way to model EIS data is to use an equivalent circuit,³⁶⁻³⁹ which lumps system properties into a network of resistors, capacitors, and other electrical circuit elements. While potentially useful, these models are also quite reductive and the physical meaning of the circuit elements can be ambiguous or otherwise prone to misinterpretation.^{39,40} Nevertheless they are very widely used due to their simplicity.

As an example, a simulated impedance spectrum for an ideal “brick layer” polycrystal with negligible electrode resistance is shown in Figure 7. The brick layer model is a simplified polycrystal geometry with (1) uniformly sized, cubic grains, (2) uniform grain properties (i.e. conductivity and permittivity), (3) uniform grain boundary properties, and (4) uniform grain boundary thickness.⁴¹ This geometry can be reduced via series and parallel combination of repeat units into a simple equivalent circuit, making it a good example to illustrate how equivalent circuit fitting works under ideal conditions. (Equivalent circuits can also be derived for uniform triangular or hexagonal grains.) The impedance spectrum for the brick layer consists of two arcs in the complex plane, traced out from low frequency at the right to high frequency at the left. At low frequencies, the impedance includes resistive contributions from both the grain boundaries and the grain bulk, while at higher frequencies the thin grain

boundaries become dielectrically short-circuited and the only resistance comes from the bulk (grain cores). Thus the highest frequency arc is considered to correspond to the grain impedance, and the other arc corresponds to the grain boundary impedance.

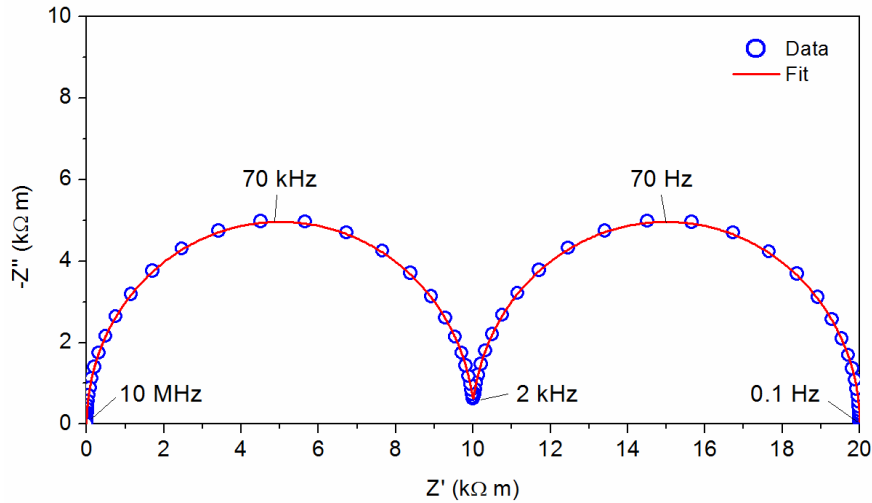


Figure 7. Simulated impedance spectrum obtained by solving Poisson’s equation at varied frequency for a single repeat unit of an ideal “brick layer” polycrystal. A fit to the data using an ideal RC-RC equivalent circuit is also shown. Model parameters were $\sigma_{grain} = 10^{-4}$ S/m, $\sigma_{gb} = 10^{-7}$ S/m, $\epsilon_{grain} = \epsilon_{gb} = 25$, grain size = 10 μ m, and grain boundary thickness = 1 nm (chosen so that the grain and grain boundary resistances are equal).

In this example case, since the electrolyte geometry is an ideal brick layer, the impedance data can be fitted using an equivalent circuit of the form shown in Figure 6 to model the resistive and capacitive behavior of the electrolyte. The circuit consists of two parallel (R,C) elements connected in series, representing the grain and grain boundary, respectively. The four fitting parameters R_1 , R_2 , C_1 , and C_2 may be easily related to the grain and grain boundary parameters via the simple plate capacitor equation

$$C = \frac{\varepsilon\varepsilon_0 A}{L} \quad (5)$$

and the resistor equation

$$R = \frac{L}{\sigma A} \quad (6)$$

where ε is the relative permittivity, ε_0 is the permittivity of free space, σ is the conductivity, A is cross-sectional area, and L is the plate separation distance or resistor length. Making use of the known geometric parameters allows the conductivity and permittivity of the grains and grain boundaries to be calculated. (In some cases, researchers will make the assumption that $\varepsilon_{gb} = \varepsilon_{grain}$ and use (5) to calculate the grain boundary thickness instead.) This approach provides accurate quantification of σ and ε in the case of the perfect brick layer example, but it is less reliable when the electrolyte strays from the brick layer geometry. Nevertheless serial equivalent circuits are commonly used in experimental EIS studies.^{42,43}

Electrode processes can also be investigated to some extent using equivalent circuit models, at least in the sense that it is usually possible to quantify a resistance and capacitance associated with electrode processes. However, studies capable of specific, precisely quantifiable characterization of the electrode usually require a more system-specific model.

1.2.2 Constant Phase Elements

In many cases, researchers wishing to model the impedance behavior of systems exhibiting depressed impedance arcs make use of equivalent circuits including one or more constant phase elements (CPEs). The CPE is a mathematical generalization of the resistor, capacitor, and inductor elements in classical electrical circuit theory and has an impedance Z defined by

$$Z = \frac{1}{Q(i\omega)^n} \quad (7)$$

where $i = \sqrt{-1}$, ω is the angular frequency, and Q and n are unnamed parameters. In conventional usage, the exponent n is in the range $[-1, 1]$ and determines how “inductively” or “capacitively” the element can be considered to behave. When $n = 1$, (7) reduces to

$$Z = \frac{1}{i\omega Q} \quad (8)$$

and the CPE is equivalent to an ideal capacitor with capacitance Q . Similarly, the CPE reduces to a pure inductor when $n = -1$, and to a pure resistor (with neither inductive nor capacitive behavior) when $n = 0$. In the range $0.7 < n < 1$ the CPE may be thought of as an “imperfect capacitor,” with n providing a measure—albeit one that is rather abstract and of ambiguous physical meaning—of the non-ideality of the device. As shown in Figure 8, the flexibility afforded by the CPE’s extra fitting parameter as compared to a capacitor allows for reduced residual error in the fit to depressed impedance arcs. However, the physical basis for the CPE remains suspect and it remains unclear how best to recover useful information from the CPE parameters Q and n (except in the near-ideal case where simple capacitive behavior is seen).

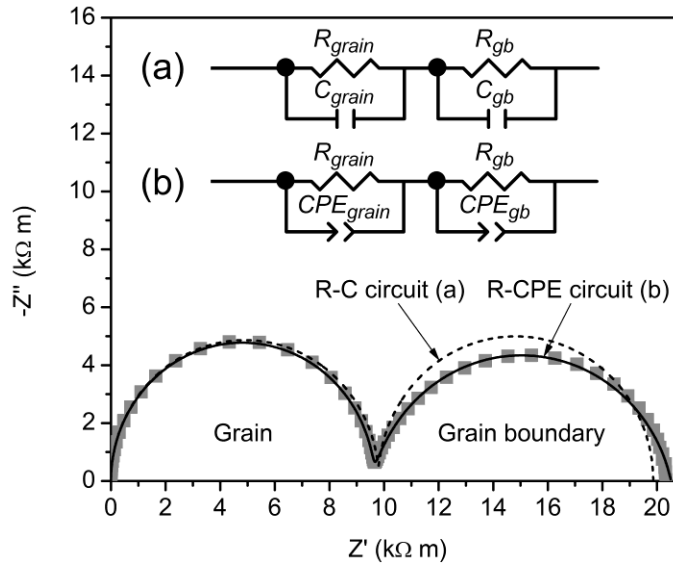


Figure 8. Hypothetical impedance spectrum for a polycrystalline electrolyte (squares), along with best-fit curves (dashed and solid lines) corresponding to the indicated equivalent circuits.

In an attempt to derive useful information from the CPE parameter values, one equation originally given by Brug et al.⁴⁴

$$C_{Brug} = R^{(1-n)/n} Q^{1/n} \quad (9)$$

which gives an “effective capacitance” is frequently encountered in the literature.⁴⁵

This equation was originally derived for the case of an ideally polarized electrode, but has also frequently been applied to grain boundaries.⁴⁶⁻⁴⁸ One merit of (9) is that it yields a peak frequency $\omega_{gb} = 1/(R_{gb}C_{gb})$ which is consistent with the observed impedance spectrum. The expression for C_{gb} is also consistent with an interpretation of the R-CPE circuit as a weighted integral of R-C elements.⁴⁶ However, although it generally gives plausible results, there has not been a systematic study of the applicability of Brug’s equation to grain boundary capacitance.

1.2.3 Issues Complicating the Use of Equivalent Circuits

In the ideal case where the properties of a polycrystalline electrolyte are well approximated by the brick layer model, equivalent circuit fitting is capable of characterizing the grain and grain boundary properties with a high degree of accuracy. However, real polycrystals usually violate one or more of the assumptions of the brick layer model; that is, they have irregularly sized and shaped grains, voids, impurities, heterogeneous grain and/or grain boundary properties, and non-uniform grain boundary thicknesses. Such non-idealities can affect the observed impedance spectrum in a variety of ways and can significantly complicate efforts to characterize the material using equivalent circuit fitting. In many cases an equivalent circuit fit can be misleading or useless.

1.2.3.1 Non-Ideal Microstructures

The oftentimes considerable deviation of real polycrystals from the ideal brick layer geometry is well known, but there has not been much research into the implications for equivalent circuit-based measurements. One important series of studies was conducted by Fleig et al., who investigated the relationship between electrolyte microstructure and the resultant impedance spectrum using a numerical modeling approach to solve Laplace's equation over a two- or three-dimensional region with an appropriate treatment of the grain boundaries and electrodes.^{46,49,50} This work has shown that heterogeneous grain sizes or grain boundary properties can result in a distorted grain boundary arc in the impedance spectrum.^{41,51} An example from Fleig's work is shown in Figure 9 for a case where two different grain sizes are present in the electrolyte, violating condition (1) of the brick layer model. As seen, the low frequency (grain boundary) arc is significantly distorted compared to a true

semicircle; in more extreme cases, even greater distortion is possible. Even for ideal grain geometries, it was observed that variance in the grain boundary conductivity could still result in distorted low frequency arcs. In particular, inhomogeneous conductivity of the grain boundaries was found to contribute strongly to distortion of the grain boundary arc. The researchers modeled a small number of polycrystals with different numerical distributions of the grain boundary conductivity, and it was noted that the mean resistance could be satisfactorily estimated using the brick layer model in the case of a relatively narrow Gaussian distribution. Still, the grain boundary arc was visibly depressed. The effect became even more pronounced when uniform or bimodal distributions of grain boundary conductivity were used, and the mean conductivity predicted from the brick layer model became quite inaccurate. While limited in scope, this study illustrated some of the challenges associated with attempting to quantify the properties of heterogeneous grain boundaries using equivalent circuit models.

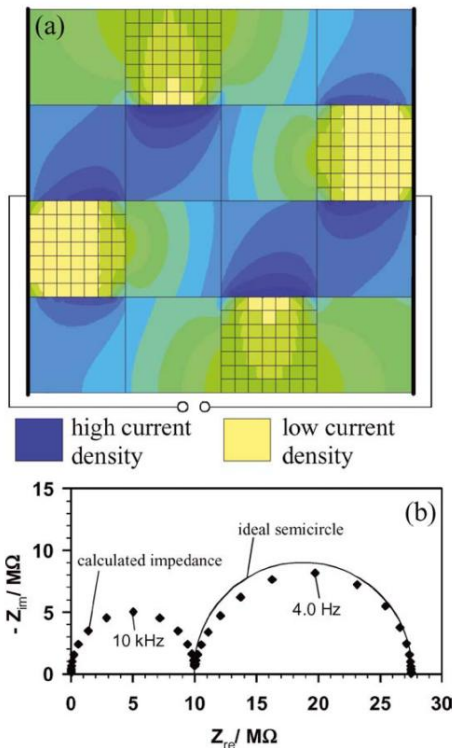


Figure 9. A distorted grain boundary semicircle resulting from an inhomogeneous grain size distribution in a sample with resistive grain boundaries. Figure reprinted from Reference 52 (© 2004 Kluwer Academic Publishers) with permission of Springer.

Although Fleig et al. helped clarify the effect of heterogeneity on the grain boundary arc, their study was not extensive enough to provide much quantitative analysis. There is a definite need among researchers who use EIS to study polycrystals for a comprehensive study of how heterogeneity of the grain boundary properties affects the impedance spectrum, incorporating a large number of randomly generated electrolyte simulations. Additionally, the effect of heterogeneous permittivity is not known at all, nor is that of heterogeneous conductivity and permittivity combined. Finally, it would be highly beneficial to clarify how useful CPE-based equivalent

circuits can be in quantifying heterogeneous grain boundary properties. For instance, it seems reasonable that the grain boundary conductivity value obtained from an equivalent circuit fit should approximate the mean conductivity of the (heterogeneous) individual grain boundaries. Similarly, it is tempting to use the CPE parameter n , which provides an abstract measure of non-ideality, as some kind of estimate of the standard deviation of grain boundary conductivities or permittivities. However, the feasibility of such uses of the CPE data is not justified by any research to date.

1.2.3.2 Ambiguity of Impedance Features

Apart from the difficulties associated with depressed or distorted arcs, features observed in impedance spectra are often hard to characterize even when relatively well defined. For example, Figure 10 shows a simulated impedance spectrum for a case where current at the electrode-electrolyte interface is constricted due to localized reaction processes at the TPB.^{18,50} As a consequence, the area of the electrode-electrolyte interface available to conduction expands at higher frequencies from the constricted region near the TPB to the entire interface due to displacement current. Therefore, the low frequency arc in the impedance spectrum includes not only the interfacial resistance, but also the resistance associated with current constriction in the electrolyte (which is a function of electrolyte conductivity). This means that the electrolyte resistance contributes to both the low- and high-frequency arcs. The actual electrolyte resistance under DC conditions, which includes the constriction resistance, is illustrated in the figure. It is clear that a conventional equivalent circuit analysis associating the low frequency arc with the interface and the high frequency arc with the electrolyte will result in erroneous values for both resistances. Similarly ambiguous spectra may occur in other situations where the current distribution is

frequency-dependent, such as when insulating phases are present at grain boundaries⁵³ or at the electrode-electrolyte interface,⁵⁴ or when the grain geometry is non-ideal.⁴¹ It is evident from these studies that there are many potential pitfalls in applying equivalent circuit models in cases where the underlying electrochemical mechanisms are not well understood.

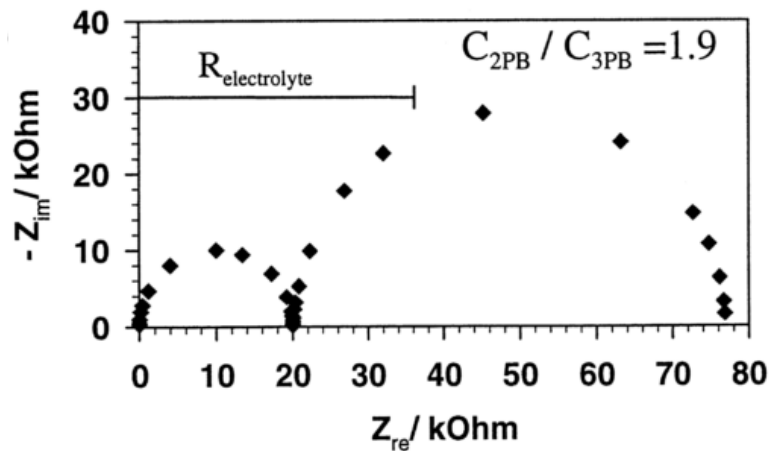


Figure 10. An ambiguous impedance spectrum caused by current constriction near the three phase boundary, with the true constricted electrolyte resistance indicated. Figure reprinted from Reference 50 (© 1998) with permission from Elsevier.

In addition to potentially misleading features, impedance spectra may also contain features whose physical meaning is unclear. One anomalous impedance feature of particular relevance to the present work has been observed in previous studies of thin film cells with the interdigitated electrode geometry shown in Figure 5.^{20,55} An example of such an impedance spectrum, obtained for a gadolinium doped ceria (GDC) thin film electrolyte with dense platinum electrodes at 652°C, is shown in

Figure 11. The spectrum consists of three arcs, labeled I, II, and III in the figure. The high frequency arc I is typically attributed to the bulk electrolyte, while the low frequency arc III is attributed to the electrode reaction. However, the meaning of the intermediate frequency arc II is less clear. Hertz et al. attributed the intermediate frequency arc observed in platinum/yttria stabilized zirconia (YSZ) cells to a current constriction effect near the TPB, similar to that shown in Figure 10 but more clearly separated in frequency space.²⁰ A schematic of the proposed low and high frequency current distributions in the electrolyte is shown in Figure 12a. Under DC or low frequency conditions, current is confined near the TPB, which is the only location where the oxygen vacancies, electrons, and oxygen gas required for the electrode reaction are all present. At higher frequency, displacement current is able to travel over the entire electrode-electrolyte interface and, according to this model, the constriction resistance vanishes. However, the researchers' quasi-DC numerical modeling approach predicted that an unrealistically small TPB size would be required to account for the magnitude of resistance observed experimentally.

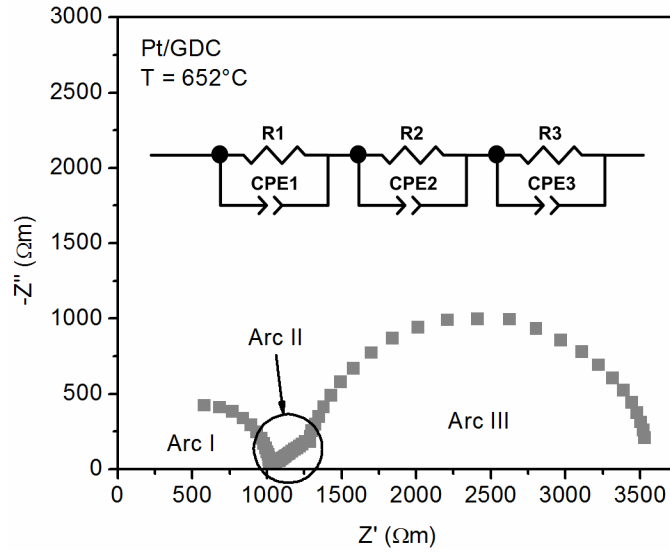


Figure 11. Sample impedance spectrum for a Pt/GDC specimen with an electrolyte thickness of 30 nm and electrode spacing and width of 25 μm . A possible equivalent circuit to fit the spectrum is shown in the inset.

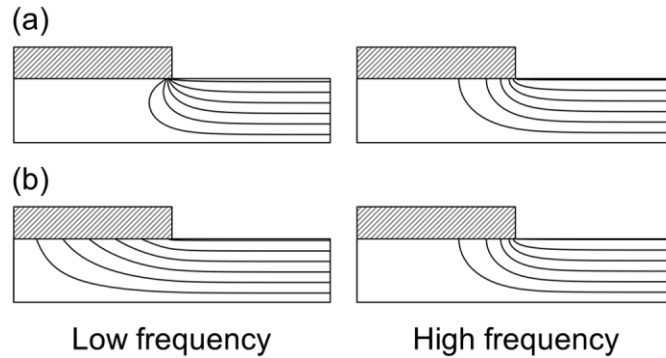


Figure 12. Two possible mechanisms for the intermediate frequency arc: (a) low frequency current constriction at TPB; (b) low frequency current spreading at electrode-electrolyte interface.

Another possibility is that the mechanism for the intermediate frequency impedance is the spreading of current in the electrolyte at low frequencies. A spreading resistance refers to the increased resistance due to nonparallel current flow

through a conductor. A thin film electrolyte considered alone has negligible spreading resistance.⁵⁶ However, Zhang et al. have shown that contact between two phases with different conductivities can result in a much larger spreading resistance.⁵⁷ A result similar to Zhang's could be expected if there is substantial resistance to current flow at the electrode-electrolyte interface. In this case, current is forced to spread across the whole electrode-electrolyte interface at low frequency. At higher frequencies, the interfacial impedance vanishes since the parallel capacitance of the interface allows current to cross the interface dielectrically. The current is thus able to take a shorter path through the electrolyte on average. The low and high frequency current paths through the electrolyte predicted by this hypothesis are shown in Figure 12b.

It is also worth noting that the shape of the intermediate frequency feature shown in Figure 11 is reminiscent of a Warburg impedance, which manifests as a 45-degree line in the impedance plane and often arises from a diffusion process. Although the impedance feature observed here is not strictly linear and has a "slope" closer to 30 degrees, the possibility that the intermediate frequency impedance could be due to diffusion still merits some discussion. As the experiments discussed in References 20 and ⁵⁵ were performed under atmospheric conditions, it is highly unlikely that the electrode reaction could be limited by gas-phase diffusion at the frequencies under consideration. However, solid state bulk oxygen diffusion⁵⁸ or diffusion-limited oxide formation⁵⁹ can occur within the platinum electrode. Still, the published diffusion coefficients^{59,60} are on the order of 10^{-23} to 10^{-22} m²/s, too low to result in a characteristic frequency in the relevant range. Therefore, the possibility of a diffusion-related feature in the impedance spectrum was discounted.

1.3 Modeling Solid State Electrochemical Systems

As the results in Section 1.2.3 illustrate, the geometric and electrochemical complexity of actual SOFC materials can often hinder analysis using equivalent circuits and other similarly reductive models. This reveals two potential areas of inquiry: firstly, under what circumstances equivalent circuit models remain useful, and secondly, what kinds of (more advanced) models may be developed to replace them. As these questions are of central importance to the present work, it is necessary to present an overview of the literature in modeling solid state electrochemical systems and the extent to which such efforts have been successful. While the present work is primarily focused on thin film, surface electrode cells, models developed for a variety of cell geometries will be discussed.

Modeling, whether via analytical or numerical methods, is frequently a useful tool in elucidating the behavior of solid state electrochemical systems. It can be used both for fitting of experimental results and for simulating systems from the ground up using fundamental equations. In the former case, the fitting procedure yields parameter values which are then typically compared to literature values for validation, whereas in the latter approach parameters are quantified at the outset using literature values and the resulting electrochemical behavior (e.g., polarization curves or impedance spectra) are validated by comparison with experimental results. The parameters of interest are usually diffusion coefficients or conductivities for transport processes, rate constants for reactions (often expressed as exchange currents for charge transfer reactions), electrolyte resistances and double layer capacitances, and geometric factors relating to the size and distribution of active sites. A summary of modeling techniques relevant to the Pt, O₂|YSZ system under consideration here will be presented over the following sections.

1.3.1 Electrolyte Impedance Models

While experimental impedance measurements are typically dominated by electrode processes, the researcher may be interested only in characterizing the electrolyte. In contrast to experimental studies, simulation with an appropriate model allows the electrolyte behavior to be isolated by assuming perfect electrode kinetics. The principal area of interest in electrolyte impedance studies is the contribution of grain boundaries, and sometimes impurity phases, to the overall electrolyte resistance. As already discussed, the simplest form of electrolyte modeling uses the brick layer model (BLM) to reduce the polycrystalline ceramic to a simple equivalent circuit.^{42,43} However, as discussed in Section 1.2.3, there are many cases in which the brick layer approximation may not yield satisfactory results. Studies by Fleig and Maier have used 2D and 3D electrical models based on the Laplace equation to simulate the impedance of a variety of electrolyte morphologies, including homogeneous low-conductivity grain boundaries in both ideal and realistic microstructures,^{46,49,50} laterally heterogeneous grain boundaries containing insulating phases,⁵³ heterogeneous distributions of grain sizes and boundary conductivities,^{41,51} and small grain boundary arrays with both high and low conductivity suitable for comparison with microelectrode measurements.⁶¹⁻⁶³ The primary purpose of their electrical models was to investigate the efficacy of the BLM; the models generally included too many variables to be useful for direct fitting of experimental results.

Other researchers have also noted the limitations of equivalent circuit models and have proposed alternative microstructural models. Kidner et al.⁶⁴⁻⁶⁶ noted that even for relatively regular microstructures, crystals with nano-sized grains were poorly modeled by the brick layer model due to the large volume fraction of grain boundaries relative to grain interiors. They explored alternative models, treating the

microstructure first as an array of nested cubes and then as an array of packed, coated spheres. While their models offered an improvement over the BLM in the nanoscale regime, the differences between the models are minimal for larger grain sizes. Dean et al.,⁶⁷ rather than merely modifying or extending the BLM, sought instead to simulate the electrochemical behavior of an entire microstructure using finite element modeling. Like Fleig and Maier, they were able to show the potential for large inaccuracies when applying the brick layer model to irregular grain geometries. However, the geometric complexity and computational expense of their finite element model make it a minimally useful substitute for the BLM in actual experimental studies.

1.3.2 Empirical Electrode Models

The type of modeling just described yields significant insight into the impedance behavior of solid electrochemical cells, but without a more realistic treatment of electrode processes, the opportunities for quantitatively interpreting experimental impedance spectra are limited. One of the first attempts to model a noble metal/conductive solid oxide interface came from Wang and Nowick,²³ who employed the Butler-Volmer equation (3) to model the current-voltage relationship at the interface. They found their model fit experimental data and were thus able to quantify the fitting parameter J_0 , the exchange current density. Numerous experimental values of J_0 can be obtained from the literature for various temperatures and pressures under the assumption of Butler-Volmer kinetics.^{23,25,26,68–71}

As discussed in Section 1.1.4.2, Mizusaki et al.^{28,29} later showed that charge-transfer kinetics alone cannot adequately explain the observed polarization behavior, and thus while the measured J_0 is still a phenomenologically useful parameter, it is not

physically meaningful. Their proposed model included surface adsorption and diffusion processes in addition to the electrode reaction, and allowed quantification of the model parameters via fitting of experimental DC polarization data. Nevertheless, impedance models based on Butler-Volmer kinetics or a simple assumption of RC behavior at the interface have continued to be employed due to their simplicity and phenomenological usefulness. For instance, Fleig and Maier have investigated effects related to the electrode-electrolyte interface using this approach, including the impedance associated with air gaps at the interface,^{54,72,73} electrode polarization,⁷⁴ and current constriction at the TPB.¹⁸ These electrode effects were treated only phenomenologically, by defining an interphase region with properties different from the bulk electrolyte without consideration of the polarization mechanism.

1.3.3 More Detailed Physicochemical Models

Continuum modeling based on physicochemical processes can yield greater insight into electrochemical systems than the simpler models discussed above. This type of modeling is most often applied to SOFC systems, so porous single-phase or composite mixed-conducting electrodes are usually considered rather than dense metal electrodes. This approach is typified by an influential paper by Adler et al.,⁷⁵ where a one-dimensional model of a porous mixed-conducting oxygen electrode was developed. The model considered three contributions to the electrode impedance: interfacial charge-transfer, solid state diffusion of oxygen ions in the mixed conductor, and (at low P_{O_2}) gas-phase diffusion. Impedance spectra derived from the model were fitted to experimental results and the values of the fitting parameters thus obtained were shown to be plausible.

Similar models were developed by Svensson et al.,⁷⁶ who also considered multistep adsorption and diffusion of oxygen on the electrode surface, and Costamagna et al.,⁷⁷ Chan et al.,⁷⁸ and Kenney and Karan,⁷⁹ who opted to use Butler-Volmer kinetics without considering detailed reaction mechanisms. Chan et al. later contributed a very generalized modeling approach considering many possible polarization mechanisms and with parameter values estimated from independent literature reports rather than fitting of experimental data.⁸⁰⁻⁸² Their composite cathode model considered polarization due to multistep charge transfer, grain and grain boundary resistance, gas phase diffusion, and constriction due to limited distribution of active sites (TPB regions), and they were able to determine the relative importance of these processes via parametric studies. However, the model included no temperature or P_{O_2} dependence of input parameters, and made the assumption that neither adsorption nor charge transfer at the TPB is rate-determining. Pakalapati et al. also developed a porous mixed conducting cathode model considering a multistep charge transfer process.⁸³

While these models were able to capture the relevant behavior of porous electrodes, they are not directly applicable to the present study of dense electrodes. Due to the small particle sizes involved, porous models rarely consider diffusion on the electrode surface since oxygen is able to adsorb directly near the TPB. However, the experimental results discussed in Section 1.1.4.2 have shown that surface diffusion is one of the most important processes influencing the cell impedance. On the other hand, gas phase diffusion is a key component of most porous electrode models, since the narrow pores can significantly restrict the supply of oxygen to TPB sites. In the case of dense electrodes, gas phase diffusion can be considered negligible when the

partial pressure of O₂ is greater than about 10⁻³ atm.³³ In addition, porous electrode models often place considerable emphasis on morphological parameters like particle size, tortuosity, and percolation threshold, which are irrelevant to dense electrode studies. Due to these fundamental differences between porous and solid electrodes, the results obtained from the above models have very limited applicability to the system presently under consideration.⁸¹

Another key shortcoming of all the models presented so far is that they are implemented only in one dimension. This can be considered appropriate for the planar or radial construction of most macroscale devices, but the thin film cells under discussion here have both electrodes fabricated on the same surface of the electrolyte, so the curved path of current through the geometry should be taken into account. In a DC model, this can be addressed trivially by adding a spreading resistance to account for the curved current path. However, in impedance studies, constriction and/or spreading of current at the electrode can be hidden by other processes as discussed in Section 1.2.3.2. Returning to that discussion, Figure 10 illustrates how a constriction of current near the TPB can masquerade as part of the “electrode” impedance. Any one-dimensional model applied to these data would clearly underestimate the actual electrode conductivity by a significant margin. Furthermore, current spreading and constriction effects can arise even in planar or radial systems due to current blocking at the electrode-electrolyte interface (such as in the Pt, O₂|YSZ system), or asymmetry of the electrodes. Since none of these issues can be adequately addressed via one-dimensional modeling, the models described here are insufficient for the purposes of the present study.

A model more specifically suited to the Pt, O₂|YSZ system was developed by Mitterdorfer and Gauckler, who considered adsorption and diffusion on the electrode surface as well as charge transfer at the TPB.^{31,32} Their model was solved numerically in state space, and when fitted to experimental impedance spectra for Pt/YSZ cells, plausible values were obtained for the adsorption constants, diffusion coefficient, and charge transfer resistance. The authors also observed that when they modeled adsorption of oxygen on platinum as a single-step dissociative process, the adsorption rate constants and adsorbed oxygen diffusivity were dependent on the adsorbed oxygen concentration. This led them to develop a second iteration of the model incorporating adsorbed molecular oxygen as an adsorption precursor, which allowed for concentration-independent adsorption parameters.³³ However, the model was still implemented in only one dimension. In addition, all state-space models share the common disadvantage that the system must be linearized, and thus the ability to simulate current-voltage characteristics in the nonlinear range is lost.⁸⁴

Bieberle and Gauckler later developed a model of the Ni, H₂-H₂O|YSZ system representing the typical SOFC anode using the same general method as the cathode model.⁸⁵ The authors included multistep charge transfer kinetics and adsorption/diffusion behavior in the model and were able to initialize all of the model parameters using estimates from the literature. The model showed a good fit to experimental data; however, the model considered only a single set of (T, P_{O_2}) values and neglected a probable mechanism of hydrogen adsorption and diffusion on YSZ due to lack of available data. Other researchers have also developed sophisticated anode models. Bessler et al. enumerated a generalized modeling framework which was applied to the Ni, H₂-H₂O|YSZ system,⁴⁰ and then extended to a full cell-level

model.^{86,87} The framework included generalized multistep charge transfer, gas-phase transport, and surface chemistry effects, but did not consider the role of TPB size. The model was used to fit experimentally obtained impedance spectra for Ni/YSZ cermet anodes,^{88,89} and sensitivity analysis and selective simplification of the model allowed the authors to relate the observed impedance arcs to physical processes. Application to experimental results for Ni pattern electrodes allowed the authors to determine the location of electrochemical reaction sites on the electrode/electrolyte surface.⁹⁰ A similar model considering the electrode and electrolyte surfaces was also developed by Goodwin et al.⁹¹ These models, while not directly applicable to the Pt, O₂|YSZ cell, demonstrate the ability of physicochemical modeling to help clarify reaction mechanisms and impedance features.

Full cell-level SOFC impedance models have also been developed in recent years, though these models tend to employ Butler-Volmer kinetics to describe the electrode reactions since this type of modeling is typically concerned with the functionality of the fuel cell as a whole rather than achieving a detailed understanding of fundamental processes. Such models have been developed by Zhu et al.^{92,93} and Shi et al.,⁹⁴⁻⁹⁶ who included more detailed electrochemical reactions suitable for dealing with internal reforming processes. Other cell-level impedance models based on Butler-Volmer kinetics have been developed by Hofmann and Panopoulos⁹⁷ and Mohammadi et al.⁹⁸

As this overview makes clear, there is still room for improvement in modeling the Pt, O₂|YSZ thin film electrochemical cell. In particular, there has not been a two-dimensional model of the Pt/YSZ interface to date, which is a necessity in understanding the impedance of a cell with surface electrodes (one of the main goals

of this work). Even in the cases of planar or radial cell geometries, current constriction and spreading effects may not be negligible and therefore two-dimensional modeling will be helpful in this area as well. It is also desirable to develop the model in the time domain rather than continuing the linearized state-space approach of Mitterdorfer and Gauckler, which does not allow simulation of I-V characteristics into the nonlinear range. These two advancements, extending to two dimensions and into the nonlinear simulation range, will greatly improve the versatility of Pt, O₂|YSZ modeling efforts.

1.4 Summary of Existing Literature

1. It is known from the work of Fleig et al.⁵¹ that heterogeneous grain boundary properties can cause a depressed grain boundary arc to appear in the impedance spectrum. Impedance spectra were generated via numerical solution of Laplace's equation over two- and three-dimensional geometries with an appropriate treatment of the grain boundaries. The researchers modeled three cases of heterogeneous grain boundary conductivity: a normal distribution, a uniform distribution, and a bimodal distribution. Distortion of the grain boundary impedance arc was observed in all three cases, most noticeably the uniform and bimodal distributions. However, comparisons between the different cases were purely qualitative as fewer than five randomly generated microstructures were modeled for each case. There has not been a systematic, quantitative study of the extent to which heterogeneous grain boundary conductivity can distort the grain boundary arc. Also, there has been no study of polycrystals with heterogeneous grain boundary permittivity, or with simultaneously heterogeneous permittivity and conductivity.

2. When depressed grain boundary impedance arcs are encountered, researchers often use CPE equivalent circuit fitting to estimate a "mean" grain

boundary conductivity. Similarly, it is possible to estimate a mean permittivity (or grain boundary thickness) using Brug's equation (9). However, the accuracy of this estimation procedure has not been quantitatively investigated. Additionally, while the CPE exponent n provides a qualitative indication of the non-ideality of the electrolyte microstructure, it is not known whether, or how accurately, the value of n can be related to a quantitative measure of heterogeneity of the grain boundary conductivity and/or permittivity (i.e. standard deviation in the case of a normal distribution).

3. Equivalent circuit fitting of experimental impedance spectra is often hindered by a lack of understanding of the mechanisms producing various impedance features, and thus the physical meaning of the circuit parameters can be unclear. For instance, previous experimental work by Hertz et al.^{20,55} has shown an intermediate frequency impedance feature of unknown origin for platinum microelectrodes on both YSZ and GDC thin film electrolytes. It was determined that this feature was not, as initially hypothesized, caused by current constriction at the TPB, but its actual mechanism of origin has not been identified. This feature has only been observed in thin film cells with surface microelectrodes.

4. The electrode kinetics of the Pt, O₂|YSZ system are not completely understood. It has been known since the 1980s that the electrode reaction is not limited by the charge transfer step (1) as in conventional aqueous electrochemistry. Instead, more recent models treating the reaction as jointly controlled by adsorption and diffusion on the electrode surface as well as charge transfer have provided a good match to experimental results for planar cells in the (T, P_{O_2}) regime relevant to SOFC operation.

5. Thin film electrochemical cells with interdigitated microelectrodes have various practical applications but are also useful as easy-to-fabricate model systems with well-defined interfacial and TPB geometries and good repeatability suitable for fundamental electrochemical studies. An appropriate model of the Pt, O₂|YSZ thin film cell, combined with experimental results, will provide more evidence of the electrode reaction mechanisms. However, existing models of the Pt, O₂|YSZ system have been implemented in one dimension, which ignores the effect of TPB width, interfacial (pseudo)capacitance, and current spreading and/or constriction. Additionally, the most advanced model to date, developed by Mitterdorfer and Gauckler,^{31,32} was implemented in state space using linearized equations, which limits the ability of the model to simulate DC polarization into the nonlinear range. A more general, two-dimensional model of the Pt, O₂|YSZ system will address these shortcomings and allow DC polarization and impedance experiments of various geometries to be fitted using a single model.

Chapter 2

PROCEDURE

2.1 General Modeling Approach

The majority of the present work was based upon numerical simulation of electrochemical experiments. In most cases, the desired end results included a simulated impedance spectrum, which is of use for both stand-alone parametric studies and fitting of experimental data. The impedance modeling followed the basic framework employed by Fleig et al.,^{49,54} with added complexity to deal with non-ideality of the electrolyte microstructure, electrode, and electrode-electrolyte interface. An electrochemical cell similar to those employed in previous experimental studies,²⁰ which is typical of the geometries considered here, is shown schematically in Figure 13a. The geometry consists of a thin, solid electrolyte film deposited on a chemically inert substrate, with interdigitated platinum electrodes patterned on the top surface of the electrolyte. An AC potential is applied between the electrodes. Assuming the electrode fingers are long enough for edge effects to be negligible, the geometry can be simplified to two dimensions by considering the cross-sectional plane indicated in Figure 13b. Making use of mirror and translational symmetries in the sample geometry, the model domain can be further simplified as shown in Figure 13c. Finally, as the potentials applied to the two electrodes are equal in magnitude but opposite in polarity, the antisymmetry of the sample may be taken advantage of by bisecting the model domain to obtain the geometry shown in Figure 13d. It is evident by inspection that the potential along the right border (*CD*) is zero.

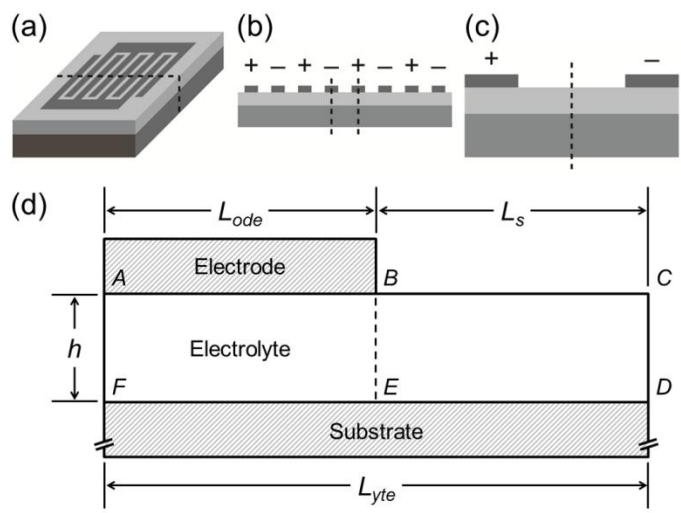


Figure 13. Schematic of a thin film electrochemical cell with interdigitated microelectrodes. The 3D geometry (a) can be reduced to the 2D geometry (d) as shown by slicing along the dashed lines shown in parts (a), (b), and (c).

The two-dimensional model geometry shown in Figure 13d was modeled in the time domain, with appropriate modifications for each individual study, using COMSOL Multiphysics (v. 4.3a and 4.4, COMSOL AB). The general approach was to solve for the electrical potential and current density within the domain considering externally applied electrical and/or chemical driving forces. The current density and potential were related using Ohm's law where applicable, assuming that the IV relationship remains in the linear range (as is the case for small-signal impedance measurements). In more complex cases the current density was calculated independently by solving mass transport equations. The impedance could then be determined by transforming the current and potential to the frequency domain, or in simpler cases directly in the time domain using complex-valued variables. Complete impedance spectra were obtained by repeating the solution process over a range of

frequencies. The specific equations and boundary conditions used in each modeling study will be detailed in the following sections.

2.2 Grain Boundary Heterogeneity Study

The first study to be undertaken concerned the electrical behavior of polycrystalline electrolytes. The study aimed to address the first two questions raised in Section 1.4: first, to what extent heterogeneous grain boundary conductivity and/or permittivity cause depression of the grain boundary arc in the AC impedance spectrum, and second, whether the degree of heterogeneity can be measured or estimated using CPE equivalent circuit parameters. These questions were investigated quantitatively for the first time.

2.2.1 Model Framework

Impedance spectra for arbitrary polycrystalline electrolyte geometries were created using the modeling domain shown schematically in Figure 14. Since the present study is concerned solely with electrolyte effects, this geometry has been simplified in a number of respects compared to Figure 13. First, the electrodes were placed on opposite surfaces of the electrolyte in a sandwich layout rather than having both electrodes interdigitated on the same surface. This allows the effects of grain boundary heterogeneity to be easily visualized since the current path in the homogeneous case is strictly one-dimensional. Additionally, both electrodes were assumed to be ideally non-polarized and the substrate was neglected in order to focus solely on the electrolyte behavior.

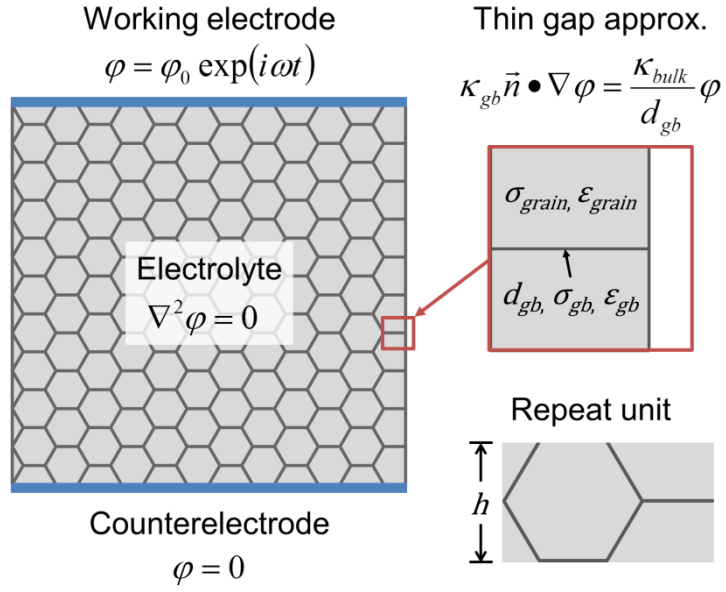


Figure 14. Schematic of the two-dimensional modeling domain illustrating the polycrystalline electrolyte geometry, key model parameters, and boundary conditions.

Following the method of Fleig et al., the complex electrical potential $\varphi(x,y,t)$ within the two-dimensional domain was obtained by direct numerical solution of Laplace's equation

$$\nabla^2 \varphi = 0 \quad (10)$$

subject to appropriate internal and external boundary conditions. In arriving at (10), it was assumed that diffuse space charges can be neglected.⁷³ An electrical driving force was specified in the form of an AC potential applied at the working electrode, which was chosen as the top surface in the model. The boundary condition at this surface was therefore taken as

$$\varphi = \varphi_0 \exp(i\omega t) \quad (11)$$

where φ_0 is the amplitude of the applied potential. Here φ_0 was set at 20 mV, which is typical of EIS experiments.²⁵ The counter-electrode (chosen here as the bottom surface) was kept grounded,

$$\varphi = 0 \quad (12)$$

and the free (side) surfaces of the electrolyte were assumed to be perfectly insulating according to

$$\vec{n} \cdot \nabla \varphi = 0 \quad (13)$$

where \vec{n} is the unit vector normal to the surface in question. Once the potential distribution was calculated, the current density distribution J was calculated from

$$J = -\kappa \nabla \varphi \quad (14)$$

with the complex conductivity κ defined as

$$\kappa = \sigma + i\omega\varepsilon\varepsilon_0 \quad (15)$$

where σ and ε are positive, real values representing the conductivity and relative permittivity, respectively, and ε_0 is the permittivity of free space. Equation 14 is valid when the relationship between current and potential is linear, which is the case in nearly all EIS experiments since the applied potential is small. The total current (per unit of out-of-plane thickness) could then be obtained by integrating over an equipotential surface ES :

$$I = \int_{ES} J \cdot ds \quad (16)$$

For convenience, the grounded surface was chosen as the surface of integration.

Finally, the complex impedance Z was calculated from

$$Z = \frac{\varphi_0}{I} \quad (17)$$

Due to the two-dimensional nature of the model, the impedance calculated by this method has units of $\Omega \cdot \text{m}$. Impedance spectra were obtained by repeated application of (10)–(17) at 13 selected frequencies from 0.1 Hz to 1 GHz. This number of data points was chosen in order to maintain a balance between accuracy and solution time.

The electrolyte microstructure was modeled in two dimensions as an array of uniform hexagonal grains. Unlike the square brick layer geometry described in Section 1.2.1, this hexagonal grain structure satisfies the interfacial equilibrium condition in two dimensions and was thus considered to be a better representation of a realistic polycrystal.^{49,99} Still, the geometry is simple enough that the grain boundary resistance and capacitance can be calculated analytically. The grain boundary geometry was constructed using the repeat unit in Figure 14 and oriented as shown with the minimal grain dimension perpendicular to the electrode surfaces. The samples were defined to be as square as possible without introducing any partial repeat units, which would complicate analytical determinations of the net resistance, R_{gb} , and capacitance, C_{gb} , of the grain boundary array. This resulted in a 5:6 ratio between the numbers of grains in the y - and x -directions, respectively, and an overall sample aspect ratio $H_y / H_x = 0.96$ where H_x is the in-plane width and H_y is the electrode-to-electrode thickness.

The grain boundaries were modeled using the internal boundary condition

$$\kappa_{gb} \hat{n} \cdot \nabla \varphi = \frac{\kappa_{grain}}{w_{gb}} \varphi \quad (18)$$

where w_{gb} is the grain boundary thickness and the grain boundary conductivity, κ_{gb} , can be quantitatively different from the grain conductivity, κ_{grain} (both are complex valued and defined as in Equation 15). This “thin gap” condition is derived from the

continuity of normal current across the grain-boundary interface, making the assumption that components of current parallel to the boundaries are negligible. The approximation is therefore valid when the thickness of the grain boundary is uniform and much smaller than the boundary length. In addition, this boundary condition requires that $\sigma_{gb} < \sigma_{grain}$ since current parallel to the grain boundaries cannot be neglected otherwise.

If the grain boundaries are homogeneous, and edge effects are ignored, the net grain boundary resistance⁴⁹ of the electrolyte geometry shown in Figure 14 can be derived analytically as

$$R_{gb} = \frac{n_y}{n_x} \frac{w_{gb}}{\sqrt{3}h\sigma_{gb}} \quad (19)$$

where h is the minimal diameter of the hexagonal grain (giving a side length of $h/\sqrt{3}$), n_y and n_x are the number of repeat units across the total thickness and width of the sample, respectively, and w_{gb} is the grain boundary width. With the additional introduction of the overall sample aspect ratio H_y / H_x , the mean conductivity can then be estimated from

$$\sigma_{gb} = \frac{H_y}{H_x} \frac{w_{gb}}{hR_{gb}} \quad (20)$$

where, as before, h is the minimal grain diameter. (For a three-dimensional specimen with prismatic grains, H_x is replaced by the cross-sectional area A .)

The net grain boundary capacitance can also be analytically solved, yielding the expression

$$C_{gb} = \frac{n_x}{n_y} \frac{\sqrt{3}h\epsilon_{gb}}{w_{gb}} \quad (21)$$

Thus, the permittivity can be calculated from the capacitance by

$$\varepsilon_{gb} = \frac{H_y}{H_x} \frac{w_{gb} C_{gb}}{h} \quad (22)$$

In the absence of more detailed information about the heterogeneity of the grain boundary properties, an experimentalist would have little choice but to use (20) and (22) to calculate a single-valued grain boundary conductivity and permittivity from an experimentally determined resistance and (pseudo-)capacitance.

2.2.2 Material Properties

The properties of the grain interiors were defined to be homogeneous, with $\sigma_{grain} = 10^{-4}$ S/m and $\varepsilon_{grain} = 25$. These values are typical of YSZ at moderate temperature.^{100,101} In the homogeneous case, the grain boundary properties were $\sigma_{gb} = 10^{-7}$ S/m and $\varepsilon_{gb} = 25$. For cases where σ_{gb} and/or ε_{gb} were heterogeneous, each grain boundary was assigned a random value of the parameter(s) in question according to a pre-selected distribution. For each trial of the simulation, a list of random values was generated for each heterogeneous parameter using the inverse cumulative density function of the specified distribution, and these values were then assigned to the grain boundaries on a one-to-one basis. Different distribution functions were chosen for σ_{gb} and ε_{gb} . For grain boundary conductivity, a normal or log-normal distribution was considered intuitively appropriate and is consistent with Fleig's work.^{46,51} The conductivity in the present work was therefore assigned according to a log-normal distribution with a population mean of 10^{-7} S/m. The standard deviation of $\log(\sigma_{gb})$ varied between 0 and 1. Probability density functions for a few representative values of the population standard deviation, each with a corresponding sample distributions of grain boundary conductivities, are shown in Figure 15a.

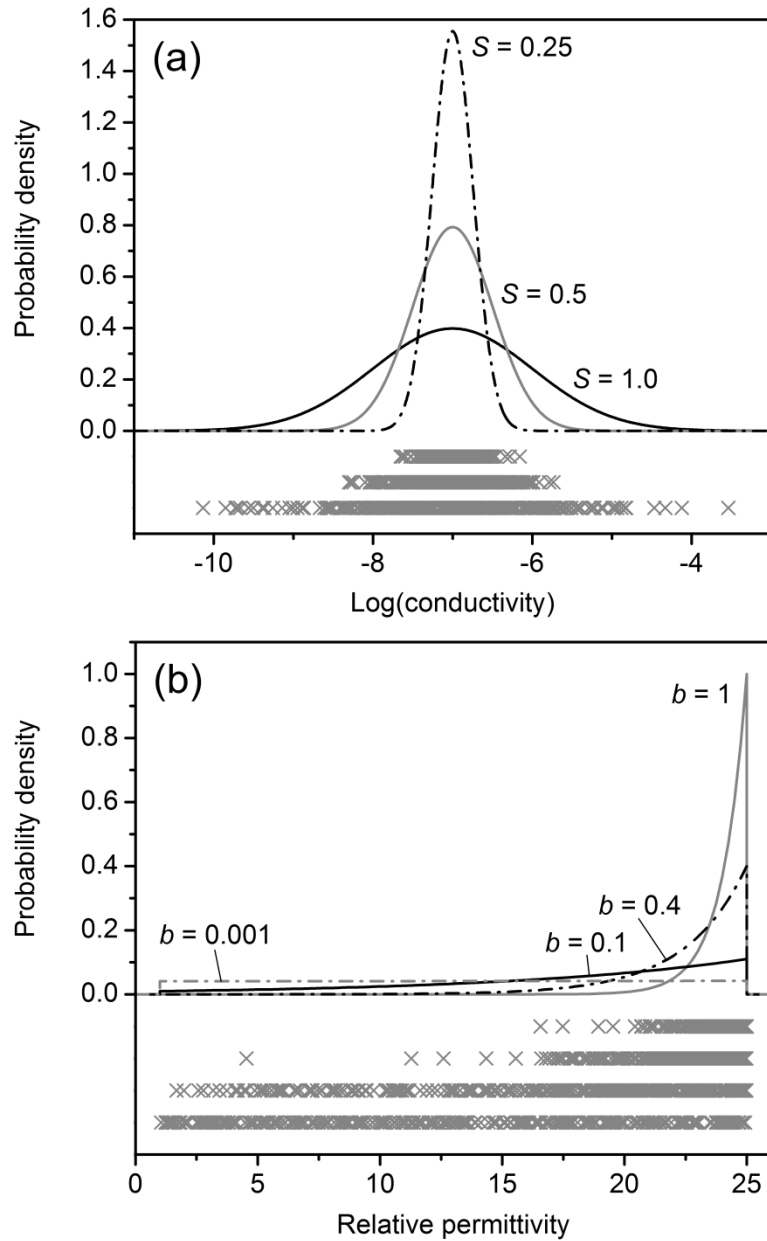


Figure 15. Selected probability density functions for distributions of (a) grain boundary conductivity (with population standard deviations S indicated) and (b) grain boundary permittivity used in the model (with the values of distribution parameter b indicated). Also included, below the PDF plots, are sample sets of grain boundary parameters corresponding to each of the distribution functions shown.

The permittivity was distributed according to an exponential probability density function of the form

$$y = a \exp(bx) \quad (23)$$

with functional bounds such that $1 \leq \varepsilon_{gb} \leq 25$. In the limit of large b , the distribution approaches the ideal case where all grain boundaries have $\varepsilon_{gb} = 25$. At the other limit, as b approaches zero, the grain boundary permittivities are uniformly distributed between 1 and 25. Distributions for a few representative values of the distribution parameter b are shown in Figure 15b. The value of a was adjusted as necessary so that

$$\int_1^{25} y(x) dx = 1 \quad (24)$$

as required for a probability density function. As grain boundaries are distinguished by reduced ion and bound electron density relative to the grain, it was assumed that the grain boundary permittivity could approach but not exceed the grain permittivity. In studies where equivalent circuit fitting is employed,⁶³ the grain boundary permittivity is often assumed equal to that of the bulk grain. However, studies on single grain boundaries¹⁰² have shown a variation in capacitance with lattice mismatch angle, so it is reasonable to conclude that some grain boundaries have a lower permittivity than the bulk material assuming the grains have non-uniform orientation. Therefore the exponential distribution just described was used to quantify heterogeneous grain boundary permittivity.

One additional grain boundary parameter considered in the present model is the thickness w_{gb} . The case of heterogeneous grain boundary thickness was not considered here since according to (18) the effect is expected to be equivalent to that of simultaneous heterogeneity of conductivity and permittivity. Instead, homogeneous thicknesses were used in all cases. The grain boundary thickness was taken as 1 nm,

which is close to values reported for YSZ using both impedance spectroscopy and transmission electron microscopy.¹⁰³

2.2.3 Impedance Spectra

The simulation procedure detailed in Sections 2.2.1 and 2.2.2 was applied repeatedly to generate an appropriately sized dataset for each of three potential cases of grain boundary heterogeneity. These consisted of specimens with (1) heterogeneous conductivity and homogeneous permittivity, (2) homogeneous conductivity and heterogeneous permittivity, and (3) heterogeneous conductivity and permittivity. The simulated impedance spectra were imported into ZView (v. 3.2d, SAI) to perform fitting to the CPE equivalent circuit model shown in Figure 8. The relationships between the equivalent circuit parameters related to the grain boundary arc— R_{gb} , Q_{gb} , and n_{gb} —and the grain boundary conductivity and permittivity distribution parameters were of particular interest.

Results were compiled for three different grain sizes: 1 μm , 500 nm, and 250 nm. The total specimen thickness was 10 μm ; thus an electrolyte cross-section parallel to the current direction in each case contained 10, 20, and 40 grains, respectively. A triangular mesh was used, which was a natural choice based on the hexagonal grain geometry. For each grain size, the mesh was refined in order to achieve an acceptable accuracy of the conductivity and permittivity results in the analytically solvable homogeneous case while still maintaining a practicable computation time. The error in apparent grain boundary parameters was less than 2% for 1 μm grains, less than 3% for 500 nm grains, and less than 5% for 250 nm grains. Due to computational limitations, fewer trials were conducted for the 250 nm grain size, and smaller sizes were not studied.

2.3 Phenomenological Electrode Modeling Study

In order to make the model presented in Section 2.2 more useful for experimental work, it was extended to consider not just the electrolyte impedance but also that of the electrode, which cannot be avoided in a practical experimental study. A key goal of the study was investigating the third question listed in Section 1.4, concerning the origin of an anomalous intermediate frequency impedance feature observed in experimental studies of thin film electrochemical cells with interdigitated surface microelectrodes. Since part of the purpose of the study was to fit experimental data, the actual as-fabricated geometry of the previously reported cells was modeled as closely as possible, including the electrodes and substrate. This allowed the model parameters to be quantified from the experimental samples.

2.3.1 Model Setup

The electrochemical cell was modeled using the 2D geometry shown in Figure 13. Unlike in Section 2.2, the model includes both the electrode and substrate in a geometry replicating the actual specimens reported in Reference 20. While the substrate was considered to have negligible DC conductivity compared to the electrolyte film, it may still provide non-negligible dielectric conduction. As the focus of this study was the behavior of the electrode, grain boundaries were not considered and the electrolyte was assumed to be a single-crystal material.

The impedance of the system was determined in much the same manner as described in Section 2.2. The modeling approach was modified by solving directly for current, instead of potential, in order to facilitate the use of boundary conditions given explicitly in terms of current. As experimental impedance studies, and thus the present modeling work, are performed strictly in the linear I-V range, any effect of this

modification on the model output is negligible. In the absence of any current sources or sinks, the current density J in the model domain is governed by

$$\nabla \cdot J = 0 \quad (25)$$

Since this experiment is within the linear range, the electrical potential and current density can be related using (14). A complex conductivity κ was implemented in the same manner as before according to (15). The boundary conditions used in the model are shown in Figure 16. The AC potential given by (11) is applied at the top surface of the electrode. At the right electrolyte boundary (labeled CD in Figure 13), the potential is governed by (12) due to the symmetry of the cell. All other exterior boundaries were considered to be insulating to current flow with

$$\hat{n} \cdot J = 0 \quad (26)$$

As a consequence of the above formulation, both φ and J are complex quantities.

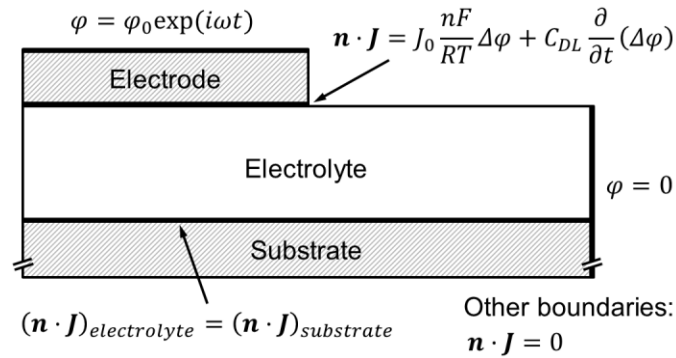


Figure 16. Model boundary conditions. All unlabeled boundaries obey the zero current condition given by (26).

Difficulty arises in the modeling of the electrode-electrolyte interface, since even for model systems (e.g. Pt,O₂|YSZ) the electrochemical reactions involved are

not yet completely understood.⁴ However, studies of platinum electrodes on solid oxide electrolytes²³ have demonstrated that the current-overpotential relationship in such electrodes can be modeled using the well-known Butler-Volmer equation from classical aqueous electrochemistry. Later work has shown that the electrode polarization is controlled largely or entirely by processes other than electrochemical charge transfer,^{4,26,28} and thus the physical basis for Butler-Volmer kinetics is lacking. Nevertheless, the mathematics remain useful phenomenologically, and researchers have compiled values of the exchange current density for Pt/O₂/YSZ and other systems under various experimental conditions.²⁸ As the focus of the present work at this preliminary stage is not a detailed microscopic understanding of the electrode kinetics, a phenomenological approach will suffice. Therefore the electrode-electrolyte interface will be modeled using Butler-Volmer kinetics, and the exchange current density treated as a strictly empirical parameter.

As per the previous discussion, the current-potential relationship at the electrode is governed by (3). However, since EIS experiments are generally performed with a small signal amplitude φ_0 in order to remain in the linear range of the I-V curve, (3) in this case can be replaced with a much simpler linearized form¹⁰⁴

$$J = J_0 \frac{zF}{RT} \eta \quad (27)$$

where, as before, J_0 is the exchange current density, z is the charge number, F is the Faraday constant, R is the molar gas constant, T is absolute temperature, and η is the overpotential. The charge transfer coefficient α does not appear in the linearized form of the equation as the I-V relationship is independent of α in the low-overpotential region.¹⁰⁴ Due to the symmetry of the electrochemical cell, the equilibrium potential of the electrodes can be neglected and η taken as simply the potential difference $\Delta\varphi$

across the interface. The temperature T was treated as a constant parameter, assuming the sample is thermally equilibrated and neglecting any Joule heating due to current flux. The latter assumption was considered to be reasonable for the geometry considered here as the electrical potentials involved are only in the millivolt range and the volume of the electrolyte is very small relative to its surface area, allowing for effective cooling. Further, the maximum current flux occurs in a region very near the free surface of the electrolyte, enabling the heat generated to dissipate easily. This was further justified using a simple DC electrostatic/heat transfer model of the electrolyte, which predicted negligible temperature change for YSZ even under worst case conditions (poor convection at the free surface and complete thermal insulation at all other boundaries including the electrolyte-substrate interface).

In addition to the Faradaic current flux represented by (27), displacement current across the interface was considered by incorporating a double layer capacitance with current density

$$J = C_{DL} \frac{\partial \eta}{\partial t} \quad (28)$$

The parameter C_{DL} should be thought of as a phenomenological descriptor of the capacitive properties of the electrode-electrolyte interface rather than a literal double layer capacitance, as the capacitance of the platinum/solid oxide interface is thought to arise from chemical processes rather than a classical double layer mechanism^{4,59,105}. Nevertheless, a phenomenological treatment is adequate for the present work. Combining (27) and (28), the boundary condition at the electrode-electrolyte interface can be expressed as

$$\hat{n} \cdot J = J_0 \frac{zF}{RT} \Delta\varphi + C_{DL} \frac{\partial}{\partial t} (\Delta\varphi) \quad (29)$$

At the interface between the electrolyte and substrate, the model requires continuity of the normal component of the complex current density

$$(\hat{n} \cdot J)_{electrolyte} = (\hat{n} \cdot J)_{substrate} \quad (30)$$

The substrate is given negligible DC conductivity but finite permittivity allowing for capacitive currents.

For any single value of frequency, the time- and space-dependent current and potential distributions are determined by solving (25) subject to the boundary conditions (11), (12), (26), (29), and (30), and the initial condition

$$\varphi = 0 \quad (31)$$

everywhere in the domain. After determining the current distribution, the total current through the specimen can be calculated using (16) with the antisymmetry boundary CD taken as the equipotential surface of integration. The complex impedance Z of the specimen can then be determined from (17). The value of Z was calculated at time $t = 2/f$, i.e. after two AC cycles. It was determined that this was sufficient to limit any transient fluctuations in the magnitude of Z to less than 0.01%. The full impedance spectrum was then obtained by repeating the above process over a range of frequency values. The frequencies of interest typically ranged from mHz to MHz with 10 data points per frequency decade. In order to accommodate this wide frequency range, the time step used in each simulation was adjusted to maintain an equal number of time steps per AC cycle regardless of frequency. It was determined that 10 time steps per cycle was sufficient to accurately calculate the impedance.

2.3.2 Mesh

For the present study, a quadrilateral mesh with 17,500 elements was selected in order to balance solution accuracy with computation time. The elements were mapped so that the mesh was much finer in the electrode and electrolyte layers than in the substrate. By performing a mesh convergence study, the maximum error in the calculated impedance magnitude (after two AC cycles) using the mapped mesh was estimated at 0.01% at 0.01 Hz and 1% at 300 MHz.

2.3.3 Fitting Procedure

One of the key purposes of the finite element modeling performed here was comparison of the resulting calculated impedance spectra to previously measured experimental spectra. This procedure is sometimes complicated by experimental data generally suffering from poorer resolution at measurement frequencies below approximately 0.1 Hz. In such cases, a least-squares fitting procedure can yield a poor estimate of the low frequency arc parameters. Instead, the fitting procedure maintained equal radii between the low frequency arc in the experimental spectrum and the fitted model results. The fitting procedure allowed the parameter values ε and C_{DL} to be estimated with a resolution of ± 0.1 (dimensionless) and $\pm 1 \mu\text{F}/\text{cm}^2$, respectively. The values of σ and J_0 derived from the fitting procedure were within 1% of the values derived from an equivalent circuit fit to the same experimental data, demonstrating the robustness of the graphical fitting procedure.

2.3.4 Experimental

Data from previously reported experimental work on thin film Pt/YSZ and Pt/GDC electrochemical cells^{20,55} were used for validation of this portion of the work. The samples were fabricated by patterning dense, interdigitated platinum microelectrodes

onto sputtered YSZ and GDC films using photolithography. While the samples measured in References 20 and 55 are similar in geometry and materials set, it should be noted that they were created and measured in different labs and on different equipment. The details of the fabrication and impedance characterization processes used in these studies have been reported elsewhere.^{13,55} The sample properties relevant to the present work are given in Table 1. Impedance spectra were collected for each sample in air. The YSZ specimens were measured using a Solartron 1260 impedance analyzer over a frequency range of 0.01–10⁷ Hz at 333–394°C with a signal amplitude of 20 mV, while the GDC specimens were measured using a Novocontrol Alpha impedance analyzer over a frequency range of 0.01–3×10⁶ Hz at 401–652°C with a signal amplitude of 1 mV.

Table 2. Properties of the Pt/YSZ and Pt/GDC samples

	Pt/YSZ	Pt/GDC
Electrode material	Pt	Pt
Electrode finger width	25 μm	25 μm
Electrode finger spacing	25 μm	25 μm
Electrolyte material	Zr _{0.91} Y _{0.09} O _{1.95}	Ce _{0.8} Gd _{0.2} O _{1.9}
Electrolyte thickness	100 nm	30 nm
Substrate	Amorphous SiO ₂	Single crystal Al ₂ O ₃ (0001)

2.4 Diffusion-Reaction Electrode Modeling Study

The model discussed in Section 2.3 the previous section was subsequently modified to include a more realistic treatment of the electrode reaction. Rather than merely adopting a phenomenological approach based on a Butler-Volmer current-potential relationship, the extended model incorporated separate adsorption, diffusion,

and charge transfer processes in an effort to model the actual physical processes at the TPB. In order to facilitate modeling of these processes, the overall model formulation was modified from a current-based framework to a Poisson-Nernst-Planck (PNP) formulation considering concentrations and fluxes of mobile species explicitly. The goal of this study was to make a first step in addressing points 4 and 5 from Section 1.4; that is, clarifying the both the reaction mechanism and geometric effects in the thin film Pt, O₂|YSZ system.

2.4.1 Model Setup

The three-dimensional microelectrode geometry to be modeled is the same as in Section 2.3, and is again reduced to a two-dimensional domain as shown in Figure 13a–c. The simplified model geometry is shown in Figure 17. As may be observed from the figure, two thin layers *ABD* and *CD* have been implemented at the electrode surface and electrode-electrolyte interface, respectively. This allows processes occurring strictly on planar surfaces, such as diffusion of adsorbed oxygen on the electrode surface, to be modeled in a manner that remains compatible with the overall two-dimensional formulation. The inclusion of these finite-thickness layers for computational reasons can be justified physically by considering that solid surfaces are not perfectly smooth and thus behave to some extent as continua having a thickness comparable to the surface roughness. Characterization of sputtered YSZ thin films¹⁰⁶ has shown that the surface roughness of such films is on the order of 1–10 nm; this is assumed to be an appropriate magnitude for surface and interfacial layer thickness in the model. The effect of the surface layer thickness will be explored later.

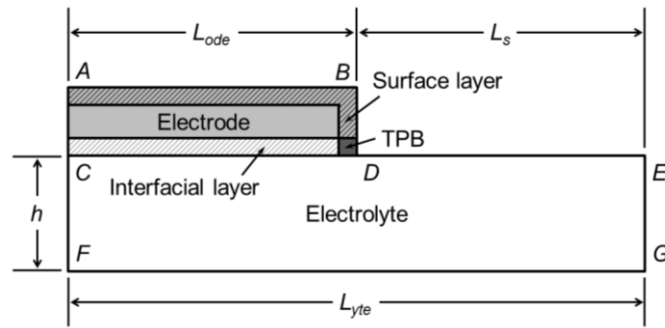


Figure 17. Model domain. Thickness of surface and interfacial layers has been exaggerated for visibility.

At the present stage, the modeling will be confined to a single set of atmospheric parameters (T, P_{O_2}) typical of standard SOFC operation: $T = 500^\circ\text{C}$ and $P_{O_2} = 0.21 \text{ atm}$. As shown earlier in Figure 1, the generalized electrode reaction potentially involves a large number of distinct physical processes. In order to develop a more practical model, a number of simplifying assumptions are made:

(1) Oxygen adsorbs dissociatively on the electrode surface in a single-step reaction. In reality, oxygen adsorption on platinum is quite complex and may involve adsorbed molecular O_2 species in addition to monatomic O ,¹⁰⁷ as well as other charged and neutral adsorption intermediates.³³ However, the use of assumption (1) is well established in the literature²⁸ and the potential benefit of explicitly modeling any intermediate adsorption processes is not expected to be worth the cost incurred by bringing additional, difficult-to-quantify parameters into the model.

(2) Transport of adsorbed oxygen to the TPB proceeds via the surface path; i.e. transport of oxygen through the electrode interior, or along grain boundaries, is negligible. This is in keeping with the findings of Robertson and Michaels, who demonstrated experimentally that the charge transfer reaction occurs at the TPB.¹⁷

Reported diffusion coefficients for oxygen in platinum⁵⁸ (extrapolated from high temperature) are on the order of 10^{-26} m²/s at 500°C. This is around 14 orders of magnitude less than the surface diffusivity and can safely be neglected.

(3) The concentration of adsorbed oxygen species in the electrolyte and on the electrolyte surface is negligible. It has been reported that oxygen vacancies in YSZ can provide active sites for O₂ adsorption.¹⁰⁸ However, the vacancy concentration at the YSZ surface is small relative to the concentration of adsorption sites on the platinum electrode, so it is assumed that oxygen adsorption on the electrolyte surface is inconsequential to the present study. Additionally, the experiments of Opitz et al. showed that the electrode active area does not extend onto the free electrolyte surface in the case of low overpotential.^{21,22}

(4) Transport of electrons and/or holes in the electrolyte is negligible. Under the ambient conditions considered here ($P_{O_2} = 0.21$ atm and $T = 500^\circ\text{C}$), YSZ has a mobile electron concentration on the order of 10^{-8} mol/m³ and a mobile hole concentration on the order of 0.1 mol/m³,¹⁰⁹ which can indeed be considered negligible compared to the other species concentrations on the order of 10^3 – 10^4 mol/m³. For ambient conditions with very high P_{O_2} , the hole concentration may become significant, and similarly the electron concentration may become significant in the case of very low P_{O_2} . Electronic conduction may also play a significant role in other electrolyte materials, such as ceria. Since these types of studies may be of interest in the future, the model is formulated in such a way that electron and/or hole conduction in the electrolyte can be added with a minimum of difficulty.

(5) Concentration overpotential is negligible; i.e. any resistive effect of gas-phase diffusion can be ignored. Diffusion of oxygen in the gas phase can be rate

limiting for $P_{O_2} \leq 10^{-3}$ atm or $T \geq 750^\circ\text{C}$ ³³ but is not expected to have a significant effect for the ambient conditions studied here. Gas phase diffusion may need to be included if the model is extended to higher temperature or lower P_{O_2} cases.

(6) Impedance of electron conduction through any connecting wires is negligible.

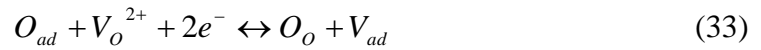
With these assumptions, the electrode reaction as modeled proceeds via a three-step process: (1) dissociative adsorption of oxygen gas onto the electrode surface, (2) diffusive transport of adsorbed oxygen to the TPB, and (3) incorporation of adsorbed oxygen into the electrolyte lattice via charge-transfer reaction. The model framework is based on a Poisson-Nernst-Planck formulation which considers species transport, chemical reactions, and electrostatics. Transport of mobile species via diffusion and migration, as well as their generation and/or annihilation due to chemical reactions, are modeled using the Nernst-Planck equation

$$\frac{\partial c_i}{\partial t} + \nabla \cdot \left[-D_i \nabla c_i - z_i D_i c_i \frac{F}{RT} \nabla \varphi \right] = \sum_j r_{ij} \quad (32)$$

where F is the Faraday constant, R is the gas constant, T is the absolute temperature, φ is the electrical potential, and c_i , z_i , and D_i are the concentration, charge number, and diffusivity, respectively, of the i th species. In the present case, three mobile species are considered: oxygen vacancies, electrons, and adsorbed oxygen. Their concentrations, which constitute the dependent variables of the set of three governing equations, are denoted c_V , c_e , and c_O , respectively. The equation is valid as long as species concentrations are low enough that any interaction between particles is negligible. In order to ensure segregation of species in accordance with the model assumptions, diffusion barriers were implemented in the model to restrict adsorbed oxygen to the

electrode surface layer ABD and oxygen vacancies to the electrolyte and interfacial layer CD . As a consequence, the charge transfer reaction is restricted to the TPB region, which is the only area accessible to both species.

The summed term on the right-hand side of (32) describes the generation or annihilation of species i due to one or more chemical reactions j . The form of this reaction term depends on the reaction(s) involved. Two reactions are considered in the model. The first is the charge transfer reaction



whereby an oxygen atom adsorbed on the electrode surface is reduced and fills a vacancy in the electrolyte lattice. The reaction proceeds in the forward direction at the cathode and in the reverse direction at the anode. In (33), O_o represents a filled oxygen site in the electrolyte and V_{ad} represents a vacant adsorption site on the electrode. The rate equation corresponding to (33) is given by

$$r_1 = k_1 c_{OO} c_{V_{ad}} - k_{-1} c_V c_O \quad (34)$$

where k_1 and k_{-1} are the anodic and cathodic rate constants, respectively, c_{OO} is the concentration of filled oxygen sites in the electrolyte, and $c_{V_{ad}}$ is the concentration of vacant adsorption sites on the electrode. The reaction rate is assumed to be independent of electron concentration, which is an order of magnitude larger than the other species concentrations and thus unlikely to limit the reaction in any way. The rate equation can be simplified by making the observation that the total number of oxygen sites is a fixed property of the electrolyte; that is,

$$c_{OO} = c_{SO} - c_V \quad (35)$$

where c_{SO} is the constant concentration of oxygen sites. The number of adsorption sites on the electrode is also fixed, giving

$$c_{Vad} = c_{Sad} - c_O \quad (36)$$

where c_{Sad} is the constant total concentration of adsorption sites. Substituting (35) and (36) into (34) allows c_{OO} and c_{Vad} to be eliminated from the rate equation, yielding an expression in terms of the dependent variables:

$$r_1 = k_1(c_{SO} - c_V)(c_{Sad} - c_O) - k_{-1}c_Vc_O \quad (37)$$

The rate constants are expressed in the well-known Butler-Volmer form,

$$k_1 = k_1^0 \exp\left(\frac{\beta F z_V}{RT} \eta(t)\right) \quad (38)$$

and

$$k_{-1} = k_{-1}^0 \exp\left(-\frac{(1-\beta)F z_V}{RT} \eta(t)\right) \quad (39)$$

where k_1^0 and k_{-1}^0 are the equilibrium rate constants, β is a symmetry factor, and $\eta(t)$ is the overpotential as defined by (4). The symmetry factor is taken as 0.5 per common practice.¹¹⁰ Since the anode and cathode are identical, and the absolute potential is arbitrary, the equilibrium potential may be taken as zero so that $\eta(t)$ is equal to the applied potential. The half cell operates as a cathode when the applied potential is negative, and as an anode when the applied potential is positive. It should be noted that (38) and (39) have not been linearized, and thus the electrode model is expected to remain valid into the nonlinear I-V range, making it suitable for DC polarization studies as well as small-signal impedance.

The rate constants k_1 and k_{-1} are not independent. At zero overpotential the electrode reaction is in equilibrium, and thus the anodic and cathodic reaction rates must be equal. When $\eta = 0$, the exponential parts of (38) and (39) reduce to unity and the equilibrium condition can be expressed as

$$k_1^0 [(c_{SO} - c_V)(c_{Sad} - c_O)]_{eq} = k_{-1}^0 [c_V c_O]_{eq} \quad (40)$$

where the subscript *eq* denotes that all of the concentrations shown are those at equilibrium. Since the oxygen reduction occurs at the cathode in an SOFC, it seems logical to take the cathodic rate constant as the independent parameter. Rearranging (40) to solve for k_1^0 yields

$$k_1^0 = k_{-1}^0 \left[\frac{c_V c_O}{(c_{SO} - c_V)(c_{Sad} - c_O)} \right]_{eq} \quad (41)$$

which eliminates k_1^0 as an independent parameter.

The second reaction considered is the adsorption of oxygen onto the electrode



According to the Langmuir model for dissociative adsorption, the rate equation for this reaction is given by

$$r_2 = k_2 P_{O_2} (1 - \theta)^2 - k_{-2} \theta^2 \quad (43)$$

where θ is the fraction of occupied adsorption sites on the electrode surface; that is,

$$\theta = \frac{c_O}{c_{Sad}} \quad (44)$$

The adsorption rate coefficient k_2 can be related to more specific physical properties using the Hertz-Knudsen equation¹¹¹

$$k_2 = \frac{S}{\sqrt{2\pi MRT}} \quad (45)$$

where S is the sticking coefficient, or probability that an O_2 molecule impinging on the surface will be adsorbed, and M is the molar mass. The maximum sticking coefficient (measured around 300°C¹¹²) is approximately 0.15, corresponding to $k_2 = 0.0041$

mol·s/(kg·m²). The Langmuir model assumes that all adsorption sites are identical and that interactions between adsorbed species are negligible. There is some evidence that the latter assumption is not necessarily valid for oxygen on platinum, and therefore both the adsorption rate constants and the diffusivity of adsorbed oxygen may be functions of adsorbate concentration.³³ However, the concentration of adsorbed oxygen is not expected to vary much in the present case due to the low overpotentials involved, so it will be assumed that k_2 , k_{-2} , and D_o can be treated as constants. The validity of this assumption will be discussed in Section 3.3.1.3. The oxygen partial pressure is assumed to be high enough that the resistive contribution of O₂ diffusion is negligible, allowing P_{O_2} to be taken as a constant parameter. This assumption is justified under atmospheric conditions but may not hold for very low P_{O_2} , where the electrode reaction can become limited by gas phase diffusion. As before, the equilibrium condition

$$k_{-2} = k_2 P_{O_2} \left[\frac{(1-\theta)^2}{\theta^2} \right]_{eq} \quad (46)$$

can be invoked to relate the forward and reverse rate constants. With the above considerations, the three equations governing species concentrations are

$$\frac{\partial c_v}{\partial t} + \nabla \cdot \left[-D_v \nabla c_v - 2D_v c_v \frac{F}{RT} \nabla \varphi \right] = r_1 \quad (47)$$

$$\frac{\partial c_e}{\partial t} + \nabla \cdot \left[-D_e \nabla c_e + D_e c_e \frac{F}{RT} \nabla \varphi \right] = 2r_1 \quad (48)$$

and

$$\frac{\partial c_o}{\partial t} + \nabla \cdot \left[-D_o \nabla c_o \right] = r_1 + r_2 \quad (49)$$

Concentration boundary conditions are implemented as follows. At the symmetry boundary EG it is assumed that oxygen vacancies can migrate back and forth across the boundary to maintain a constant concentration, giving rise to the condition

$$c_v = c_{v0} \quad (50)$$

Similarly, at the upper electrode surface AB , it is assumed that the electron concentration remains constant:

$$c_e = c_{e0} \quad (51)$$

All other boundaries obey a zero flux condition

$$\hat{n} \cdot \Phi_i = 0 \quad (52)$$

where Φ_i is the flux of the i th species, given by

$$\Phi_i = -D_i \nabla c_i - \frac{F}{RT} z_i c_i \nabla \varphi \quad (53)$$

The presence of the electrical potential φ in (47)–(49) requires another governing equation to solve for the potential distribution in the model domain. This is Poisson's equation

$$-\varepsilon \varepsilon_0 \nabla^2 \varphi = F \sum_i z_i c_i \quad (54)$$

where the right-hand side is a space charge term related to the concentrations of charged species. The current model has two mobile charged species, oxygen vacancies ($z = +2$), and electrons ($z = -1$). The immobile countercharge is supplied by yttrium ions on zirconium sites, which have an effective charge of -1 , and platinum cores with an effective $+1$ charge. Since the electrolyte at equilibrium is electrically neutral, the concentration of the immobile yttrium ions is equal to twice the equilibrium concentration of vacancies. Similarly, the electrode is neutral at equilibrium and so the

concentration of positively charged platinum cores is equal to the equilibrium electron concentration. With these substitutions, (54) can be expressed as

$$-\varepsilon\varepsilon_0\nabla^2\varphi = F[2(c_V - c_{V0}) - (c_e - c_{e0})] \quad (55)$$

The electrical boundary conditions are an applied AC potential

$$\varphi = \varphi_0 \sin(2\pi ft) \quad (56)$$

at the top surface of the electrode AB and an electrical ground (12) at the right boundary of the electrolyte EG , which is the midline of the cell repeat unit. The latter condition assumes that the cell is symmetrical about this midline. It should also be noted that (56) differs from the condition (11) used in Sections 2.2 and 2.3 in that the applied potential is no longer complex; the PNP model formulation used here is too complicated to explicitly consider complex potential and current. Instead, the complex impedance will be extracted via Fourier transform. All other boundaries are considered to be electrically insulating according to (13).

The complete model formulation consists of the governing equations (47), (48), (49), and (55), subject to the boundary conditions (12), (13), (50), (51), (52), and (56). At $t = 0$, a vacancy concentration of c_{V0} is assigned to the electrolyte, the two-phase region CD , and the three-phase region D . The initial electron concentration is specified as c_{e0} in the electrode bulk, electrode surface region ABD , two-phase region, and three-phase region. The initial concentration of adsorbed oxygen is c_{O0} in the electrode surface and two-phase regions. All other initial concentrations are zero, as is the initial electrical potential.

2.4.2 Impedance

The output generated by the model consists of the concentrations and fluxes of oxygen vacancies, electrons, and adsorbed oxygen, as well as the potential, as a function of time and space. In order to calculate impedance, the total current as a function of time must be determined. The current density due to transport of charged species is given by

$$J_F = F \sum_i z_i \Phi_i \quad (57)$$

The model considers two mobile charged species, vacancies and electrons. Therefore the total faradaic current density is given by

$$J_F = F(2\Phi_V - \Phi_e) \quad (58)$$

Non-faradaic current due to electrical displacement can also occur and is given by

$$J_D = -\varepsilon\varepsilon_0 \frac{\partial\varphi}{\partial t} \quad (59)$$

The total current density is then given by

$$J_{tot} = J_F + J_D \quad (60)$$

The total current is determined by integrating J_{tot} along an equipotential contour S :

$$I = \int_S \hat{n} \cdot J_{tot} ds \quad (61)$$

For convenience, the integration is carried out along the symmetry boundary EG where $\varphi = 0$ is enforced by the electrical ground boundary condition. This results in a time-dependent current signal $I(t)$ which can be used to determine impedance.

The impedance is calculated using a custom MATLAB script employing the Fast Fourier Transform (FFT) algorithm to transform the potential and current signals $\varphi(t)$ and $I(t)$ into frequency space:

$$Z(f) = \frac{\text{fft}[\varphi(t)]}{\text{fft}[I(t)]} \quad (62)$$

The code for the MATLAB script is presented in Appendix A. While (62) computes the impedance across a range of frequencies, most of the Z values are spurious since the input signals $\varphi(t)$ and $I(t)$ have only one frequency of oscillation. Therefore only the impedance value corresponding to the input frequency is kept. The complete impedance spectrum is generated by repeating the modeling procedure over a range of frequencies.

2.4.3 Mesh

The model used a triangular mesh with 11,317 elements. In order to balance accuracy with computational time, the mesh was refined in the interfacial layers and triple phase region, where large concentration gradients are expected to occur. In the bulk electrode and electrolyte regions, where concentration gradients are expected to be small, relatively large mesh elements were used. The mesh was specified to have 125 elements along each of the boundaries AB and CD, and 30 elements along each side of the triple phase region. A mesh convergence study was performed by adjusting each mesh size parameter; the maximum numerical error using the specified mesh was determined to be approximately 0.5%.

2.4.4 Parameter Values

The majority of the parameter values used in the model were estimated from the literature. These fixed parameters are summarized in Table 2. The concentration c_{SO} of oxygen sites in the YSZ electrolyte was calculated from the molar volume of ZrO_2 . The equilibrium concentration $c_{VO,0}$ of oxygen vacancies in the electrolyte was calculated based on an 8 mol% yttria doping level. The electrolyte conductivity at

500°C was estimated from a published average of several reported values for bulk YSZ.¹¹³ (It should be noted that published values for YSZ thin films, unlike bulk YSZ, vary widely.) The diffusivity of vacancies in the electrolyte, D_{VO} , was then calculated based on the equilibrium concentration and conductivity. The equilibrium concentration $c_{e,0}$ of electrons in the electrode was estimated based on the molar volume of platinum, assuming one free electron per atom. The electron diffusivity in platinum, D_e , was then calculated from published electrical conductivity values.¹¹⁴ The concentration c_{Sad} of adsorption sites on the electrode was obtained based on a surface concentration of 1.5×10^{19} per square meter. This was converted to a volume concentration by dividing by the thickness of the active surface layer, h_{act} . The equilibrium oxygen coverage on the electrode was taken as approximately 0.35 monolayer based on published theoretical calculations around 700 K.¹¹⁵ This was converted to a volume concentration $c_{Oad,0}$ in mol/m^3 . The diffusivity of adsorbed oxygen on the electrode surface, D_{Oad} , was estimated from the literature.¹¹⁶

Table 3. Model parameters

Symbol	Description	Value
T	Temperature	773 K
P_{O_2}	Oxygen partial pressure	0.21 atm
φ_0	Applied potential	1 mV
D_V	Vacancy diffusivity	$1 \times 10^{-12} \text{ m}^2/\text{s}$
D_e	Electron diffusivity	$1 \times 10^{-4} \text{ m}^2/\text{s}$
D_O	Adsorbed oxygen diffusivity	$1 \times 10^{-12} \text{ m}^2/\text{s}$
c_{SO}	Electrolyte oxygen site concentration	92200 mol/m^3
c_{Sad}	Electrode adsorption site concentration	25100 mol/m^3
c_{V0}	Initial vacancy concentration	7376 mol/m^3
c_{e0}	Initial electron concentration	75000 mol/m^3

c_{00}	Initial adsorbed oxygen concentration	8785 mol/m ³
ε	Electrolyte permittivity	25

Chapter 3

RESULTS

3.1 Grain Boundary Heterogeneity Study

The first phase of the study was performed using the 2D impedance model described in Section 2.2 to investigate the role of heterogeneity in electrolyte grain boundaries. The model allows the impedance of polycrystalline electrolytes with arbitrary grain boundary properties to be simulated. That is, the conductivity and permittivity of each grain boundary can be specified individually given a desired random distribution. These simulated impedance spectra were then fitted using equivalent circuits to study the efficacy of the circuit fitting procedure.

3.1.1 Sample Results

Current and potential distributions for a sample polycrystal with distributed grain boundary conductivity and homogeneous permittivity are shown in Figure 18. The values of $\log(\sigma_{gb})$ were normally distributed with a standard deviation of 1; the range of conductivities therefore spanned approximately six orders of magnitude from 10^{-10} S/m to 10^{-4} S/m. The σ_{gb} value for each grain boundary is indicated by the black and white color scale in part (a). The current and potential distributions in the polycrystal at three different frequencies are shown in parts (a) and (b) of the figure, respectively. At low frequency the most resistive grain boundaries exhibit a strong blocking effect, with significant detouring of current through neighboring boundaries and large potential gradients. Depending on the orientation of these highly blocking

boundaries (since a boundary parallel to the overall current direction will have less of an influence than one perpendicular to the current direction), the total observed grain boundary resistance can be markedly higher than in the homogeneous case. The randomly assigned distribution and placement of grain boundary conductivities thus introduces considerable scatter in the total sample grain boundary resistance between repeated trials for a given standard deviation, especially as the grain size begins to approach the overall sample size. At higher frequency, the grain boundaries are increasingly dielectrically conductive and have less influence on the current path across the electrolyte.

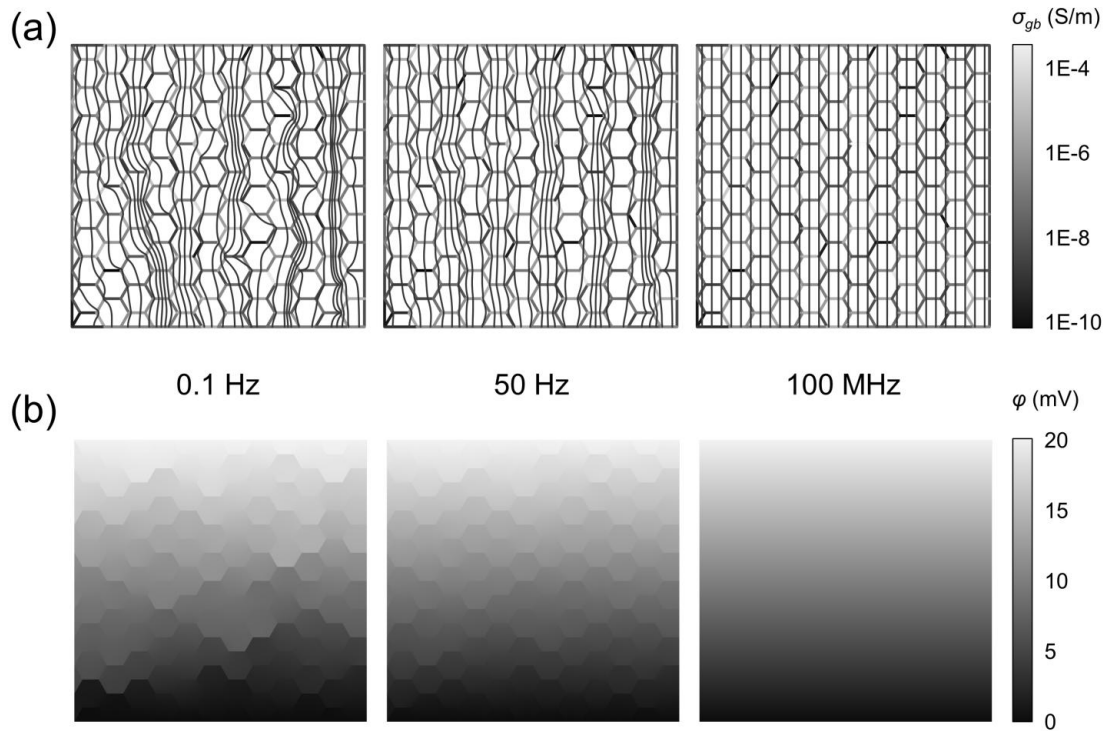


Figure 18. (a) Current lines and (b) distributions of electrical potential in a specimen with heterogeneous grain boundary conductivity and homogeneous permittivity. The conductivity of each grain boundary in the sample is indicated in part (a) according to the scale shown on the right. Results are shown for three different frequencies.

Figure 19 shows the impedance spectrum and CPE equivalent circuit fit obtained for the sample shown in Figure 18. For illustrative purposes, the impedance of this sample was calculated at more than 13 frequencies. Two semicircular features are observed: a high frequency grain arc and a low frequency grain boundary arc. As can be seen from the figure, the equivalent circuit provided an excellent fit of the model data. The fit yields a CPE exponent of 1 for the high frequency (grain) arc, indicating a near-perfect semicircle. With $n_{grain} \approx 1$, Q_{grain} can be treated as a capacitance and the apparent grain permittivity can be calculated from the parallel

plate equation as $\epsilon_{grain} = 25.01$, an error of approximately 0.03%. Similarly, the apparent grain conductivity obtained from R_{grain} is 9.998×10^{-5} S/m, an error of approximately 0.02%. These results are as expected, since the grain properties were defined to be homogeneous. On the other hand, the CPE exponent corresponding to the grain boundary arc is 0.859, indicating substantially non-ideal behavior. The quantitative meanings of R_{gb} , Q_{gb} , and n_{gb} will be explored in subsequent sections.

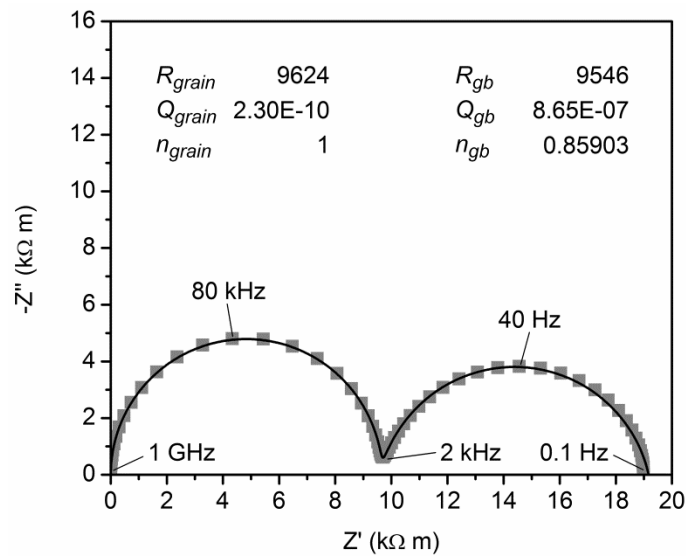


Figure 19. Representative impedance spectrum for a polycrystalline electrolyte with homogeneous grain boundary permittivity and heterogeneous grain boundary conductivity, along with the best fit parameters for the R-CPE equivalent circuit. The conductivity values follow a log-normal distribution with a standard deviation of 1. Frequencies of a few relevant data points are indicated.

3.1.2 Heterogeneous Conductivity

In order to further investigate the case of heterogeneous grain boundary conductivity, data were obtained over a range of values of the population standard

deviation of $\log(\sigma_{gb})$. Multiple trials were conducted for each value. The relationship between the CPE exponent n_{gb} and the standard deviation of the conductivity values is shown in Figure 20. As may be intuitively expected, the exponent decreases below 1, signifying less ideal capacitive behavior at the grain boundaries, as the grain boundary conductivity becomes more heterogeneous. A reasonably linear relationship between the standard deviation and n_{gb} exists with no clear dependence on grain size, suggesting that the standard deviation of a normally distributed grain boundary conductivity could be quantified from the CPE equivalent circuit fit, at least in situations when all other grain boundary parameters are uniform.

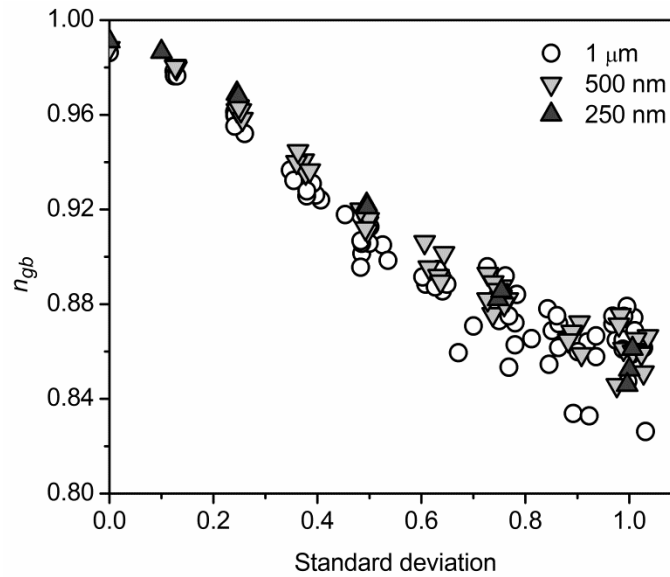


Figure 20. Equivalent circuit parameter n_{gb} as a function of standard deviation of $\log(\sigma_{gb})$ for specimens with heterogeneous grain boundary conductivity. Grain size is indicated by symbol.

Figure 21 shows the apparent grain boundary conductivity, calculated from R_{gb} using (20), as a function of the standard deviation of the grain boundary conductivity values. The figure shows increased scatter in the apparent conductivity as the standard deviation of the conductivity distribution is increased. This result is perhaps to be expected, but the range of apparent conductivity values remains surprising. A researcher presumably wishes to use the impedance measurement to determine the properties of the average grain boundary; however, Figure 21 shows that if the grain boundary conductivities are heterogeneous, the apparent conductivity obtained from the equivalent circuit can differ from the value for a homogeneous sample by up to 30%. The smaller grain sizes appear to show less scatter between trials, which is an intuitive result since current traversing a large number of grain boundaries would be expected to encounter more or less the same distribution of conductivities regardless of the path taken. Thus, the difference from sample to sample is reduced. In contrast, the spatial distribution of highly resistive boundaries can be more variable when the total number of boundaries is small, resulting in larger differences between samples. It is also apparent from the figure that (20) is more likely to provide an underestimate of the mean conductivity for 1 μm grains than for the smaller grain sizes. This is likely because with a smaller total number of grains, the conductivity estimate can be strongly influenced by a small number of highly resistive grain boundaries.

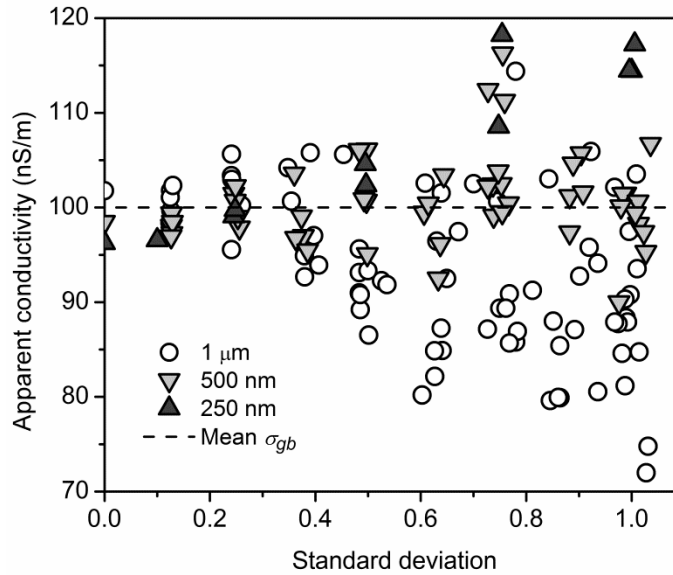


Figure 21. Apparent grain boundary conductivity of specimens with heterogeneous grain boundary conductivity, calculated from the equivalent circuit parameter R_{gb} using (20), vs. standard deviation of $\log(\sigma_{gb})$. The mean grain boundary conductivity is indicated by a dashed line.

The apparent relative permittivity of the grain boundaries was calculated from the equivalent circuit parameters using (22). Since a capacitance C_{gb} is not given by the R-CPE equivalent circuit, this initial permittivity calculation was made using the simplifying assumption $C_{gb} = Q_{gb}$ (that is, the non-ideal nature of the CPE was ignored, as is often the case in experimental studies). More advanced methods for estimating C_{gb} are discussed later in the text. The apparent permittivity calculated using the above method is shown as a function of the standard deviation of the conductivity distribution in Figure 22. The actual relative permittivity of each grain boundary, $\epsilon_{gb} = 25$, is indicated by the dashed line (as stated above, permittivity was homogeneous for these samples). As can be seen from the figure, when the conductivity distribution is narrow Q_{gb} can be used to obtain an excellent estimate of

ε_{gb} . However, the calculated value of ε_{gb} quickly becomes unsatisfactory as the standard deviation of the conductivity distribution is increased. For a standard deviation of 1, the apparent relative permittivity of the grain boundaries was between 2.8 and 4.6 times the actual value. As with the apparent conductivity, the scatter in the apparent permittivity decreased with decreasing grain size.

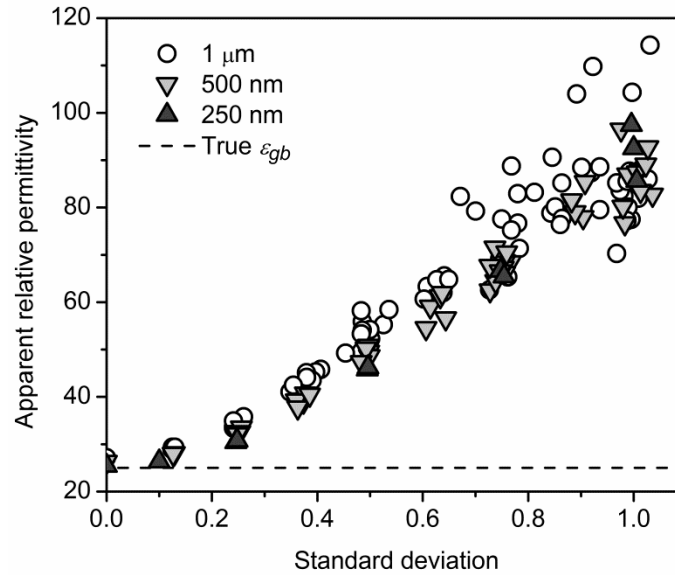


Figure 22. Apparent grain boundary permittivity of specimens with heterogeneous grain boundary conductivity, calculated from the equivalent circuit parameter Q_{gb} using (22), plotted as a function of the standard deviation of $\log(\sigma_{gb})$. The actual (homogeneous) value of ε_{gb} is indicated with a dashed line.

3.1.3 Heterogeneous Permittivity

The second set of simulations considered the case where the grain boundary permittivity, but not the conductivity, was defined to be heterogeneous. Since the distribution of permittivity values was not Gaussian, the standard deviation of the

distribution was not intuitively meaningful. Therefore the quantity $\varepsilon_{ideal} - \varepsilon_{mean}$ (where $\varepsilon_{ideal} = 25$) was chosen instead as a comparable metric of the spread of the distribution. The value of this quantity ranges from zero (all $\varepsilon_{gb} = 25$) to 12 (ε_{gb} uniformly distributed between 1 and 25). Results for a number of different permittivity distributions are shown in the following figures. The value of the CPE exponent n_{gb} as a function of the spread of the permittivity distribution is shown in Figure 23. Again, it is observed that the CPE exponent decreases monotonically as the spread of the permittivity distribution increases. The trend is slightly more pronounced for larger grain sizes. The CPE exponent reached a minimum of approximately 0.88 for the most non-ideal cases considered, in which the permittivity distribution was nearly uniform.

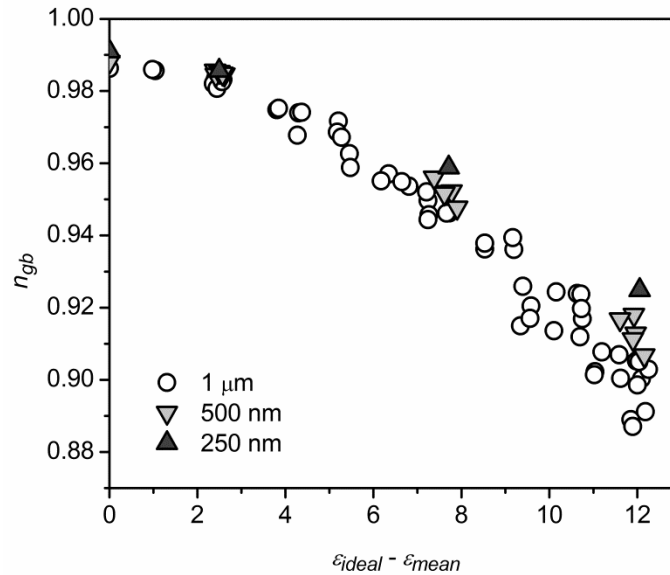


Figure 23. Equivalent circuit parameter n_{gb} as a function of $\varepsilon_{ideal} - \varepsilon_{mean}$, a measure of the spread of ε_{gb} , for specimens with heterogeneous grain boundary permittivity. Results are shown for three different grain sizes, indicated by symbol.

Figure 24 shows the apparent grain boundary conductivity calculated from the equivalent circuit parameter R_{gb} as a function of the permittivity distribution spread. The apparent conductivity decreases slightly with increasing spread of the permittivity distribution, but shows less than 4% deviation from the homogeneous case even for a near-uniform distribution. The figure also shows a noticeable difference in apparent conductivity between different grain sizes, though the overall deviation from the ideal case is less than 7% for all specimens, and may be largely or partly due to numerical error.

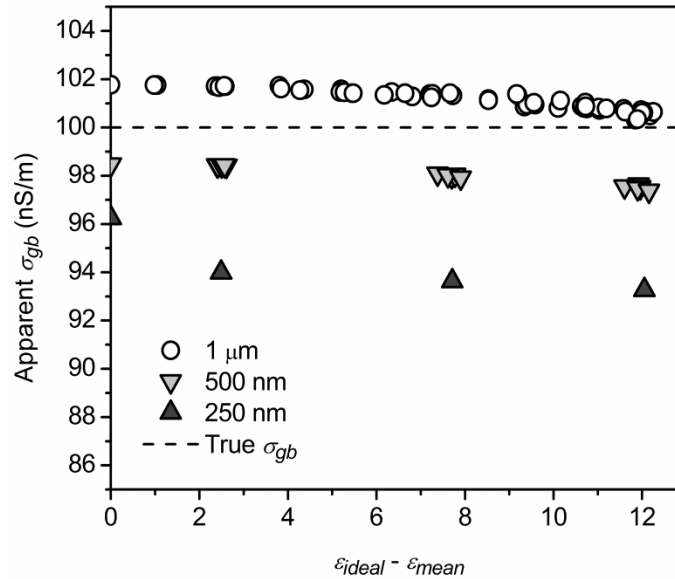


Figure 24. Apparent grain boundary conductivity of specimens with heterogeneous grain boundary permittivity, calculated from the equivalent circuit parameter R_{gb} using (20), vs. $\epsilon_{ideal} - \epsilon_{mean}$, a measure of the spread of ϵ_{gb} . The actual (homogeneous) grain boundary conductivity is indicated by a dashed line.

The corresponding results for the apparent permittivity are shown in Figure 25. Due to the choice of an exponential probability density function to describe the permittivity distribution, the mean grain boundary permittivity (indicated by a dashed line in the figure) changed according to the values of the distribution parameters. As seen in the figure, the equivalent circuit parameter Q_{gb} can be used to obtain an excellent estimate of the mean permittivity value when the distribution of permittivity values is very narrow. This result is as expected, since the CPE exponent n_{gb} is close to 1 in such cases and thus the CPE represents a nearly ideal capacitor. However, the apparent value of Q_{gb} diverges rapidly from the mean as the distribution spread is increased. In the case of a nearly uniform distribution of ε_{gb} values, the permittivity value determined from the equivalent circuit could be nearly double the actual mean value. Interestingly, Q_{gb} , and thus the apparent permittivity, changes relatively little as the distribution of permittivity values increases. This result may be related to the choice of distribution function: even when the spread of the distribution increased, the maximum permittivity value remained 25. Thus, Q_{gb} may be directly useful in providing a reasonable estimate of the maximum, rather than mean, grain boundary permittivity in these cases.

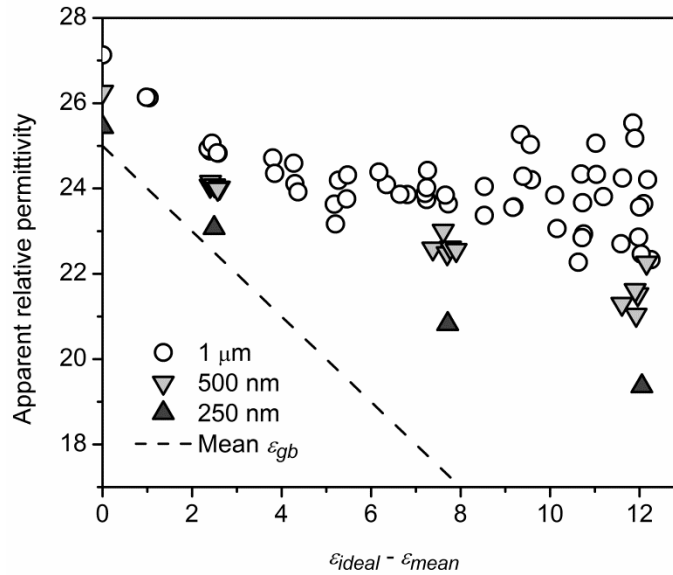


Figure 25. Apparent grain boundary permittivity of specimens with heterogeneous grain boundary permittivity, calculated from the equivalent circuit parameter Q_{gb} using (22), vs. $\epsilon_{ideal} - \epsilon_{mean}$, a measure of the spread of ϵ_{gb} . The mean grain boundary permittivity is indicated by a dashed line.

3.1.4 Heterogeneous Conductivity and Permittivity

The foregoing results suggest that the value of the CPE exponent n_{gb} could be used to provide a quantitative estimate of the spread of either the conductivities or permittivities of the grain boundaries if only one or the other is heterogeneous. However, the picture becomes more complicated when both conductivity *and* permittivity are allowed to vary. Figure 26 shows sample impedance spectra for four related cases: (a) heterogeneous grain boundary conductivity, (b) heterogeneous grain boundary permittivity, (c) heterogeneous conductivity *and* permittivity, and (d) the homogeneous case where both parameters are uniformly defined. The conductivity distribution used in cases (a) and (c) had a standard deviation of 1, while the permittivity distribution used in cases (b) and (c) was nearly uniform with $\epsilon_{mean} \approx 12.6$. The grain size was 1 μm in all cases. As the grain impedance is the same in each case,

the majority of the high frequency impedance arc has been excluded from view. As seen in the figure, the combined distributions of conductivity and permittivity result in an accumulative effect on the CPE exponent n_{gb} . Equivalent circuit fitting yielded $n_{gb} = 0.78$ for case (c), significantly less than for either case (a) or case (b). Thus the combined effect of heterogeneous grain boundary conductivity and permittivity (and likely other parameters including grain size) complicates the effort to quantify the spread of these property distributions from equivalent circuit fitting alone. Still, the mean parameter values remain quantifiable. This will be discussed further in Section 4.1.

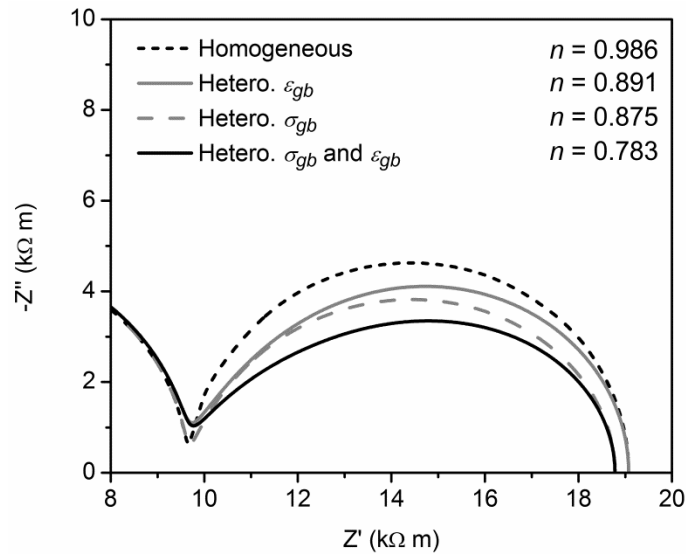


Figure 26. Grain boundary impedance arcs for four related cases: homogeneous σ_{gb} and ϵ_{gb} , heterogeneous ϵ_{gb} , heterogeneous σ_{gb} , and heterogeneous σ_{gb} and ϵ_{gb} . The CPE exponent n_{gb} obtained from equivalent circuit fitting in each case is indicated.

3.2 Phenomenological Electrode Modeling Study

The second portion of the present work shifted the focus of the modeling from the electrolyte to the electrode by including a phenomenological description of the interfacial electrochemistry, as detailed in Section 2.3. Since grain boundaries were not of interest to this study, the electrolyte was treated as a single crystal. However, it would be a straightforward matter to incorporate a treatment of the grain boundaries into the present model as well.

3.2.1 Sample Results

As an example of the model output, a simulated impedance spectrum for a 25 nm thick electrolyte is shown in Figure 27. As the parameter values used in this illustrative simulation were selected arbitrarily, the model output is not expected to quantitatively match the experimental data in Figure 11 (quantitative fitting of the experimental results will be discussed in Section 4.2.1). Still, the qualitative similarity is striking. Three separate impedance features can be distinguished, including a depressed partial arc in the intermediate frequency region.

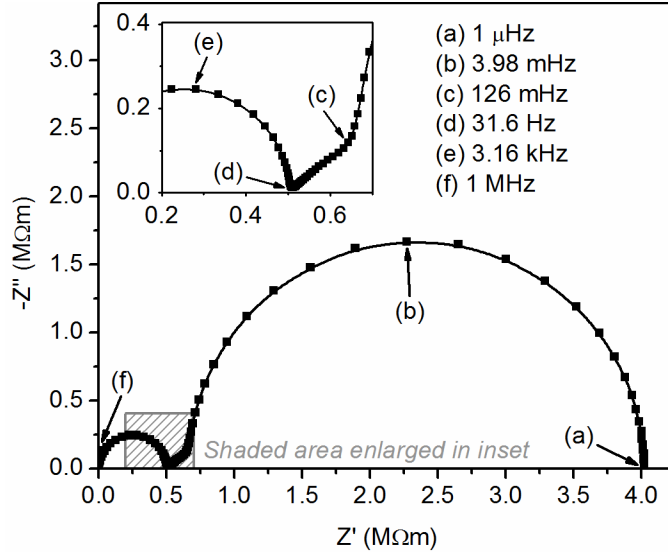


Figure 27. Impedance response predicted by the model for a 25 nm film at 700°C with $L_{ode} = L_s = 12.5 \mu\text{m}$, $\sigma = 10^{-5} \text{ S/cm}$, $J_0 = 10^{-4} \text{ mA/cm}^2$, $C_{DL} = 100 \mu\text{F/cm}^2$, and $\varepsilon = 10$. The intermediate frequency region is enlarged in the inset. The frequencies of a few key points are indicated.

In order to clarify the origin of the intermediate frequency arc, the current and potential distributions in the relevant frequency range were examined. Figure 28 shows the distributions at $f = 0.126 \text{ Hz}$ and 31.6 Hz , corresponding to the low- and high-frequency endpoints, respectively, of the intermediate frequency arc. The figure reveals that at 0.126 Hz or below, nearly all of the potential drop in the specimen occurs at the electrode-electrolyte interface, and the current distribution along the length of this interface is nearly uniform. At 31.6 Hz or higher, the potential drop across the interface is small compared to that in the electrolyte. At these relatively high frequencies, current is no longer distributed over the entire interface and instead travels through a narrower region near the edge of the electrode.

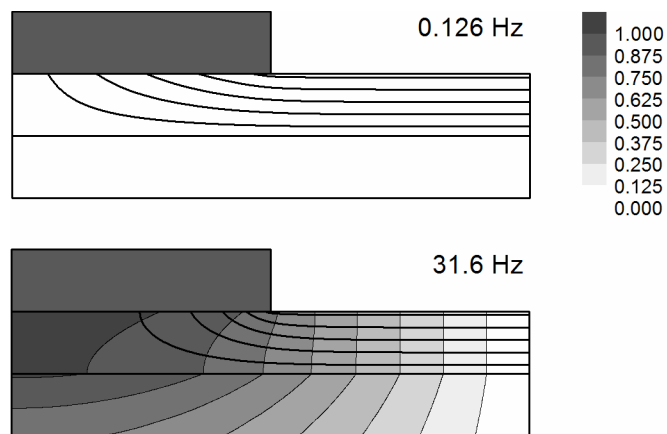


Figure 28. Contours of electrical potential in mV, indicated by black and white color scale, in the electrode, electrolyte, and substrate at $f = 0.126$ Hz and 31.6 Hz. The vertical dimension has been exaggerated and the substrate truncated to aid visualization. The distribution of current in the electrolyte is also shown via solid lines.

This frequency-dependent change of current path through the electrolyte is due to low-impedance dielectric current flux across the electrode-electrolyte interface. At relatively low frequencies, the impedance of the interface is large compared to that of the electrolyte and current travels further on average through the electrolyte to spread out over the entire interface. At higher frequencies, the interfacial impedance begins to vanish due to non-negligible double-layer displacement current, and current is able to travel a shorter path that bypasses a large portion of the electrolyte. Thus the intermediate frequency impedance arc is associated with a kind of spreading resistance arising from the sample geometry and relative impedances of the electrolyte and the electrolyte-electrode interface. Specifically, it is related to the portion of the electrolyte which is covered by the electrode finger.

3.2.2 Parametric Studies

The intermediate frequency arc was further quantified via parametric study to determine when and why it forms a significant part of the overall measured impedance of the sample, and whether it can be of use in characterizing material properties of the electrode or electrolyte. The parameters of interest were the electrolyte thickness h , the electrolyte length L_{yte} , the electrode finger width L_{ode} , the electrolyte conductivity σ , and the exchange current density J_0 .

The effect of varying the electrolyte thickness is demonstrated in Figure 29, which shows impedance spectra for four otherwise identical samples with different film thicknesses. As the high frequency impedance arc was not of interest here, it was cropped out of the figure and the real axis was re-zeroed at the high frequency extreme of the intermediate arc in order to enable direct quantitative comparison between the different cases. The magnitude of the intermediate frequency arc decreases with increasing thickness, which explains why this arc has only been reported for measurements on samples with nanoscale thickness; for $h = 25$ nm the intermediate arc is barely evident, whereas for $h = 1$ nm its magnitude is similar to that of the electrode arc. In addition, the apparent magnitude of the low frequency (electrode) arc *also* increases visibly for smaller values of h . This indicates that equivalent circuit fitting could yield inaccurate values of the electrode parameters in this case, an important finding that is discussed further in Sec. 3.4. Note that the assumption of continuum physics is likely not completely valid at $h = 1$ nm, but the results are included here for demonstration purposes.

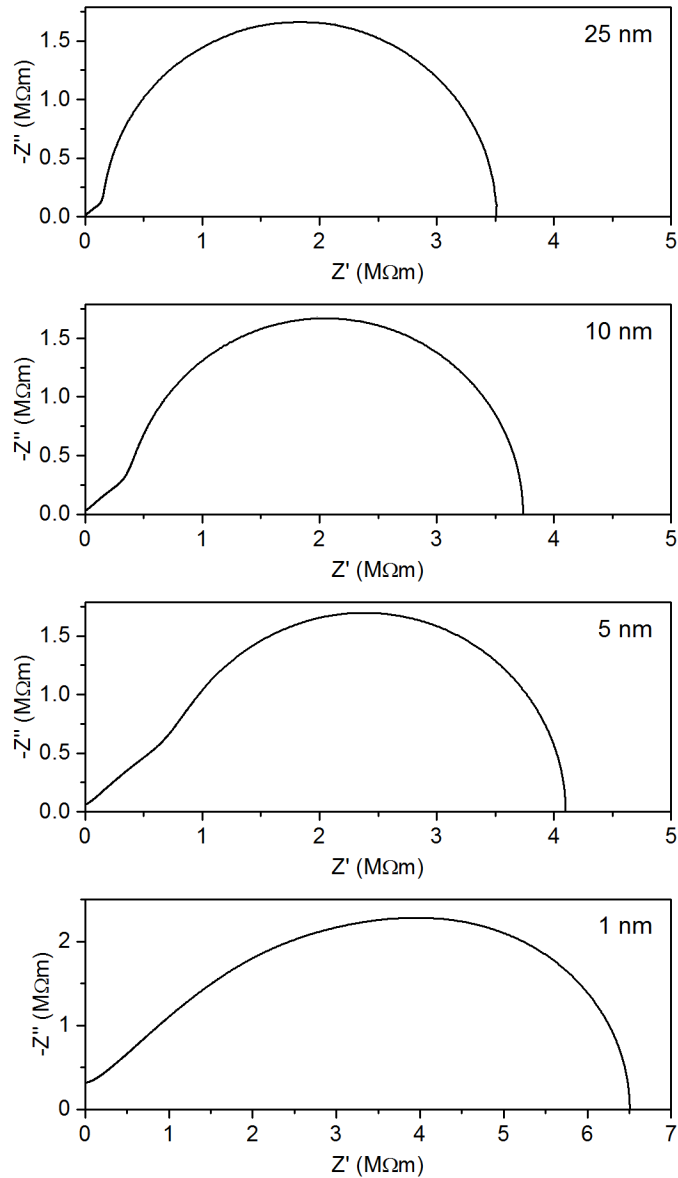


Figure 29. Low and intermediate frequency portions of the impedance spectra for specimens with the indicated electrolyte thickness and $L_{ode} = L_s = 12.5 \mu m$. The figure has been cropped and re-zeroed on the real axis in order to ignore the high frequency impedance arc. Note change of scale for the 1 nm specimen.

In order to better compare these results, quasi-DC resistances were deconvoluted for the electrode, the electrolyte, and the intermediate frequency arc. The quasi-DC electrolyte resistance R_{yte} was obtained from the model by calculating the total impedance at very low frequency ($f = 10^{-12}$ Hz) with J_0 sufficiently large to render the electrode contribution negligible ($J_0 = 10^6$ mA/cm²). The values so obtained agree closely with the theoretical electrolyte resistance,¹¹⁷ given by

$$R_{yte,theo} = \frac{L_{yte} - L_{ode}}{hw\sigma} + R_{spread} \quad (63)$$

where w is the out-of-plane specimen width, taken as unity in the present work. The first term in (63) is simply the bulk resistance of the exposed portion of the electrolyte film (region $BCDE$ in Figure 13), while R_{spread} is the additional resistance incurred between plane BE and the electrode. When $L_{ode} / h > 2$, which is the case for most thin films, R_{spread} can be approximated¹¹⁷ as

$$R_{spread} = \frac{\ln 2}{\pi w \sigma} \approx \frac{0.221}{w \sigma} \quad (64)$$

In most cases, R_{spread} is negligible compared to the bulk resistance. (It should be noted that the first term of (63) differs from the expression given in Reference 117 by a factor of 2 owing to the choice of geometric repeat unit.)

In a manner analogous to the procedure above, the quasi-DC resistance of the electrode, R_{ode} , was obtained from the model by calculating the total impedance at very low frequency ($f = 10^{-12}$ Hz) with σ sufficiently large that the impedance contribution of the electrolyte was negligible ($\sigma = 10^4$ S/m). As expected, the value of R_{ode} so calculated agrees closely with the theoretical electrode resistance

$$R_{ode,theo} = \frac{1}{L_{ode} w} \cdot \frac{RT}{J_0 zF} \quad (65)$$

Finally, the effective resistance of the intermediate frequency arc, R_2 , was quantified by subtracting R_{yte} and R_{ode} from the total quasi-DC resistance:

$$R_2 = R_{total} - R_{yte} - R_{ode} \quad (66)$$

By inspection, the values derived using the above procedure for R_2 , R_{yte} , and R_{ode} corresponded well to the approximate diameters of the (overlapping) arcs seen in the impedance spectra calculated for each model. The values of R_2 , R_{yte} , and R_{ode} were compiled for a range of model geometries for further analysis.

The relationship between R_2 and the electrolyte aspect ratio L_{yte} / h is shown in Figure 30. A linear trend corresponding to the semi-empirical equation

$$R_2 = \frac{L_{ode}}{3\sigma h} \quad (67)$$

is apparent for small values of L_{yte} / h (i.e., where the electrolyte is thick relative to the electrode spacing), but as the ratio is increased a deviation from linearity is observed. The onset of this deviation occurs at a lower value of L_{yte} / h for a larger electrolyte thickness, with a linear relationship observed only when $R_{ode} \gg R_{yte}$. Based on this observation, (63) and (65) can be combined (assuming negligible high frequency spreading resistance) to derive a condition for linearity. This yields

$$\frac{h}{L_{ode}(L_{yte} - L_{ode})} \frac{\sigma RT}{J_0 n F} \gg 1 \quad (68)$$

For a given value of L_{yte} , the product $(L_{yte} - L_{ode})L_{ode}$ is maximized when the electrode finger width and spacing are equal; i.e. $L_{ode} = 0.5L_{yte}$. Keeping in mind that a lower bound on the quantity on the left-hand side of (68) is being sought, the inequality can then be rewritten as

$$\frac{h\sigma RT}{L_{ode}^2 J_0 nF} \gg 1 \quad (69)$$

which establishes the range of electrolyte aspect ratios for which R_2 vs. L_{yte} / h is linear. The dimensionless quantity on the left-hand side of (69) will be denoted S for future reference.

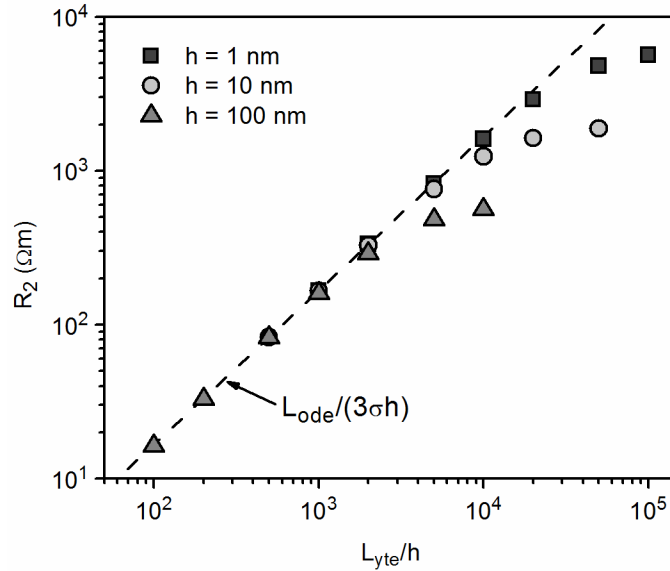


Figure 30. Resistance R_2 vs. L_{yte} / h for various values of h , with $\sigma = 10^{-3}$ S/m and $J_0 = 10^{-4}$ mA/cm². The electrode finger width and spacing are equal. The dashed line is a plot of the semi-empirical expression indicated.

The magnitude of the intermediate frequency impedance arc also depends on the electrode finger width and spacing. Impedance spectra for a few representative values of the coverage ratio L_{ode} / L_{yte} are shown in Figure 31. The ratio varies from a limiting case of 0 as the electrode finger width approaches zero to 1 as the finger spacing approaches zero. A coverage ratio of 0.5 indicates that the finger width and spacing are equal. As can be observed from the figure, the intermediate frequency arc

increases in magnitude and the high frequency arc decreases in magnitude as the electrode coverage increases. This result strongly supports the hypothesis that the two arcs arise from processes related to the covered and uncovered portions of the electrolyte, respectively.

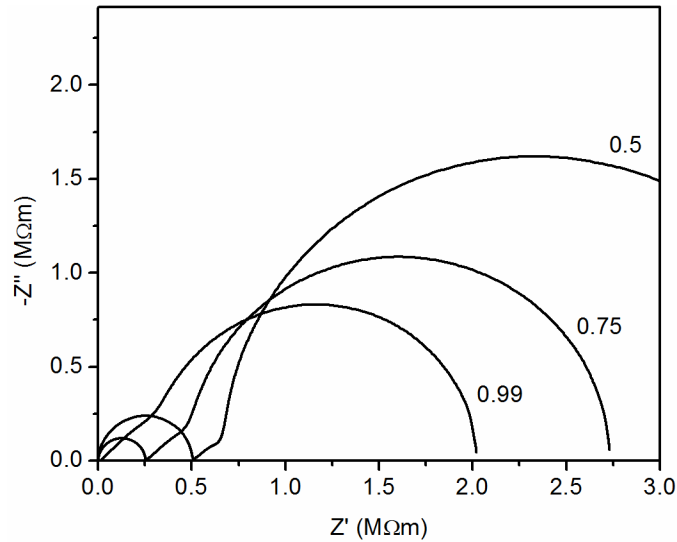


Figure 31. Impedance spectra for the three indicated values of L_{ode} / L_{yte} (i.e., the ratio of the electrolyte surface that is covered by the electrode).

Figure 32 shows the resistance R_2 as a function of L_{ode} / L_{yte} for three different electrolyte aspect ratios. In order to confirm that the absolute size is not important, results are shown for two sets of specimens, one with $L_{yte} = 25 \mu\text{m}$ and one with $L_{yte} = 10 \mu\text{m}$. As before, the results for R_2 match closely with (67) when (69) is satisfied. There is also no observable difference between the large and small samples, again provided (69) is satisfied.

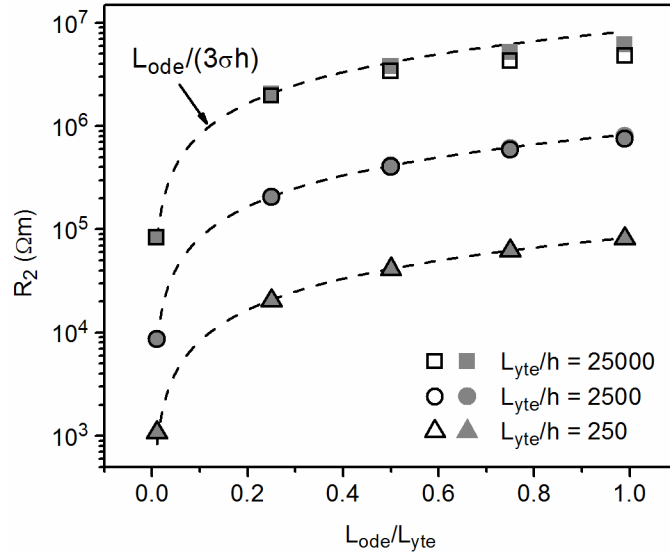


Figure 32. Resistance R_2 vs. L_{ode} / L_{yte} for three different electrolyte aspect ratios, with $L_{yte} = 10 \mu m$ (filled symbols) and $25 \mu m$ (open symbols). The semi-empirical linear expression shown is also plotted for each electrolyte aspect ratio as indicated via dashed line.

The effects of varying the exchange current density J_0 and the electrolyte conductivity σ were also studied. Impedance spectra corresponding to several different values of J_0 are shown in Figure 33. For small values of J_0 , there is no discernible change in the intermediate frequency arc with exchange current density. However, the intermediate frequency arc begins to vanish along with the low frequency arc as J_0 is increased, indicating that electrode processes do play a role in the intermediate frequency effect.

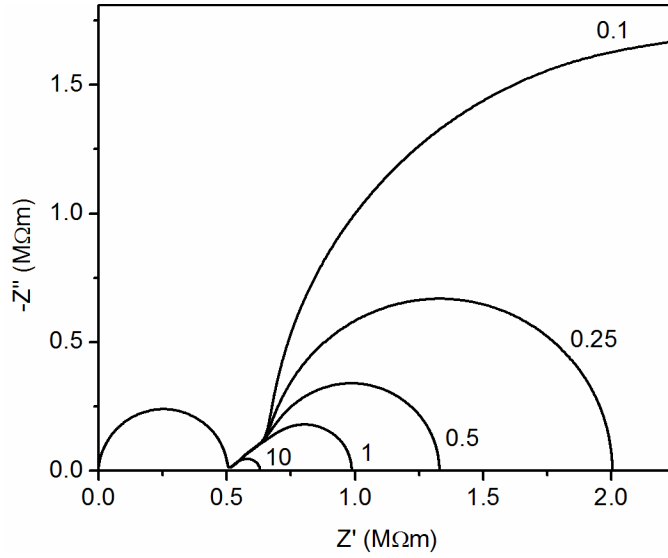


Figure 33. Impedance spectra for specimens with the indicated values of exchange current density in $\mu\text{A}/\text{cm}^2$.

Plots of R_2 as a function of J_0 are shown in Figure 34 for a few different values of the electrolyte conductivity σ . The figure confirms the behavior seen in Figure 33; the value of R_2 is independent of J_0 for small values of J_0 but decreases for larger values of J_0 . This result is as expected from the previously determined condition (69), which is not satisfied for large values of J_0 . Indeed, Figure 34 shows that R_2 continues to match closely with the semi-empirical expression (67) when (69) is satisfied, as indicated by the shaded region of the figure.

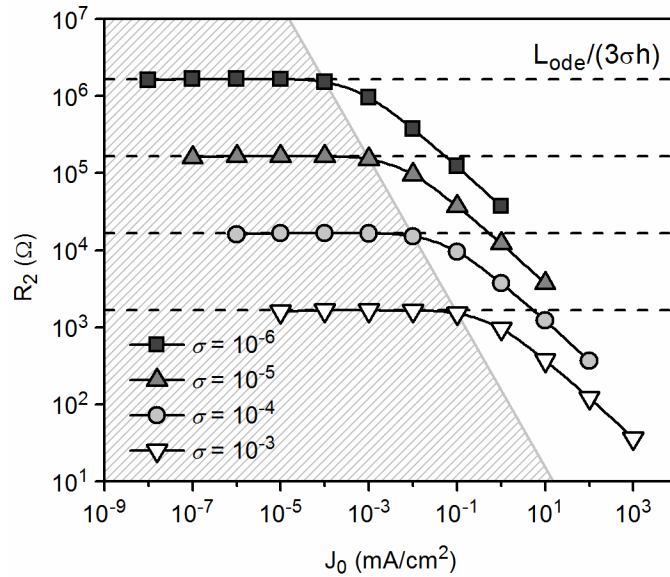


Figure 34. Value of R_2 as a function of exchange current density J_0 for various values of electrolyte conductivity in S/cm. The specimen dimensions are $L_{ode} = 12.5 \mu\text{m}$, $L_s = 12.5 \mu\text{m}$, and $h = 25 \text{ nm}$. The linear expression for R_2 shown in the upper right is plotted for each value of σ , indicated via dashed line. The condition $R_{ode} > R_{yte}$ is satisfied within the shaded region.

Based on the spacing of the curves in Figure 34, it appears that R_2 is inversely proportional to the electrolyte conductivity σ in the “ideal” regime where the dimensionless quantity $S \gg 1$. This is confirmed by re-plotting the results as a function of resistivity, shown in Figure 35. A linear relationship (67) between R_2 and $1/\sigma$ is observed when the relative magnitudes of J_0 and σ are such that $S \gg 1$. Although not evident in the figure, calculation of S at each data point confirmed that when (69) is not satisfied, a deviation from linearity is observed.

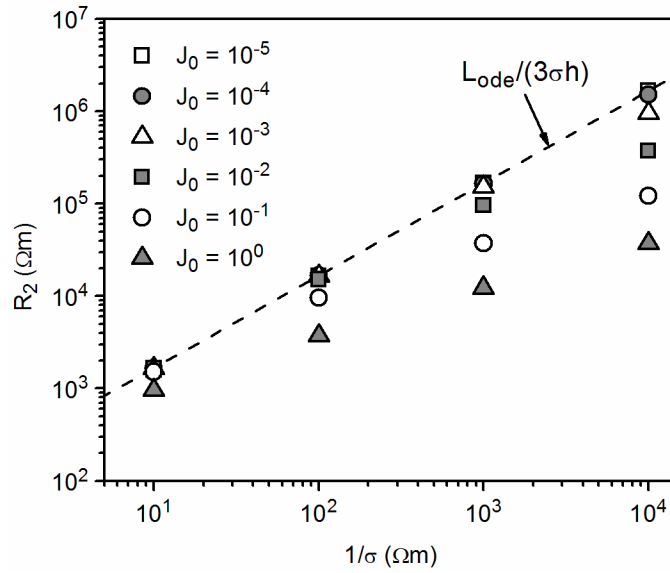


Figure 35. R_2 as a function of resistivity $1/\sigma$ for several different values of exchange current density in mA/cm^2 . The specimen dimensions are $L_{ode} = L_s = 12.5 \mu\text{m}$ and $h = 25 \text{ nm}$. The dashed line is a plot of the linear expression for R_2 indicated.

3.3 Diffusion-Reaction Electrode Modeling Study

Having studied some of the basic electrode effects using a simplified model, the electrode behavior can now be investigated in greater detail using the diffusion-reaction model described in Section 2.4. While the model is adaptable to a broad range of experimental conditions, the present work was limited to a single set of atmospheric parameters ($T = 500^\circ\text{C}$, $P_{O_2} = 0.21 \text{ atm}$) in order to manage the scope of the modeling task. Additionally, due to computational limitations, the model domain was restricted to approximately $50 \times 50 \text{ nm}$. As actual microelectrode finger widths are much larger, usually on the order of $1\text{--}100 \mu\text{m}$, the model could not be used to fit experimental data in the manner of the previous section. The extreme aspect ratio of the experimental specimens makes modeling this geometry computationally demanding, even if the model is nondimensionalized, and the results do not scale linearly with specimen size.

The present study was conducted on a desktop computer with 2 GB RAM, which was not sufficient to handle the full-scale electrode geometry with a reasonable computation time. However, the reduced-scale geometry is still sufficient to investigate the physical processes involved, and the results will be validated as much as possible. Future research using increased computing power will be required to apply the model to experimental data.

3.3.1 Sample Results

Before examining the model results in detail, it will be useful to present some sample results to demonstrate the various forms of output available from the model.

3.3.1.1 Impedance

An example impedance spectrum generated using the model is shown in Figure 36. Here, and in all subsequent sections unless otherwise noted, the electrolyte is 10 nm thick and 50 nm long, with equal electrode finger width and spacing (25 nm each). The thickness of the electrode surface and interfacial layers is 1 nm. In this example case the values of the reaction rate coefficients k_1^0 and k_2^0 have been chosen so that the electrode and electrolyte arcs will both be of sufficient magnitude to be readily visible in the figure. The spectrum exhibits a resistance of 791.7 Ωm at the low-frequency extreme (resistances are given in Ωm due to the two-dimensional model geometry). Two arcs are readily apparent: a low frequency arc with a resistance of 721.2 Ωm and a peak frequency of approximately 125 Hz, and a high frequency arc with a resistance of 70.4 Ωm and a peak frequency of approximately 30 MHz. The latter resistance differs by only 2% from the theoretical electrolyte resistance $R_{\text{yte,theo}} = 68.9 \Omega\text{m}$ calculated using (63), indicating that the high frequency arc corresponds to

the electrolyte as expected. (Note that due to the small overall dimensions of the electrolyte, the spreading resistance term in (63) is not negligible.) Therefore it is presumed that the remaining impedance is due to the electrode or electrode-electrolyte interactions.

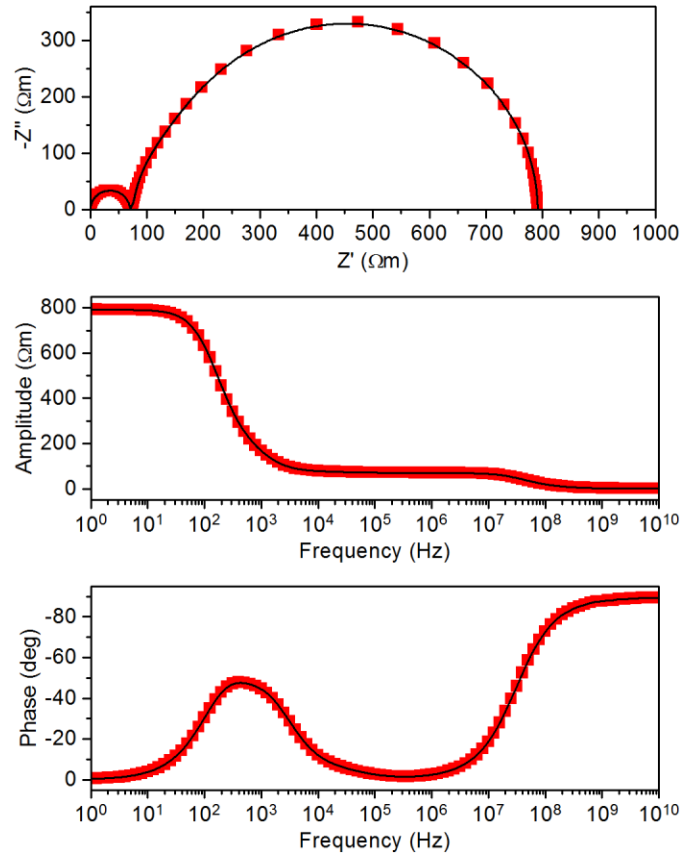


Figure 36. Simulated Nyquist and Bode impedance plots for a specimen with $k_{-1}^0 = 10 \text{ m}^3/\text{mol}\cdot\text{s}$, $k_2^0 = 4.1 \times 10^{-7} \text{ mol}\cdot\text{s}/(\text{kg}\cdot\text{m}^2)$, and $h_{act} = 1 \text{ nm}$.

3.3.1.2 IV Curve

Unlike other models which use linearized equations to model electrode reactions, the present model is not restricted to the linear regime and is able to

simulate behavior of the cell for arbitrarily large overpotentials (assuming the adsorption properties remain independent of adsorbate concentration). A simulated IV curve for the same cell modeled in Figure 36 is shown in Figure 37. The cell exhibits a cathodic limiting current of 161 mA/cm^2 and an anodic limiting current of 449 mA/cm^2 . These values are unrealistically large, indicating that the values of the reaction rate constants k_1^0 and k_2^0 , arbitrarily selected for illustrative purposes, are themselves unrealistic. Nevertheless the shape of the IV curve is qualitatively similar to published results for platinum on YSZ (cf. Fig. 11 in Reference 29), providing evidence that the model framework is valid. In the small overpotential range where the current-potential relationship is linear, the plot exhibits a slope of $791.9 \text{ } \Omega\text{m}$, which differs by only 0.03% from the quasi-DC resistance obtained from the impedance spectrum. Therefore the current-overpotential behavior of the model is quantitatively internally consistent with the AC impedance, as well as qualitatively consistent with published experimental data.

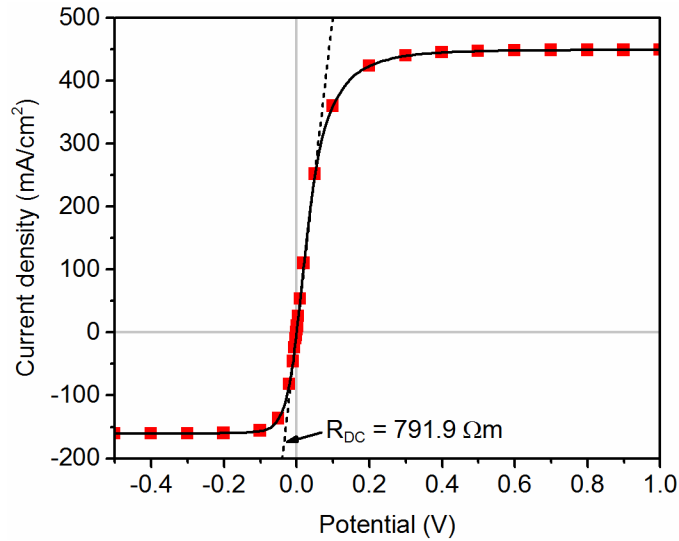


Figure 37. Simulated IV curve for a specimen with $k_{-1}^0 = 10 \text{ m}^3/\text{mol}\cdot\text{s}$, $k_2^0 = 4.1 \times 10^{-7} \text{ mol}\cdot\text{s}/(\text{kg}\cdot\text{m}^2)$, and $h_{act} = 1 \text{ nm}$. The electrode length is $L_{ode} = 25 \text{ nm}$.

3.3.1.3 Potential, Current, and Species Concentrations

The model output is of course not restricted to AC/DC measurements but also includes localized potentials, current, and concentrations. Figure 38 shows the potential distributions in the specimen considered in Figures 36–37 at two different frequencies, 0.01 Hz and 316 kHz, along with a representative current distribution in the electrolyte. These two frequencies correspond to the endpoints of the low frequency arc seen in Figure 36. At the lower frequency of 0.01 Hz, both the electrode and electrolyte contribute to the overall cell resistance with the majority of the total resistance coming from the electrode. Therefore, as can be seen in the figure, nearly all of the potential drop between the working electrode and the symmetry boundary occurs at the electrode-electrolyte interface. Additionally, current is concentrated at the triple phase boundary since this is the only region of the interface that current is able to traverse. Conversely, at the higher frequency of 316 kHz, displacement current

is able to completely short-circuit the interface and the electrode reaction no longer contributes to the total resistance. Thus the entirety of the potential drop occurs in the electrolyte and current is no longer concentrated in the vicinity of the triple phase boundary.

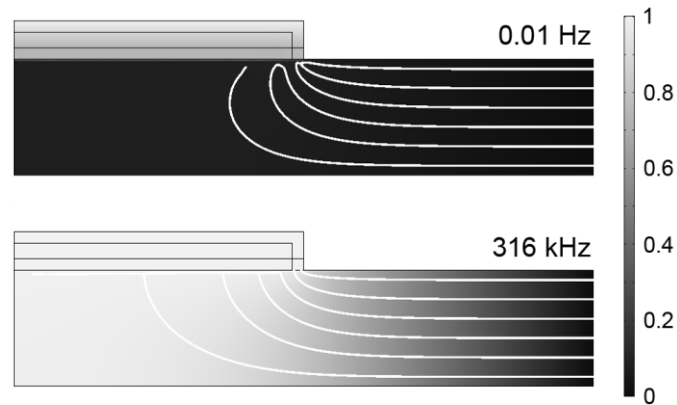


Figure 38. Potential distribution and representative current streamlines for the specimen modeled in Figure 36 at the frequencies indicated. The scale of the potential distribution is given in millivolts.

In Section 2.4.1 it was assumed that the diffusivity of adsorbed oxygen could be treated as independent of adsorbate concentration. Since the model output includes mobile species concentrations, it is now possible to test this assumption. The concentration of adsorbed oxygen was plotted along the L-shaped region *ABD* consisting of the surface layer and TPB as shown in Figure 39. Since the oxygen concentration is quite uniform across the thickness of this region, the plot has been simplified to a 1D plot along the centerline (indicated by the dashed line in the figure). The oxygen concentration along this line under a cathodic DC polarization is shown in

Figure 40 for several different adsorption rates. In the extreme of very fast adsorption ($k_2^0 = 0.41 \text{ mol}\cdot\text{s}/(\text{kg}\cdot\text{m}^2)$), the adsorption reaction is in equilibrium and the equilibrium concentration of oxygen is maintained throughout the surface layer. Any adsorbed oxygen consumed by the charge transfer reaction is replaced immediately from the atmosphere due to the very facile adsorption reaction. As the adsorption rate is decreased, adsorbed oxygen becomes increasingly depleted on the surface, with especially noticeable concentration gradients for $k_2^0 = 4.1\times 10^{-7}$ – $4.1\times 10^{-6} \text{ mol}\cdot\text{s}/(\text{kg}\cdot\text{m}^2)$. In the extreme of slow adsorption ($k_2^0 = 4.1\times 10^{-13} \text{ mol}\cdot\text{s}/(\text{kg}\cdot\text{m}^2)$), the concentration profile becomes uniform at a concentration lower than the equilibrium value. This lower limit of adsorbed oxygen concentration is determined by the charge transfer rate and applied potential. The behavior is similar for anodic polarization, but with oxygen concentrations *higher* than the equilibrium concentration in the case of slow adsorption. Regardless, for a polarization of $\pm 1 \text{ mV}$ (typical of an AC impedance experiment), the concentration of adsorbed oxygen in the surface layer never varies by more than 3.5% from the equilibrium value, so the assumption made in Section 2.4.1 that the diffusivity and adsorption rate constants can be treated as independent of oxygen concentration is clearly valid. Under higher polarization, such as in certain DC experiments, the depletion or excess of adsorbed oxygen on the electrode surface may be more extreme and the concentration dependence of oxygen diffusivity may no longer be negligible. Therefore caution should be exercised in applying the present model to DC polarization data without further study, but it is expected that the qualitative behavior of the model in such cases remains valid.

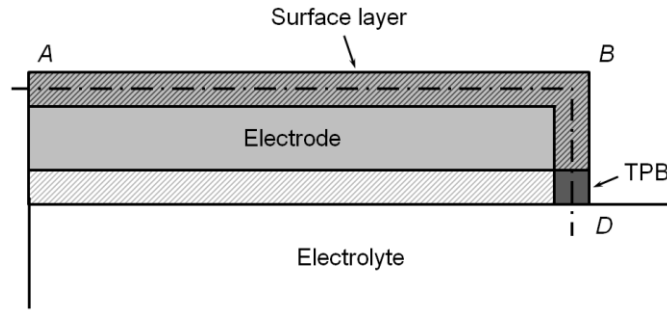


Figure 39. Centerline ABD through the surface layer and TPB, indicated by dashed line.

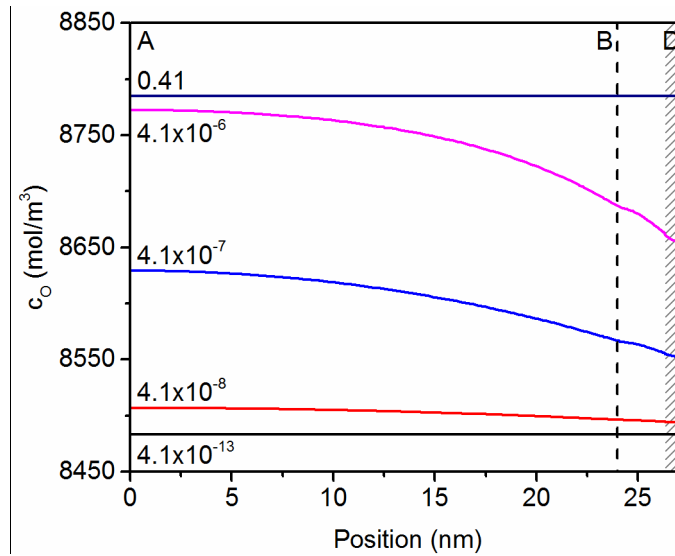


Figure 40. Concentration of adsorbed oxygen along the centerline ABD (shown in Figure 39) for the values of k_2^0 given in $\text{mol}\cdot\text{s}/(\text{kg}\cdot\text{m}^2)$ under cathodic DC polarization with $\eta = -1$ mV. The dashed line marks the bend at the electrode corner B , and the shaded area denotes the TPB.

3.3.2 Parametric Studies

Because of the unrealistically small sample geometry necessitated by the available computing resources, the present study does not include fitting of experimental data. However, the model in its limited form is still useful for

investigating the relative influence of key parameters on the overall impedance. Of particular interest is the interplay between the three processes that make up the overall electrode reaction: adsorption/desorption of oxygen on the electrode surface, diffusion of adsorbed oxygen, and the charge transfer reaction. By adjusting the values of the key parameters k_1^0 , k_2^0 , and D_O , it should be possible to determine the regimes in which each process controls the overall reaction. Some attention will also be given to the effect of geometric parameters in order to understand how the present model differs from previous iterations in that respect.

3.3.2.1 Rate Constants

Parametric studies were performed for values of k_1^0 between 0.01 and 10^6 $\text{m}^3/\text{mol}\cdot\text{s}$ and values of k_2^0 between 4.1×10^{-10} and 0.41 $\text{mol}\cdot\text{s}/(\text{kg}\cdot\text{m}^2)$. The latter value actually exceeds the maximum physically possible rate constant of $k_2^0 = 0.028$ $\text{mol}\cdot\text{s}/(\text{kg}\cdot\text{m}^2)$ corresponding to a sticking coefficient of 1. Nevertheless it was informative to consider extreme values of both rate constants. Representative impedance plots for $k_1^0 = 10$ $\text{m}^3/\text{mol}\cdot\text{s}$ and four different values of k_2^0 are shown in Figure 41. In order to compare impedance plots which vary greatly in magnitude, the results have been plotted on a logarithmic scale. The high frequency arc appears the same for all four cases, which is expected since the electrolyte impedance should be independent of the electrode reaction parameters. For smaller values of k_2^0 (e.g. 4.1×10^{-10} $\text{mol}\cdot\text{s}/(\text{kg}\cdot\text{m}^2)$), two distinct arcs are apparent in the lower frequency portion of the spectrum, indicating possible resistive contributions from two different electrode processes. As the adsorption rate approaches infinity, the low frequency impedance collapses to a single arc as seen in the case where $k_2^0 = 0.41$ $\text{mol}\cdot\text{s}/(\text{kg}\cdot\text{m}^2)$ (for the purposes of the present study this was found to be large enough to be

considered “infinite” within the numerical uncertainty of the model). This suggests, unsurprisingly, that the lowest frequency arc corresponds to the adsorption/desorption process unless k_2^0 is very large (in which case the adsorptive impedance contribution is necessarily negligible). The remaining electrode impedance is presumably due to the charge transfer reaction.

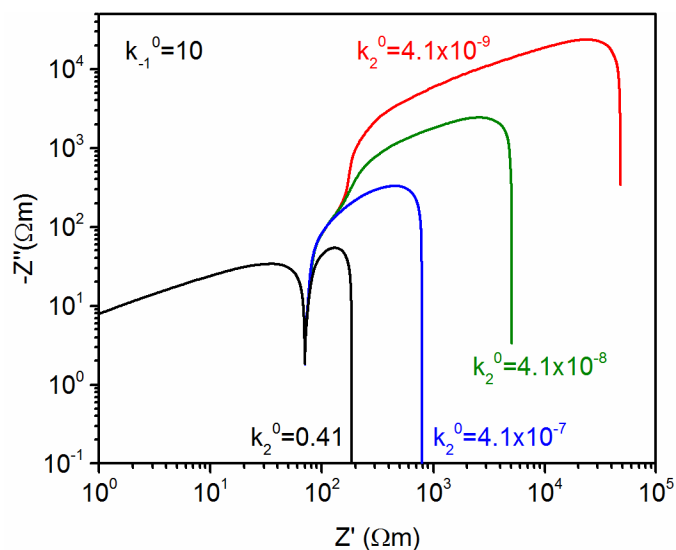


Figure 41. Simulated impedance spectra for $k_{-1}^0 = 10 \text{ m}^3/\text{mol}\cdot\text{s}$ and four different values of k_2^0 in $\text{mol}\cdot\text{s}/(\text{kg}\cdot\text{m}^2)$, plotted on a logarithmic scale. The frequency range is $10^{-2} \text{ Hz} \leq f \leq 10^9 \text{ Hz}$.

The spacing of the low frequency ends of the spectra in Figure 41 suggests a proportionality between k_2^0 and the electrode resistance R_{ode} . This can be confirmed by calculating the resistance at very low frequency for each value of k_2^0 and subtracting the electrolyte resistance to obtain the quasi-DC electrode resistance. This is analogous to the calculation of intermediate frequency resistance in the previous section using (66). For the spectra shown in Figure 41, R_{ode} is proportional to $1 / k_2^0$

when $k_2^0 \geq 10^{-7} \text{ mol}\cdot\text{s}/(\text{kg}\cdot\text{m}^2)$, but deviates from this proportionality for the largest value of k_2^0 . The relationship between the reaction rate constants and electrode resistance will be investigated in greater detail later in this section.

Figure 42 shows an impedance plot for simulations with $k_1^0 = 0.1 \text{ m}^3/\text{mol}\cdot\text{s}$ (i.e. the charge transfer reaction is two orders of magnitude slower than in Figure 41). Again, a single low frequency arc is observed for the largest value of k_2^0 , transitioning to two distinct arcs as the adsorption rate is reduced. Unlike Figure 41, the electrode resistance of the arcs in Figure 42 is no longer inversely proportional to k_2^0 . This result seems reasonable as the charge transfer reaction is expected to have more of an effect in the present case. This can be confirmed by examining the intermediate frequency arc, which is presumed to correspond to charge transfer. As expected, the intermediate frequency arc in Figure 42 is much more prominent as compared to Figure 41. In Figure 41, the quasi-DC resistance is approximately $110 \text{ }\Omega\text{m}$ for the case with $k_2^0 = 0.41 \text{ mol}\cdot\text{s}/(\text{kg}\cdot\text{m}^2)$. In Figure 42 the quasi-DC resistance is approximately 100 times larger for the same value of k_2^0 , suggesting a direct proportionality between the magnitude of the intermediate arc and charge transfer resistance.

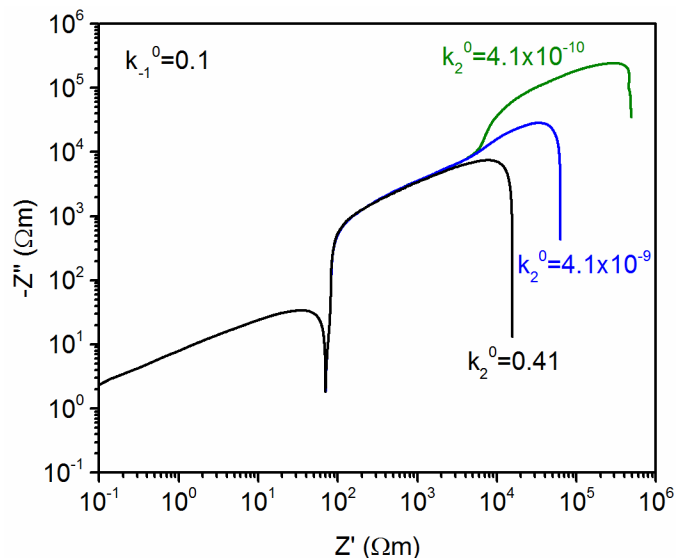


Figure 42. Simulated impedance spectra for $k_{-1}^0 = 0.1 \text{ m}^3/\text{mol}\cdot\text{s}$ and three different values of k_2^0 in $\text{mol}\cdot\text{s}/(\text{kg}\cdot\text{m}^2)$, plotted on a logarithmic scale. The frequency range is $10^{-2} \text{ Hz} \leq f \leq 10^9 \text{ Hz}$.

When the charge transfer rate constant k_{-1}^0 is increased to $1000 \text{ m}^3/\text{mol}\cdot\text{s}$, unexpected results are observed. Figure 43 shows several such impedance spectra for various values of k_2^0 . When the adsorption rate is relatively small, the low and high frequency impedance arcs appear normal, but a “loop” is observed in the 0.1–10 MHz range where the impedance spectrum doubles back on itself; i.e. the impedance actually increases with frequency over part of this range. This is not consistent with experimental observation, nor with an intuitive expectation of the model behavior; i.e. that the charge transfer reaction should remain in equilibrium when k_{-1}^0 is very large. It is believed that the anomalous effect is caused by an unintended violation of the model assumptions—namely, either the assumption that diffusivity of adsorbed oxygen is coverage-independent, or that of continuum diffusion of oxygen vacancies in the electrolyte. When charge transfer is extremely facile, the result is a depletion of

adsorbed O and an excess of filled O sites near the TPB (under cathodic polarization). If taken to extremes, this can result in the anodic reaction rate exceeding the cathodic rate even under cathodic polarization, which is certain to cause unexpected effects. This was verified by observing that the IV curve for the present combination of parameters does not pass through the origin. In a real system, a runaway charge transfer reaction would be kept in check by a slowdown of vacancy diffusion due to the excess of filled oxygen sites, or an increase in diffusivity of adsorbed O at low coverage. However, the model assumed that both diffusivities were constant, preventing such mediation of the charge transfer rate.

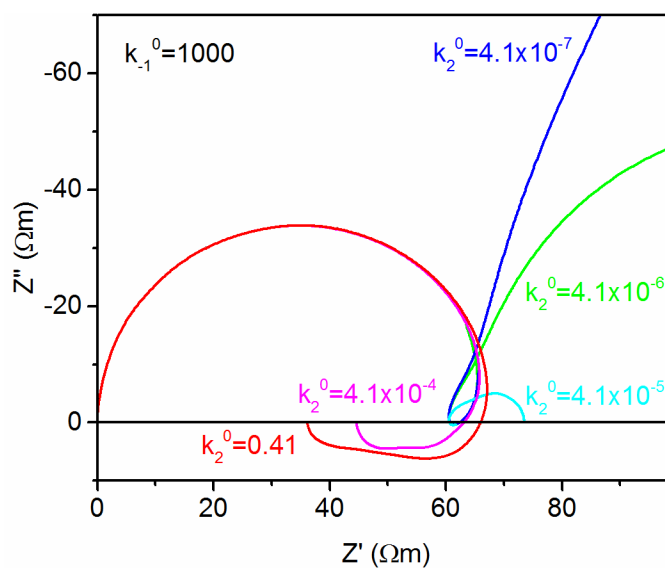


Figure 43. Simulated impedance spectra for $k_{-1}^0 = 1000 \text{ m}^3/\text{mol}\cdot\text{s}$ and five different values of k_2^0 in $\text{mol}\cdot\text{s}/(\text{kg}\cdot\text{m}^2)$, plotted on a linear scale. The frequency range is $10^{-2} \text{ Hz} \leq f \leq 10^9 \text{ Hz}$.

The model results become even more unexpected as the adsorption rate becomes very large in addition to the charge transfer rate. As seen in the figure, the

low frequency arc in this case actually shifts into the positive imaginary axis. The magnitude of this inductive feature increases with increasing k_2^0 so that the quasi-DC resistance of the specimen for very rapid adsorption is actually less than the electrolyte resistance. This result is obviously non-physical as there cannot be a negative resistance associated with the electrode. However, it is not cause for concern since the model assumes that either adsorption, diffusion, charge transfer, or a combination of these is the rate limiting reaction step. If both adsorption and charge transfer are extremely rapid, then obviously one of the other electrode reaction steps must be rate limiting instead and the model is no longer valid. At first glance, it seems that diffusion of adsorbed oxygen to the TPB could instead be rate-limiting when adsorption is very fast, but keeping in mind the co-limited adsorption/diffusion process discussed in Section 1.1.3.1, it becomes evident that this is not the case. That is, when adsorption is extremely facile, any oxygen consumed by the charge transfer reaction can be immediately replaced by newly adsorbed oxygen directly at the TPB. In this case, the mean diffusion length of adsorbed oxygen is very small and consequently the effect of diffusion is negligible. This will be explored more fully in Section 3.3.2.2, where the effect of varying the diffusivity of adsorbed oxygen will be explored.

The non-physical results observed in Figure 43 are not useful in understanding the physical behavior of the Pt, O₂|YSZ system, but they do give an upper bound on realistic values of the reaction rate coefficients. It can be concluded that if k_1^0 is on the order of 100 m³/mol·s or larger, the model assumption of concentration-independent diffusivity of adsorbed oxygen and/or oxygen vacancies is violated. Therefore, the model is not valid for such cases. Of course, it is possible that the actual value of k_1^0

in a real system exceeds this range, and the model would not be useful for experimental fitting. However, it would be relatively straightforward to reformulate the model to allow for concentration-dependent diffusivities if it becomes necessary in the future.

In order to better understand the effect of the charge transfer reaction, it is helpful to compare the impedance spectra for different values of k_{-1}^0 directly on the same plot. Figure 44 shows three impedance spectra with $k_2^0 = 4.1 \times 10^{-9} \text{ mol}\cdot\text{s}/(\text{kg}\cdot\text{m}^2)$ (two of which were already plotted in Figures 41 and 42). It is now possible to observe more clearly a distinct increase in magnitude of the intermediate frequency arc with decreasing k_{-1}^0 . It can also be observed from the low frequency ends of the spectrum that the electrode resistance is not proportional to k_{-1}^0 , which makes sense because the present adsorption rate is quite slow and so adsorption is expected to have a large influence on the electrode resistance.

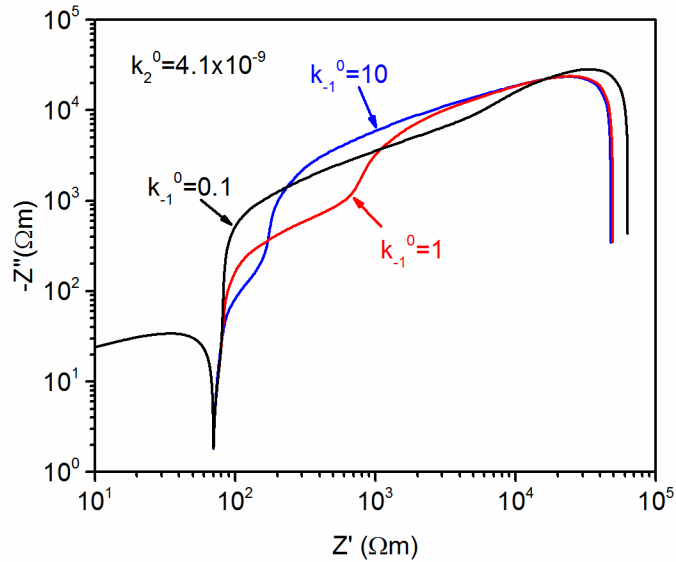


Figure 44. Simulated impedance spectra for $k_2^0 = 4.1 \times 10^{-9} \text{ mol}\cdot\text{s}/(\text{kg}\cdot\text{m}^2)$ and three different values of k_{-1}^0 in $\text{m}^3/\text{mol}\cdot\text{s}$, plotted on a logarithmic scale. The frequency range is $10^{-2} \text{ Hz} \leq f \leq 10^9 \text{ Hz}$.

A plot analogous to Figure 44, but this time with $k_2^0 = 4.1 \times 10^{-7} \text{ mol}\cdot\text{s}/(\text{kg}\cdot\text{m}^2)$, is shown in Figure 45. That is, the adsorption reaction is now two orders of magnitude faster. In this case only a single low frequency impedance arc is evident regardless of the value of k_{-1}^0 . Despite the appearance of a single electrode process (presumably charge transfer) in this case, revisiting Figure 41 shows that adsorption still contributes to the electrode impedance when $k_2^0 = 4.1 \times 10^{-7} \text{ mol}\cdot\text{s}/(\text{kg}\cdot\text{m}^2)$. It is therefore apparent that the capacitances associated with the adsorption and charge transfer processes are relatively similar in this case, leading to overlapping arcs. This demonstrates how a single “electrode” arc appearing in an impedance spectrum may actually arise due to a combination of processes rather than a single rate-limiting reaction step. It is clear that analysis using a simpler model (e.g. an equivalent circuit) would yield unsatisfactory results in such a case.

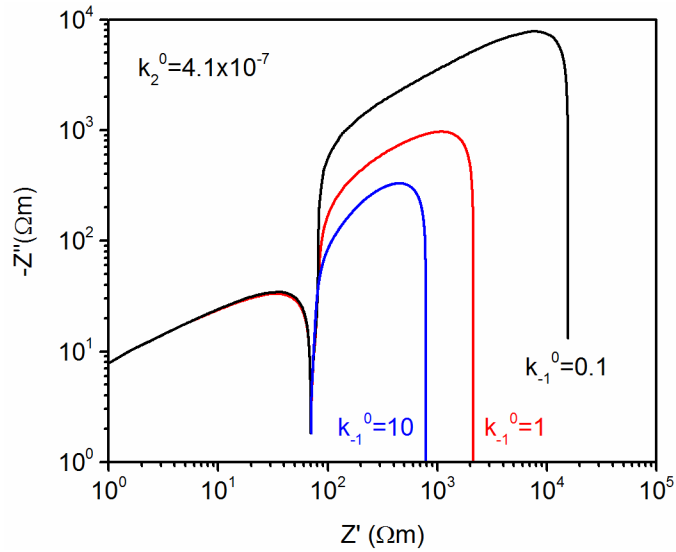


Figure 45. Simulated impedance spectra for $k_2^0 = 4.1 \times 10^{-7} \text{ mol}\cdot\text{s}/(\text{kg}\cdot\text{m}^2)$ and three different values of k_{-1}^0 in $\text{m}^3/\text{mol}\cdot\text{s}$, plotted on a logarithmic scale. The frequency range is $10^{-2} \text{ Hz} \leq f \leq 10^9 \text{ Hz}$.

The proportionalities between k_{-1}^0 and k_2^0 and the electrode resistance can be better understood by examining the extreme low frequency (quasi-DC) response of the model. Figure 46 shows the total quasi-DC resistance R_{total} predicted by the model for various combinations of the two rate constant parameters. This measurement includes the both the electrolyte and electrode resistance, so it was expected that as the rate constants approach infinity, R_{total} will approach the electrolyte resistance, indicated by a dashed line in the figure. However, the figure shows that the resistance actually approaches a value near $32 \text{ } \Omega\text{m}$ as both rate constants approach infinity. This apparent negative electrode resistance is the same effect observed for large values of k_2^0 in Figure 43, confirming that the model no longer simulates real behavior when charge transfer is very fast. The curves extending below the horizontal dashed line in the figure therefore correspond to values of k_{-1}^0 resulting in unrealistic behavior. The

figure confirms that, as noted earlier, the model is no longer valid when k_{-1}^0 is on the order of $100 \text{ m}^3/\text{mol}\cdot\text{s}$ or larger.

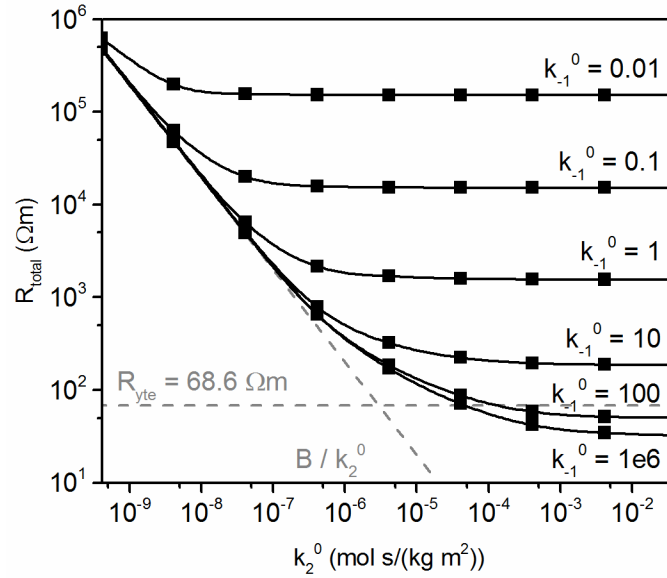


Figure 46. Quasi-DC resistance R_{total} as a function of the reaction rate constants k_{-1}^0 (in $\text{m}^3/\text{mol}\cdot\text{s}$) and k_2^0 (in $\text{mol}\cdot\text{s}/(\text{kg}\cdot\text{m}^2)$) for a specimen with $L_{yte} = 50 \text{ nm}$, $L_{ode} = 25 \text{ nm}$, $h_{yte} = 10 \text{ nm}$, and $h_{act} = 1 \text{ nm}$.

In the case of very slow adsorption (small values of k_2^0), R_{total} is essentially independent of k_{-1}^0 and obeys an inverse proportionality with k_2^0 , indicated by the diagonal dashed line in the figure with a constant of proportionality B . As k_2^0 is increased, R_{total} approaches a constant value which is inversely proportional to k_{-1}^0 . Thus the electrode reaction can be dominated by adsorption (with $R_{total} \propto 1/k_2^0$) or by charge transfer with ($R_{total} \propto 1/k_{-1}^0$) depending on the relative magnitudes of k_{-1}^0 and k_2^0 . There also exists an intermediate regime where both adsorption and charge

transfer control the overall reaction rate. This will be studied more quantitatively in Section 4.3.3.

3.3.2.2 Diffusivity

While the diffusivity of adsorbed oxygen on a platinum surface has been measured,¹¹⁶ the rate limiting effects of surface diffusion can still be investigated by varying this diffusivity in the simulation. Figure 47 shows representative impedance spectra for three cases with a moderate adsorption rate ($k_2^0 = 4.1 \times 10^{-7} \text{ mol} \cdot \text{s}/(\text{kg} \cdot \text{m}^2)$) and three different values of the adsorbed oxygen diffusivity D_{Oad} : 10^{-13} , 10^{-12} (which is approximately the value given in the literature), and $10^{-11} \text{ m}^2/\text{s}$. As observed in Section 3.3.2.1, the chosen adsorption rate is within the regime where adsorption has a measurable influence on the electrode impedance. Decreasing the diffusivity from 10^{-12} to $10^{-13} \text{ m}^2/\text{s}$ causes the electrode resistance to roughly double from 722 to 1470 Ωm , while increasing the diffusivity from 10^{-12} to $10^{-11} \text{ m}^2/\text{s}$ causes a decrease of around 16% to 605 Ωm . This demonstrates that, at least within a certain range of parameter values, the overall electrode impedance is jointly controlled by the oxygen adsorption and diffusion as discussed in Section 1.1.3.1.

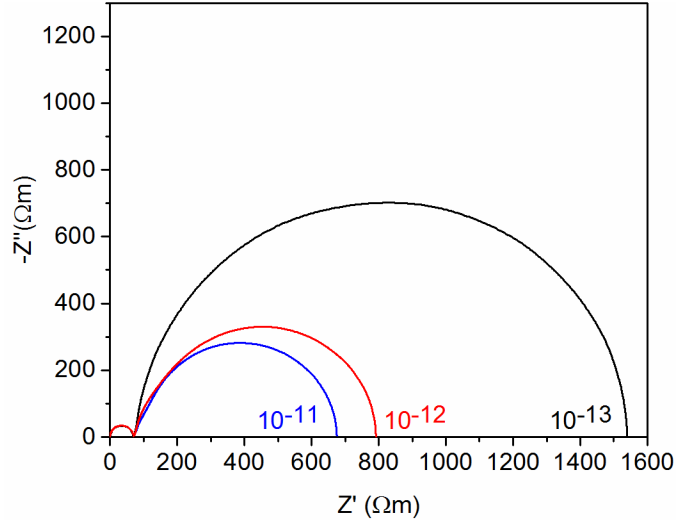


Figure 47. Simulated impedance spectra for three specimens with $k_{-1}^0 = 10 \text{ m}^3/\text{mol}\cdot\text{s}$, $k_2^0 = 4.1 \times 10^{-7} \text{ mol}\cdot\text{s}/(\text{kg}\cdot\text{m}^2)$, and the respective values of D_{Oad} indicated (in m^2/s). The geometric parameters are $L_{yte} = 50 \text{ nm}$, $L_{ode} = 25 \text{ nm}$, $h_{yte} = 10 \text{ nm}$, and $h_{act} = 1 \text{ nm}$.

On the other hand, when the adsorption rate is very large, the diffusivity of adsorbed oxygen has almost no effect. This is demonstrated in Figure 48, which like Figure 47 shows a set of three impedance spectra corresponding to the diffusivities $D_{Oad} = 10^{-13}$, 10^{-12} , and $10^{-11} \text{ m}^2/\text{s}$, respectively. However, the value of k_2^0 has now been increased to $0.41 \text{ mol}\cdot\text{s}/(\text{kg}\cdot\text{m}^2)$, which is sufficiently large to render the electrode impedance independent of adsorption rate. All other parameters are identical to the previous case. As seen in the figure, all three spectra overlap perfectly, showing no effect due to varying D_{Oad} . This provides more evidence of the statement put forth in Section 3.3.2.1 that diffusion can be rate limiting only in conjunction with adsorption. If adsorption is very fast, the diffusion process is bypassed by adsorption very close to the TPB, resulting in no dependence of the impedance on diffusivity (as seen in the figure). This can be confirmed by examining the adsorption rate along the

electrode surface. Figure 49 shows the adsorption rate under 1 mV cathodic DC polarization as a function of position along the centerline of the surface layer ABD for $D_{Oad} = 10^{-12} \text{ m}^2/\text{s}$ and two different values of k_2^0 . (The positioning of the centerline is shown in Figure 39.) The adsorption rates have been normalized for ease of comparison as the maximum adsorption rates for the two different cases vary by orders of magnitude. For the low to intermediate k_2^0 case, the adsorption reaction is spread over the entire electrode surface, meaning much of the oxygen adsorbs far from the triple phase boundary. Therefore the rate at which oxygen can diffuse from its adsorption site to the triple phase boundary partially controls the overall reaction rate. Conversely, when k_2^0 is large, almost all of the oxygen adsorbs directly at the triple phase boundary and the diffusivity becomes irrelevant.

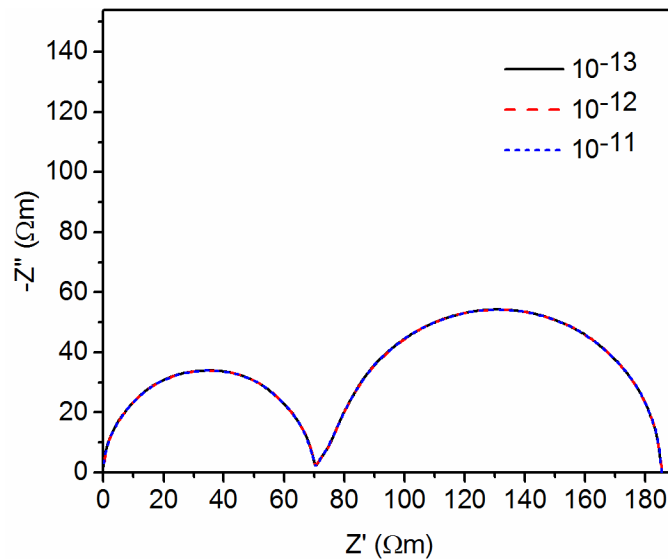


Figure 48. Simulated impedance spectra for three specimens with $k_{-1}^0 = 10 \text{ m}^3/\text{mol}\cdot\text{s}$, $k_2^0 = 0.41 \text{ mol}\cdot\text{s}/(\text{kg}\cdot\text{m}^2)$, and the respective values of D_{Oad} indicated (in m^2/s). The geometric parameters are $L_{yte} = 50 \text{ nm}$, $L_{ode} = 25 \text{ nm}$, $h_{yte} = 10 \text{ nm}$, and $h_{act} = 1 \text{ nm}$.

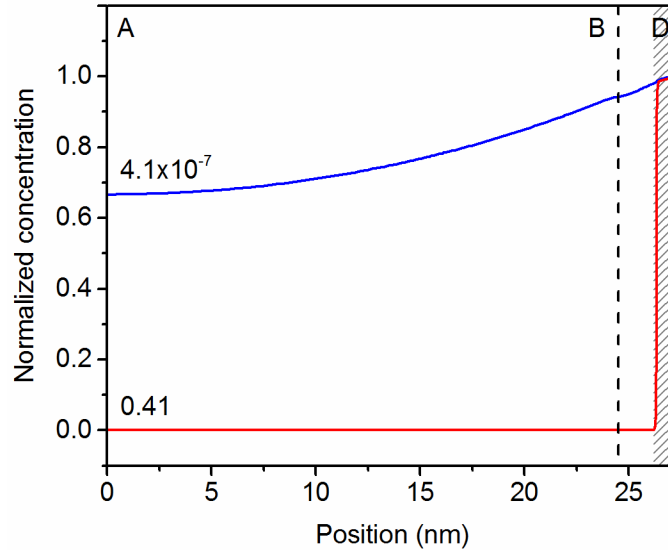


Figure 49. Normalized adsorption rate along the centerline of the electrode surface layer and TPB (see Figure 39) for a specimen with $k_{-1}^0 = 10 \text{ m}^3/\text{mol}\cdot\text{s}$, $D_{Oad} = 10^{-12} \text{ m}^2/\text{s}$, and the indicated values of k_2^0 in $\text{mol}\cdot\text{s}/(\text{kg}\cdot\text{m}^2)$ under a cathodic DC polarization of $\eta = -1 \text{ mV}$. The dashed line indicates the bend at the electrode corner B , and the shaded area represents the TPB. The maximum adsorption rates in $\text{mol}/(\text{m}^3\cdot\text{s})$ are 3.1×10^5 for $k_2^0 = 4.1 \times 10^{-7}$ and 2.8×10^7 for $k_2^0 = 0.41$.

3.3.2.3 Geometry

In Section 3.2 it was observed that the electrolyte thickness and electrode finger geometry can have a significant effect on not only the magnitude of the impedance, but also the shape of the spectrum. Many of these effects, in particular those related to current spreading in electrolytes with very large aspect ratios, have already been explored in detail in Section 3.2 using a simpler model and will not be revisited in depth. Nevertheless, it is worth investigating some of the geometric impedance effects of the diffusion-reaction model to determine whether the results are

plausible and consistent with previous findings. Figure 50 shows three impedance spectra for otherwise identical specimens with different electrolyte thicknesses. The electrolyte resistance behaves as expected, decreasing with increasing thickness and closely matching the theoretical resistance predicted by (63). In the case of a very thick electrolyte, the electrolyte resistance becomes independent of thickness since, due to the electrode geometry, ionic conduction occurs near the electrolyte surface. The addition of electrolyte volume far from the surface region therefore does not improve ionic conductance in the electrolyte. These findings are consistent with the model presented in Section 2.3 (c.f. Figure 30).

Intuitively, the electrode resistance is expected to be completely independent of the electrolyte geometry, yet in Figure 50 a decrease in electrode resistance can be observed with decreasing thickness. A decrease of approximately 2.5% is observed in R_{ode} when h_{yte} is decreased from 20 nm to 10 nm, and a further decrease of approximately 5% is observed when h_{yte} is decreased from 10 nm to 5 nm. The cause of this unintuitive behavior has not yet been determined, although it is possible that for such extremely small electrolyte volumes, the free vacancy concentration actually becomes small enough to affect the charge transfer rate. Nevertheless, the effect is negligible for an electrolyte thickness greater than 20 nm. Therefore investigating the precise cause of this effect will be left for future work, with the caveat that caution may be required in applying the model to very thin films.

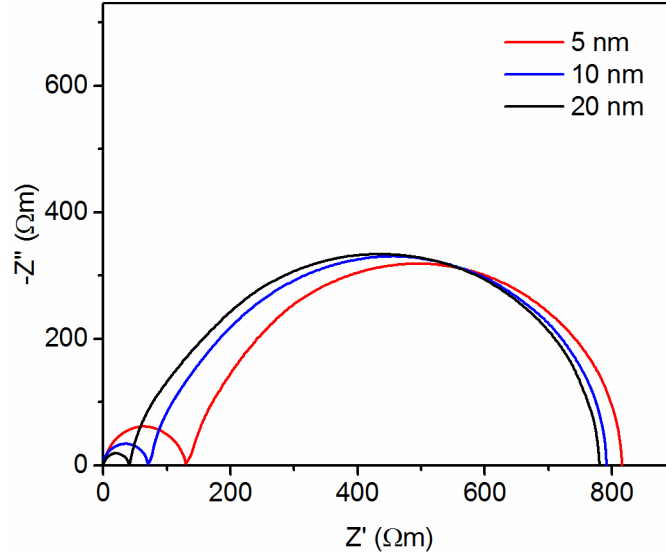


Figure 50. Impedance spectra for three specimens with $k_{-1}^0 = 10 \text{ m}^3/\text{mol}\cdot\text{s}$, $k_2^0 = 4.1 \times 10^{-7} \text{ mol}\cdot\text{s}/(\text{kg}\cdot\text{m}^2)$, and the respective values of h_{yte} indicated. The electrolyte dimensions are $L_{yte} = 50 \text{ nm}$ and $L_{ode} = 25 \text{ nm}$ for all specimens.

In addition to electrolyte thickness, the electrode finger width and spacing are also important geometric parameters. Figure 51 shows impedance spectra for three otherwise identical specimens with different electrode finger widths. The electrolyte resistance behaves as expected, decreasing with increasing finger width and closely matching the theoretical resistance predicted by (63). The electrode resistance decreases with increasing finger width as well, most strikingly when L_{ode} is small. This behavior can be attributed to the rate-controlling adsorption reaction, which naturally proceeds faster when more platinum surface area is available for adsorption. If this is indeed the case, then the same behavior is not expected if the model parameters are adjusted so adsorption is no longer rate limiting. Figure 52 shows the electrode resistance R_{ode} versus the finger width ratio L_{ode}/L_{yte} for the case corresponding to Figure 51 where $k_2^0 = 4.1 \times 10^{-7} \text{ mol}\cdot\text{s}/(\text{kg}\cdot\text{m}^2)$, as well as a case where k_2^0 is very large

($0.41 \text{ mol}\cdot\text{s}/(\text{kg}\cdot\text{m}^2)$) and the electrode reaction is no longer controlled by adsorption. As already observed, R_{ode} increases markedly for $L_{ode}/L_{yte} < 0.5$ when adsorption is the rate controlling process. However, when charge transfer rather than adsorption is the limiting step, the electrode resistance actually shows a slight *increase* with increasing finger width. This trend appears to be linear. As with the relationship between electrolyte thickness and electrode resistance, this effect may be related to the free vacancy concentration in a very small electrolyte volume. Since this effect too is observed only in an extreme parameter regime that is not at all representative of reality (exceeding the maximum value of k_2^0 that is physically possible), any further investigation will be left for future work.

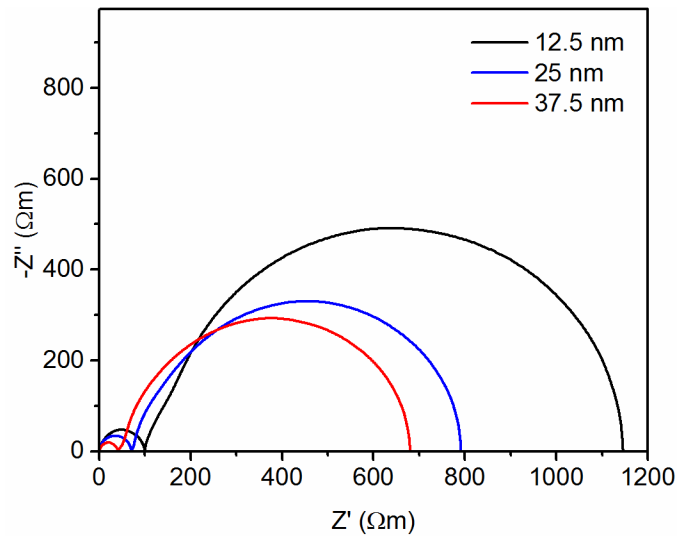


Figure 51. Impedance spectra for three specimens with $k_{-1}^0 = 10 \text{ m}^3/\text{mol}\cdot\text{s}$, $k_2^0 = 4.1 \times 10^{-7} \text{ mol}\cdot\text{s}/(\text{kg}\cdot\text{m}^2)$, and the respective values of L_{ode} indicated. The electrolyte dimensions are $L_{yte} = 50 \text{ nm}$ and $h_{yte} = 10 \text{ nm}$ for all specimens.

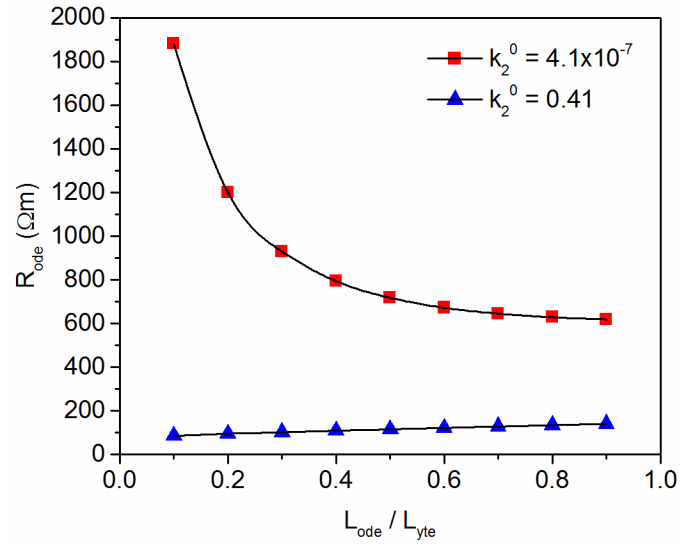


Figure 52. Electrode resistance vs. finger width ratio for two different values of k_2^0 . The electrolyte dimensions are $L_{yte} = 50$ nm and $h_{yte} = 10$ nm, and $k_1^0 = 10$ m³/mol·s for all specimens.

Chapter 4

DISCUSSION

4.1 Grain Boundary Heterogeneity Study

The results of Section 3.1 suggested that CPE-based equivalent circuit models can provide an acceptable estimate of the mean grain boundary properties even when the conductivity and/or permittivity of the grain boundaries are heterogeneous. Furthermore, the possibility that the CPE parameter n_{gb} could provide a quantitative measure of the heterogeneity (i.e. standard deviation or similar) was discussed. The effectiveness of such procedures, and their consequences to experimental study, will now be discussed more thoroughly.

4.1.1 Estimation of Average Grain Boundary Conductivity

Based on Figure 21, it was observed that calculating the grain boundary conductivity using (20) appears to give a fairly good estimate of the actual mean value for specimens with heterogeneous conductivity. However, the results can be made more quantitative by plotting the estimated conductivity against the true sample mean, as shown in Figure 53. The figure collects together all of the impedance spectra obtained in Sections 3.1.2–3.1.4 for all three grain sizes, including samples (not previously shown) where σ_{gb} and ϵ_{gb} were both heterogeneous. The ideal case where the apparent conductivity is equal to the actual mean value is indicated in the figure by a dashed line. The data points falling near the line represent relatively accurate estimates of the conductivity, while those farther away represent less accurate estimates. It can be observed from the figure that the worst-case error in the conductivity estimates was approximately 30%.

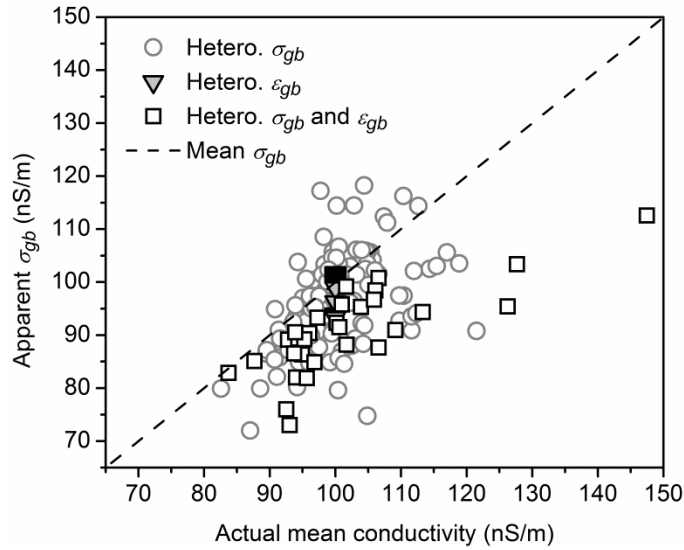


Figure 53. Apparent grain boundary conductivity calculated from (20) vs. actual mean conductivity for all specimens. Data are shown for samples with heterogeneous conductivity and homogeneous permittivity (circles), heterogeneous permittivity and homogeneous conductivity (triangles), and both heterogeneous conductivity and permittivity (squares). The mean grain boundary conductivity is indicated by a dashed line.

For the researcher, it would be useful to be able to estimate an upper bound on the error in the conductivity estimate. Presumably the accuracy of the conductivity estimate improves as the grain boundary impedance arc approaches a perfect semicircle; that is, as the CPE exponent n_{gb} approaches 1. This is confirmed by Figure 54, which plots the percent error of each conductivity estimate in Figure 53 against n_{gb} . The figure indicates that when the CPE exponent is 0.9 or greater, an error of approximately 13% or less is predicted for the calculation of the average σ_{gb} from the equivalent circuit fit.

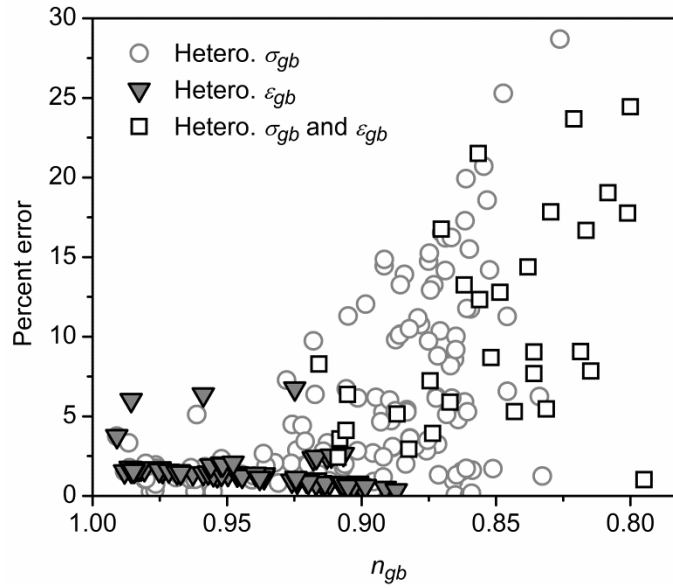


Figure 54. Percent error in apparent conductivity calculated from (20) vs. equivalent circuit exponent n_{gb} . Data are shown for samples with heterogeneous conductivity and homogeneous permittivity (circles), heterogeneous permittivity and homogeneous conductivity (triangles), and both heterogeneous conductivity and permittivity (squares).

The present study included σ_{gb} and ε_{gb} distributions which were quite broad, perhaps more so than would be likely in a real polycrystal. In actuality, the variation in grain boundary properties in polycrystals has not been studied much, although Fleig et al. have demonstrated a procedure for measuring the impedance of a single grain boundary using microcontacts⁶² which could be used for this purpose. Nevertheless, the variation in grain boundary properties in real polycrystals is not expected to be larger than the distributions used here. Based on Figures 53 and 54, the resistance obtained from an R-CPE equivalent circuit therefore appears to allow satisfactory determination of the mean grain boundary conductivity in a polycrystalline electrolyte

(within 30%) despite heterogeneous grain boundary conductivity and/or permittivity. Furthermore, the conductivity can be estimated within 13% when $n_{gb} \geq 0.9$.

As noted earlier, it is expected that valid results would also be obtained for specimens with heterogeneous grain boundary thickness since this case is equivalent to simultaneous heterogeneity of conductivity and permittivity. The σ_{gb} and ε_{gb} distributions considered in the present study would equate to more than an order of magnitude of variation in w_{gb} . Of course, the conductivity calculation can also be influenced by other considerations such as heterogeneous grain geometry and lateral variation of grain boundary properties. Numerical simulation of 19 randomly generated two-dimensional microstructures by Fleig⁴⁶ predicted less than 20% error in σ_{gb} and ε_{gb} calculations in the case of quasi-realistic polycrystals with homogeneous grain boundary properties. Considering the possible additional influence of curved or faceted grain boundaries, Fleig made a rough estimate of a factor of 2 for the upper bound on the error. Lateral heterogeneity of grain boundaries, on the other hand, has the potential to severely complicate quantitative analysis of impedance spectra.⁴¹ Although more work is needed to explore the limits of CPE-based equivalent circuit modeling quantitatively, these results provide a degree of confidence that such modeling is able to provide at least some quantitative value in estimating grain boundary conductivity in real polycrystals.

4.1.2 Estimation of Average Grain Boundary Permittivity

Determining the mean grain boundary permittivity is less straightforward. In order to make use of (22), the grain boundary capacitance C_{gb} must be quantified. However, this value cannot be obtained directly from the equivalent circuit fit. In the previous sections this issue was addressed by making the assumption that $C_{gb} = Q_{gb}$,

with generally unsatisfactory results. The apparent permittivity calculated using this simplification (represented by triangles) is plotted against the actual mean grain boundary permittivity in Figure 55. All available data, including samples with heterogeneous conductivity, heterogeneous permittivity, and heterogeneous distributions of both parameters, are included. In many cases the permittivity estimates are very poor, differing by as much as a factor of 4 from the mean grain boundary permittivity. Therefore a method to better quantify C_{gb} is needed.

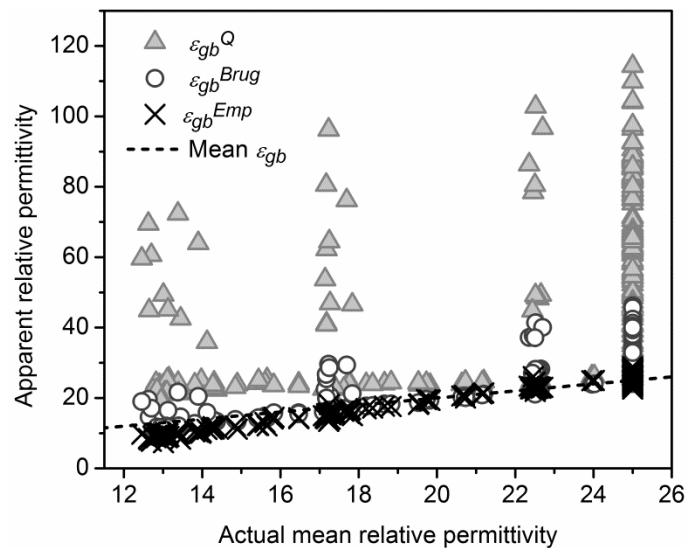


Figure 55. Apparent grain boundary permittivity vs. actual mean permittivity for all specimens. Apparent permittivity was calculated using one of three capacitance expressions: the assumption $C_{gb} = Q_{gb}$ (triangles), Brug’s equation (9) (circles), and a new empirical equation (70) (Xs). The mean permittivity is indicated by a dashed line.

As discussed in Section 1.2.2, the established method is to calculate an “equivalent capacitance” from the CPE parameters using Brug’s equation (9). The permittivity can then be calculated from the equivalent capacitance using (22).

Applying this method to the present dataset results in a better estimate of the mean permittivity, represented by circles in Figure 55. However, the apparent permittivity values still vary from the actual mean by as much as 85% and the goodness of fit for these data points to the line in Figure 55 is quite poor with $R^2 = 0.21$. Equation (9) appears to perform best when the grain boundary conductivity is relatively homogeneous; the largest errors occur when the conductivity values are widely distributed. Considering only samples with $n_{gb} > 0.9$, the equation performs considerably better with $R^2 = 0.83$ and a maximum error of 30%.

Further improvement in the permittivity estimate was obtained using an empirical expression for effective capacitance,

$$C_{Emp} = 1.07R^{0.78(1-n)}Q^{1/n} \quad (70)$$

which was obtained via least-squares fitting of various modified forms of (9) to the data. Combining this expression with (22) and expressing the result in terms of the sample aspect ratio yields

$$\epsilon_{gb}^{Emp} = 1.07 \frac{H_y}{H_x} \frac{w_{gb}}{h} R_{gb}^{0.78(1-n_{gb})} Q_{gb}^{1/n_{gb}} \quad (71)$$

As indicated by Xs in Figure 55, this equation gives an estimate of ϵ_{gb} within 45% of the actual mean value for all cases considered, and the goodness of fit improves considerably to $R^2 = 0.90$. When $n_{gb} > 0.9$, the maximum error is essentially the same as that of Brug's equation (approximately 30%), but the overall goodness of fit is better with $R^2 = 0.92$. Thus (71) yields a substantially better estimate of permittivity than Brug's equation, particularly when the grain boundary conductivity is widely distributed. Equation (71) therefore has the potential to be useful in experimental determinations of grain boundary permittivity.

Since SOFCs are operated under DC conditions, the grain boundary permittivity is generally of less interest than the conductivity. However, (70) can also be used to calculate the grain boundary thickness, which *is* an important parameter in DC operation. This can be accomplished by assuming a value of ε_{gb} (such as $\varepsilon_{gb} = \varepsilon_{grain}$) and then proceeding as before with w_{gb} , rather than ε_{gb} , as the unknown parameter. Still, further work is required to clarify the applicability of (70). In particular, it should be emphasized that the meanings of the numerical constants appearing in the equation are currently unknown, and their values may depend upon parameters not considered in the present study, particularly possible differences between two-dimensional and three-dimensional space behavior. Therefore caution should be exercised in applying the equation to experimental results. Nonetheless, it is clear that equation (9) can yield relatively poor estimates of the average grain boundary permittivity or thickness in some relevant situations.

4.1.3 Estimation of Heterogeneity

While R-CPE circuits seem to allow relatively easy determination of the average grain boundary conductivity and, with some effort, an estimate of the average grain boundary permittivity or thickness, there appears to be no useful way to estimate the distributions of either of these parameters from the equivalent circuit alone. Figure 20 shows a roughly linear relationship between n_{gb} and the standard deviation of $\log(\sigma_{gb})$, which in principle could be used to estimate the latter based on experimental results. However, a similar relationship between n_{gb} and the spread of the permittivity distribution is seen in Figure 23. Therefore it appears that distortion of the grain boundary impedance arc due to heterogeneous conductivity cannot be distinguished

from distortion due to heterogeneous permittivity, or, potentially, other heterogeneous parameters. Plots for n_{gb} versus the spread of both the σ_{gb} and ε_{gb} distributions for all 1 μm samples are shown in parts (a) and (b) of Figure 56, respectively, illustrating the difficulty of drawing quantitative conclusions based on the CPE exponent.

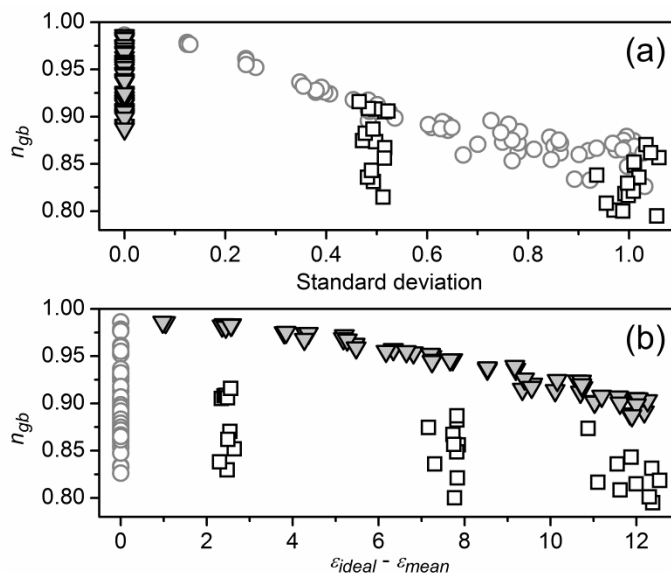


Figure 56. Equivalent circuit parameter n_{gb} vs. (a) standard deviation of $\log(\sigma_{gb})$ and (b) $\varepsilon_{ideal} - \varepsilon_{mean}$, a measure of the spread of ε_{gb} , for all samples with 1 μm grains. These samples include those with heterogeneous conductivity only (circles), heterogeneous permittivity only (triangles), and both heterogeneous conductivity and permittivity (squares).

4.2 Phenomenological Electrode Modeling Study

In Section 3.2, it was demonstrated that an intermediate frequency impedance feature resembling experimental results can arise due to current spreading at the electrode-electrolyte interface. However, it is not yet clear if this phenomenological electrode model is capable of explaining all aspects of the experimental results. This will now be explored further.

4.2.1 Fitting

In order to validate the phenomenological model, the calculated impedance spectra were compared to previously reported experimental impedance measurements of YSZ and GDC thin film samples with interdigitated platinum electrodes.^{20,55} The calculated spectra were fitted to the experimental data by adjusting the values of four parameters: electrolyte conductivity, permittivity, exchange current density, and double layer capacitance. All other model parameters, including geometric parameters and temperature, were fixed to the known values determined by the experimental conditions. An example result from this procedure for a Pt/GDC specimen at 652°C is shown in Figure 57. Although the experimental spectrum shows some depression of the low and high frequency arcs, the overall fit of the model is very good and all key features are captured. The ability to model the system with only four fitting parameters offers a notable advantage compared to a more conventional equivalent circuit. For example, the equivalent circuit in Figure 11 requires 9 fitting parameters. Furthermore, all four parameters determined by the model described in this work represent intuitively meaningful (if phenomenological) parameters of the system, which is not always the case for an equivalent circuit model.

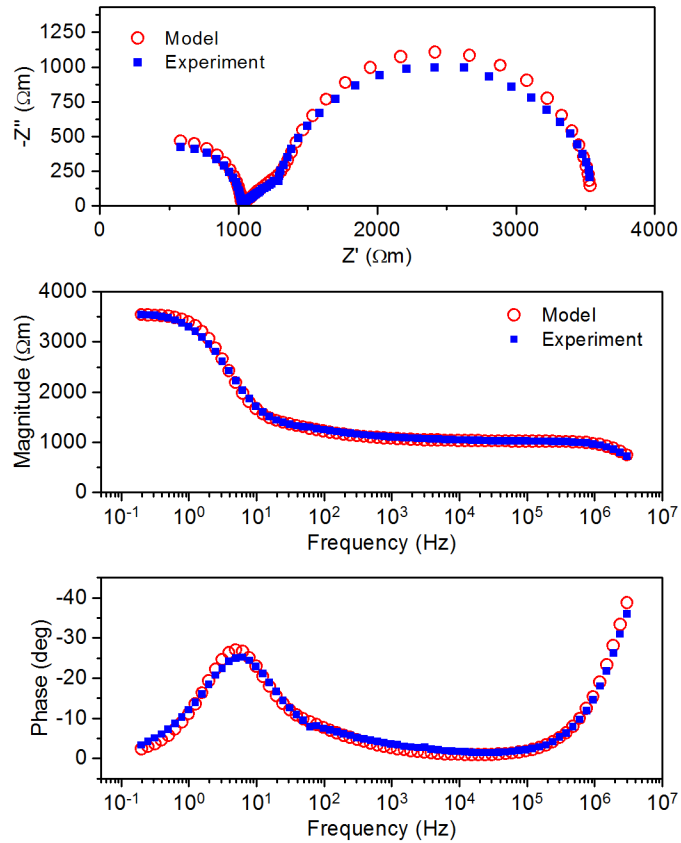


Figure 57. Bode and Nyquist plots of the impedance of a Pt/GDC specimen at 652°C, along with the model fit.

After repeating the fitting routine for a range of samples and temperatures, the values determined for the conductivity of YSZ and GDC thin films were compared to literature values. As the reported conductivities of YSZ and GDC thin films can vary widely, a representative selection of films most similar to those considered in the present study was compiled. These samples are listed in Table 4. The conductivities of representative bulk YSZ and GDC ceramics were also included. Since these measurements show a much smaller variation from sample to sample compared to the thin films, the bulk conductivities were reported as averages of several different

samples. The bulk YSZ conductivity was obtained by linear regression of 9 different samples, compiled in Reference 113. The conductivity of bulk GDC was obtained by linear regression of 3 different samples.^{118–120} The conductivity results are shown in Figure 58. It is evident that both the conductivity magnitude and activation energy for the YSZ sample agree closely with literature results for similar specimens and for the bulk ceramic. The activation energy for the GDC sample is somewhat smaller than the published bulk and thin film values; however, there is considerable variation among the literature results. The magnitude of the GDC conductivity obtained from the model is slightly reduced compared to the bulk GDC results, but well within the range of reported values for thin films.

Table 4. Properties of thin film YSZ and GDC specimens as reported in the literature

Material	Spec. no.	Dopant %	Thickness (nm)	Substrate	Ref.
YSZ	1	9.5	125	MgO (001)	121
YSZ	2	9.5	210	MgO (100)	122
YSZ	3	8.7	107	MgO (110)	123
YSZ	4	9	100	Al ₂ O ₃ (0001)	124
GDC	1	20	110	Al ₂ O ₃	125
GDC	2	20	170	MgO (001)	126
GDC	3a	20	100	Al ₂ O ₃	118
GDC	3b	20	100	SiO ₂	118
GDC	4a	21	500–1800	Al ₂ O ₃ (0001)	119
GDC	4b	21	500–1800	Pt (111)	119

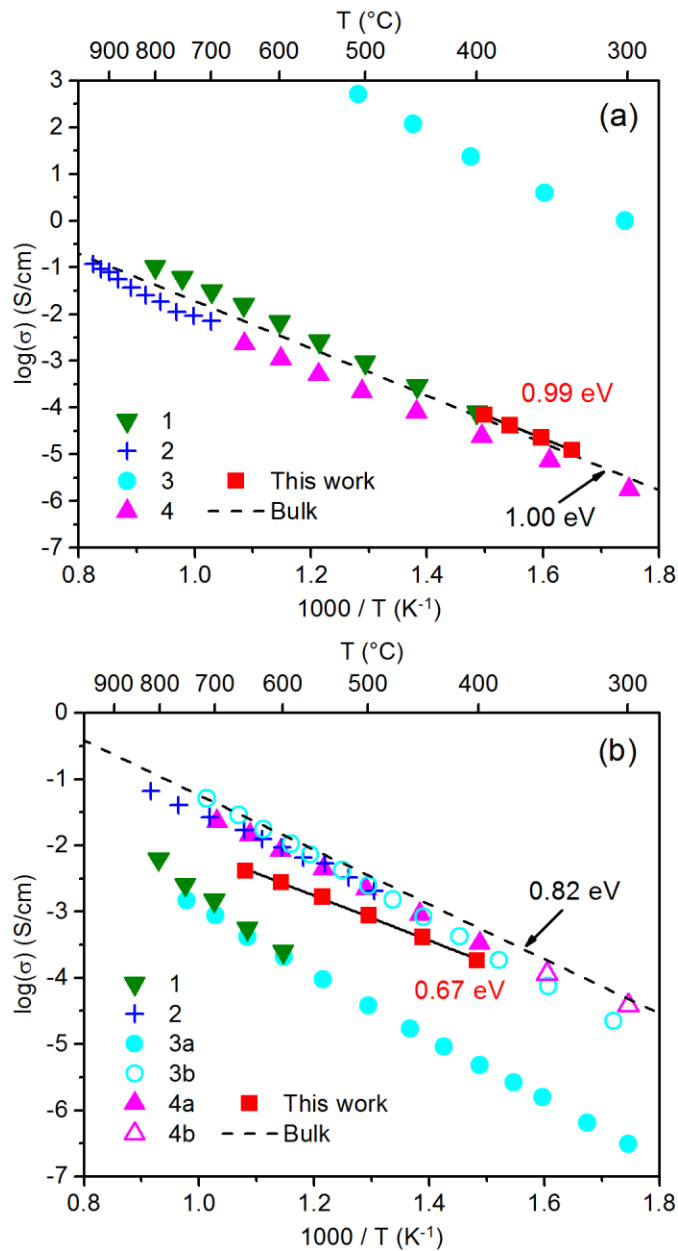


Figure 58. Arrhenius plot of electrolyte conductivity for (a) YSZ and (b) GDC thin films obtained by model fitting, compared to literature results for similar thin film specimens as well as bulk ceramics. The thin film specimens selected from the literature are compiled in Table 4. The bulk conductivities were obtained by linear regression of several sets of data as explained in the text. The activation energy obtained from the model results, as well as the bulk activation energy, is indicated in each plot.

The second parameter obtained by fitting experimental data, the exchange current density, is shown in Figure 59 along with several reported values of the same from the literature.^{25,26,71,127,128} The values obtained from the model for YSZ are slightly larger than the literature results when extrapolated to the lower measurement temperatures of the spectra fit in this work, but it bears mentioning that the reported values of J_0 vary by nearly an order of magnitude. Fewer values of J_0 are available for GDC, but the model agrees very well with the results from Reference 26.

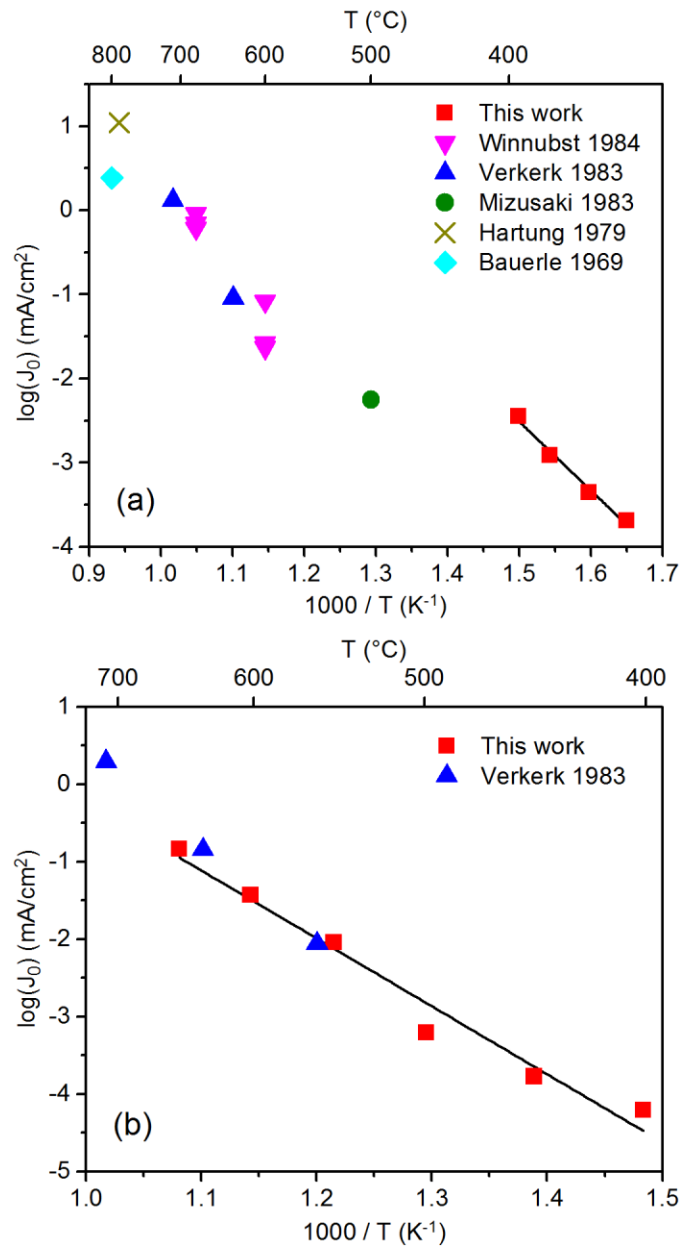


Figure 59. Arrhenius plot of exchange current density for Pt electrodes on (a) YSZ and (b) GDC. Model fit results from the present work are shown along with values reported previously in the literature.

The third fitting parameter determined from the model's fit to the experimental data is the double layer capacitance. The values determined for the YSZ samples increased monotonically with temperature, ranging from $290 \mu\text{F}/\text{cm}^2$ at 333°C to $950 \mu\text{F}/\text{cm}^2$ at 394°C . This is consistent with values reported in the literature, which typically range from 60 to $550 \mu\text{F}/\text{cm}^2$ and occasionally higher.^{25,26,59,71} The literature values do not show a clear temperature dependence. As noted earlier, these values likely represent an electrochemical pseudocapacitance rather than a true double layer capacitance. The value of C_{DL} for the GDC specimens varied from 80 to $325 \mu\text{F}/\text{cm}^2$ with no clear dependence on temperature, which also seems reasonable in light of the YSZ results.

The last of the four fitting parameters is the permittivity ϵ , which would intuitively be expected to represent the permittivity of the electrolyte film. However, the substrate permittivity was found to be far more significant to the overall impedance spectrum since the substrate thickness is so much larger than that of the electrolyte. In fact, a sensitivity study revealed that the impedance magnitude is more sensitive to the substrate permittivity than to that of the electrolyte unless the electrolyte is roughly the same thickness as the substrate or larger. As this was not the case in the present samples, the substrate permittivity rather than the electrolyte permittivity was chosen as the fitting parameter, and the electrolyte permittivity was assigned a constant value of 10 for all of the fitting. Adjusting this value within a reasonable range had very little observable effect on the results.

For the YSZ specimens, ϵ varied from 8.3 to 8.8 and decreased slightly with increasing temperature. This is more than twice as large as the value of $\epsilon \approx 3.8$ reported in the literature for fused silica,¹²⁹ but still of a reasonable order of

magnitude. The permittivity of the GDC specimens also generally decreased with increasing temperature. The values varied from 12.5 at 652°C to 24.6 at 447°C (the permittivity at 401°C was slightly lower at 23.1). For comparison, the expected permittivity of sapphire^{130,131} varies from 8.9–11.6 depending on the crystal orientation. However, the sensitivity of the impedance to permittivity is quite low relative to the resolution of the fitting technique. Therefore, it appears that neither the film nor the substrate permittivity can be precisely determined using this technique. Stray capacitances in the experimental setup may be yielding anomalously high values in the model.

One question raised by the fitting results concerns the apparent lack of current constriction at the TPB. The model assumes no constriction of current across the electrode-electrolyte interface to the region near the TPB, even though this is the expected behavior for dense platinum electrodes. Nonetheless the model accurately fits the experimental results with realistic values of all fitting parameters. In fact, given that the intermediate frequency impedance arc predicted by the model arises from current spreading at low frequencies, it is unlikely the same effect would be observed if the current were instead constricted at low frequencies. Hertz et al.²⁰ have already shown that the intermediate frequency feature cannot plausibly arise from current constriction. This necessitates some possible explanations for the apparent success of the model in fitting the dense electrode impedance spectra.

First, it is possible that the dense electrodes studied were more porous than previously thought, though they were inspected by scanning electron microscopy and no holes were observed. Since it is unlikely that a significant number of pores would have escaped detection, this does not seem highly plausible. Another possibility, of

course, is that the intermediate frequency feature does not arise from current spreading and in fact is due to some other mechanism. However, the excellent fit of the experimental data lends credence to the model. Current spreading as the intermediate frequency impedance mechanism also explains why this impedance feature has only been observed in cells with coplanar electrode construction, since it is this geometry that leads to current spreading. Also, the effect was observed in two different electrochemical systems (Pt/YSZ and Pt/GDC), which may not have identical electrochemical behavior. This also makes a geometry-related mechanism for the impedance feature seem likely.

A third, more likely explanation for the apparent lack of current constriction may be that the physical width of the TPB (usually assumed to be on the order of nanometers) is actually considerably larger—enough to allow significant current spreading. As discussed in Section 1.1.4.1, there have been very few studies of this important parameter, but one result reported by Opitz et al.^{21,22} put the TPB size at approximately 1 μm in the vicinity of 300°C and it is possible it could be even larger at higher temperature. This could allow for a large enough area of three-phase contact to produce significant current spreading, especially if occasional pores or pinholes are also present. Therefore, this hypothesis remains a distinct possibility and more research will be required to validate or invalidate it. With this in mind, caution should be exercised when applying the model discussed here to future experiments with dense electrodes, though it is expected to be applicable to porous electrodes without reservation.

4.2.2 Validity of Eq. 67

All of the results thus far have demonstrated that so long as (69) is satisfied, the resistance of the intermediate frequency arc correlates closely with (67). The form of (67) seems intuitive as it resembles the theoretical resistance of the portion of the electrolyte under the electrode (region *ABEF* in Figure 13). However, the constant factor of $1/3$ (hereafter denoted K) that appears in the expression is more difficult to interpret, and it is still unclear if the value of K depends on the sample geometry. This was investigated more thoroughly using a DC model of the electrolyte geometry with a uniform current distribution at the electrode-electrolyte interface (corresponding to the case where $S \rightarrow \infty$). The value of K was computed for different electrolyte aspect ratios and electrode finger geometries, as shown in Figure 60. As can be seen, K is approximately equal to $1/3$ when the geometric ratio h / L_{ode} is less than about 0.2 (i.e. the electrode finger width is more than 5 times the electrolyte thickness). For larger values of h / L_{ode} , the value of K increases dramatically. This result seems unintuitive at first glance as it implies that the expected inverse proportionality between resistance and h / L_{ode} breaks down for thick electrolytes. However, the geometry of the electrodes necessitates a majority of the current remaining near the electrolyte surface, so increasing the electrolyte thickness above a certain value will have a negligible effect on the resistance. Fortunately for the experimenter, many practical thin film devices have $h / L_{ode} < 0.2$, so (67) is expected to remain broadly applicable.

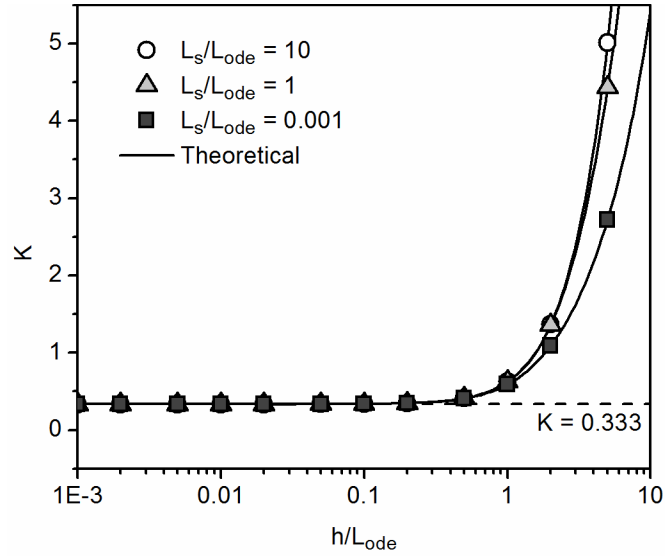


Figure 60. Resistance scaling factor K as a function of aspect ratio h / L_{ode} for the case where $R_{ode} \gg R_{yte}$. Results are shown for three different values of the electrode spacing ratio L_s / L_{ode} . Also shown are plots of the same quantity calculated using (72) and (73). The value $K = 1/3$ is indicated by a dashed line.

Thus far, (69) has been repeatedly asserted as a necessary condition for the validity of approximation (67), but there has been little quantitative justification. This is clarified in Figure 61, which plots the relative error in R_2 calculated using (67) compared to the observed intermediate frequency resistance against the dimensionless quantity S for all samples considered in the previous sections. According to (69), this error should be negligible when $S \gg 1$. This is indeed confirmed by the figure, and it is evident that $S \geq 10$ is sufficiently large to achieve an excellent estimate. Even when $S = 1$, (67) gives an error of only about 5%.

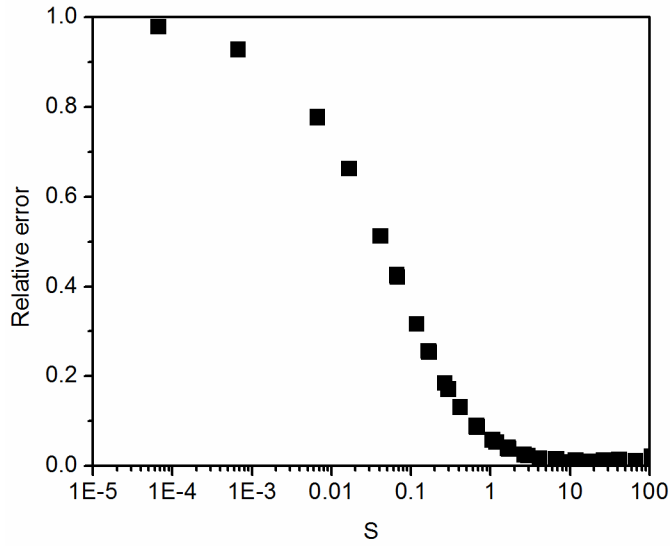


Figure 61. Percent error in intermediate frequency resistance (R_2) estimate calculated using (67) as a function of the dimensionless number S .

It has been established that the intermediate frequency resistance R_2 can be estimated accurately from the semi-empirical expression (67) in almost any situation where the condition $S \geq 10$ is met. Additionally, it has been observed that R_2 tends to zero when $R_{yte} \gg R_{ode}$. However, calculating R_2 in the intermediate regime where R_{yte} is the same order or slightly larger than R_{ode} is less straightforward. The DC resistance of geometries similar to Figure 13 was previously studied analytically by Zhang et al.⁵⁷ From this work, the expected theoretical spreading resistance may be derived as

$$R_{spread,theo} = \frac{\bar{R}_C}{2\pi w \sigma} \quad (72)$$

where \bar{R}_C is a function of the relative conductivities of the electrode and electrolyte as well as the geometric parameters. The analytical expression for \bar{R}_C is unwieldy, but in the limit of $R_{ode} / R_{yte} \rightarrow \infty$ it may be simplified as

$$\bar{R}_C = 4 \sum_{n=1}^{\infty} \frac{\coth[(n-1/2)\pi h / L_{yte}] \sin^2[(n-1/2)\pi L_{ode} / L_{yte}]}{(n-1/2)^3 (\pi L_{ode} / L_{yte})^2} - \frac{2\pi(L_{yte} - L_{ode})}{h} \quad (73)$$

Thus if (69) is satisfied, it is expected that the theoretical value of R_2 can be calculated using (72) and (73). This result bears little resemblance to the expression (67) which was deduced from the parametric study, but the two expressions do in fact yield nearly identical results in the range of parameter values of interest. Values of the scaling factor K calculated from (72), shown as solid lines in Figure 61, agree closely with the results of the DC modeling. Thus when $S \geq 10$ and $L_{ode} > 5h$, R_2 can be estimated to a high degree of accuracy using (67). Unfortunately a general closed-form expression for K could not be determined, so very thick films with $L_{ode} < 5h$ require the use of (72) to calculate R_2 . When the condition $S \gg 1$ is satisfied, \bar{R}_C can be calculated from (73); otherwise, the general expression given in Appendix A of Reference 57 must be used.

4.2.3 Comparison to Equivalent Circuit Models

With the physical meaning of the intermediate frequency impedance now better understood, the question arises of whether, for experimental fitting purposes, it might be simpler to replace the relatively complex model described here with a simpler equivalent circuit model. In order to investigate further, equivalent circuit fitting of the spectra shown in Figure 29 was performed using ZView (SAI, v.3.2d). The fitting used the equivalent circuit shown in Figure 11, whose adjustable parameters include the three resistance values R_1 , R_2 , and R_3 corresponding to the high, intermediate, and low frequency arcs, respectively. In order for the equivalent circuit model to be useful, these values should correspond to physically meaningful properties of the electrochemical cell. For $h = 25$ nm, the equivalent circuit fit yields a

value of $R_3 = 3.31 \text{ M}\Omega$ corresponding to the low frequency arc. Using (65) it is possible to calculate $J_0 = 0.101 \text{ }\mu\text{A}/\text{cm}^2$, an error of approximately 1% from the actual value of $0.1 \text{ }\mu\text{A}/\text{cm}^2$. The other two resistances obtained from the equivalent circuit, $R_1 = 505 \text{ k}\Omega$ and $R_2 = 179 \text{ k}\Omega$, can be used to independently quantify σ using (63) and (67) respectively. From R_1 a value of $\sigma = 0.990 \text{ mS}/\text{m}$ is obtained, an error of less than 1% from the true value, $1 \text{ mS}/\text{m}$. Calculating the conductivity from R_2 instead yields $\sigma = 0.932 \text{ mS}/\text{m}$, which is an error of approximately 7%. Since (67) is an empirical, approximate relation, it is unsurprising that it gives a less accurate value of σ . Nonetheless, the equivalent circuit in this case is demonstrably useful in quantifying the system parameters, given the equations derived in this work to explain the physical meaning of the elements.

On the other hand, it was noted earlier that impedance spectra for very thin electrolytes could yield misleading results when fitted with an equivalent circuit, as the intermediate frequency arc becomes large enough to alter the apparent magnitude of the electrode arc. For $h = 1 \text{ nm}$, the equivalent circuit gives $R_3 = 4.79 \text{ M}\Omega$, which is clearly problematic since with only the electrolyte thickness having changed, the electrode resistance is expected to be the same as in the previous case. Calculating the exchange current density yields $J_0 = 0.070 \text{ }\mu\text{A}/\text{cm}^2$, which differs from the actual value by 30%. This overestimation of electrode polarization resistance reveals a notable deficiency of an equivalent circuit model as applied to thin film geometries, and caution should be exercised when applying such models generally.

4.3 Diffusion-Reaction Model

In Section 3.3, a model of the thin-film electrode based on diffusion-reaction equations was demonstrated and parametric studies were performed on the reaction

rate constants, diffusivity, and geometric parameters. Here, the usefulness of the model will be enhanced by taking a first step toward validating the results, and some questions raised by the previous sections will be explored in greater detail.

4.3.1 Comparison Between Models

As previously discussed, the computational power available for the present study was not sufficient to enable direct fitting of experimental results using the diffusion-reaction microelectrode model (referred to throughout the remainder of this section as model C). The electrode finger geometry used in the model was limited to a considerably smaller size scale than what would be practically realizable using conventional fabrication techniques. This makes direct validation of the model difficult. However, it is possible to model the same electrode geometry using the simpler electrode model which was presented in Section 2.3 and experimentally validated in Section 4.2.1, referred to as model B throughout the remainder of this section. Figure 62 shows a simulated impedance spectrum generated using model C, reproduced from Figure 36. As noted in that section, the reaction rate constants for this simulation were $k_{-1}^0 = 10 \text{ m}^3/\text{mol}\cdot\text{s}$ and $k_2^0 = 4.1 \times 10^{-7} \text{ mol}\cdot\text{s}/(\text{kg}\cdot\text{m}^2)$. For comparison, the figure also shows the best-fit impedance spectrum generated using model B.

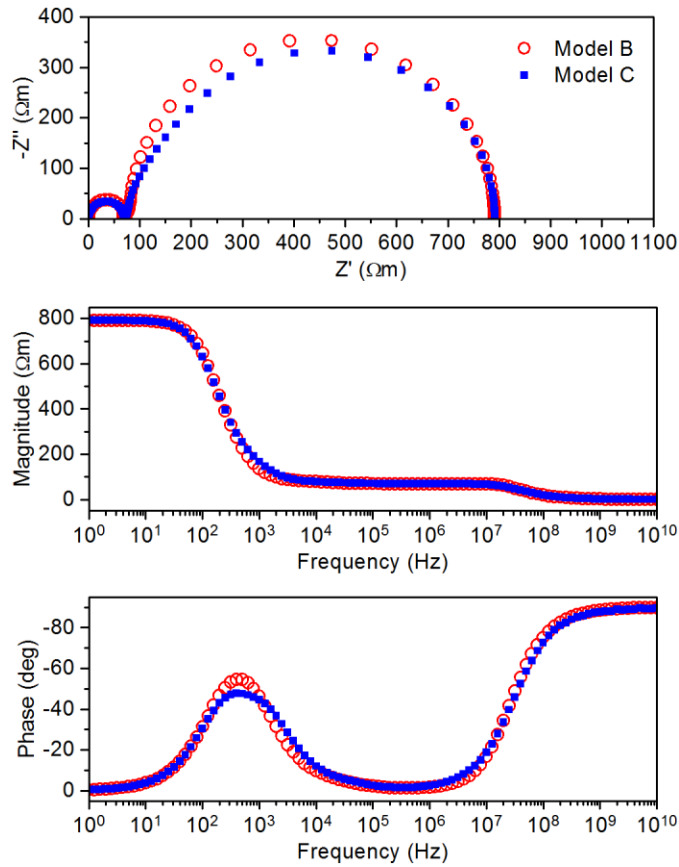


Figure 62. Simulated impedance spectrum generated using model C with $k_{-1}^0 = 10 \text{ m}^3/\text{mol}\cdot\text{s}$ and $k_2^0 = 4.1 \times 10^{-7} \text{ mol}\cdot\text{s}/(\text{kg}\cdot\text{m}^2)$ compared to spectrum generated using model B with $\sigma = 4.3 \times 10^{-4} \text{ S/cm}$, $\varepsilon = 37$, $C_{DL} = 6400 \text{ }\mu\text{F/cm}^2$, and $J_0 = 236 \text{ mA/cm}^2$.

As can be observed from the figure, the qualitative agreement between the two models is quite good. The conductivity determined from the fitting with model B is $4.3 \times 10^{-4} \text{ S/cm}$, which is within 35% of the conductivity specified in the formulation of model C. The permittivity obtained from the fitting was 37, which is within 50% of the specified permittivity of 25 (the fitting was not particularly sensitive to

permittivity). The other two fitting parameters, the exchange current density and double layer capacitance, are both considerably higher than reported literature values (see Section 4.2.1). This indicates that the arbitrarily chosen values of k_{-1}^0 and k_2^0 are not realistic for Pt/YSZ cells. Nevertheless, the qualitative agreement between the models is quite good and indicates that model C will be able to fit experimental data successfully given increased computational power. This will make it possible to extract more physically meaningful parameter values from the model than is possible with model B.

4.3.2 TPB Size

One geometric parameter of the diffusion-reaction model which has not yet been investigated, yet holds considerable interest, is the physical extent of the triple phase boundary. As shown in Figure 17, the present model formulation has the TPB defined as a square region with side length h_{act} , which is equal to the thickness of the surface layer ABD and the interfacial layer CD. In the studies discussed in Section 3.2.2, h_{act} was set at 1 nm. For the purposes of the present study, the question of how to model the TPB extension is non-trivial. One approach is to maintain the single-parameter approach already incorporated in the model and simply vary h_{act} . That is, the TPB remains square in cross section while its thickness, and consequently the thickness of the surface and interfacial layers, is varied accordingly. This approach is illustrated schematically in Figure 63a. Formulating the TPB extension in this manner is consistent with the existing model's interpretation of the interfacial layer as a region of two-phase coexistence, and also has the advantage of not requiring any additional parameters.

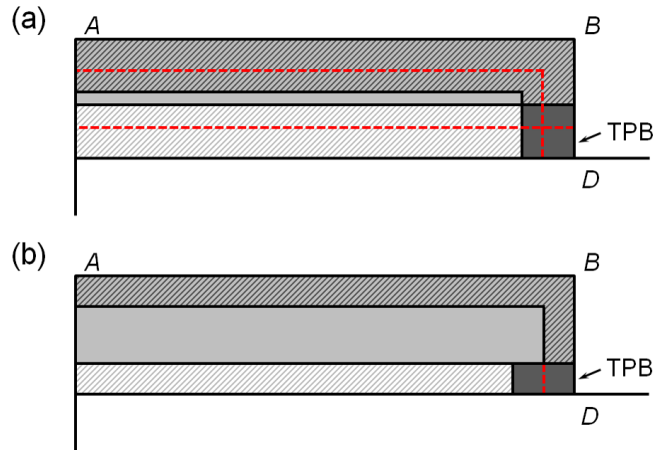


Figure 63. Two different formulations of the TPB extension: (a) single-parameter and (b) two-parameter.

In order to investigate the effect of varying the TPB size in this manner, the electrode geometry was slightly modified to make the finger cross section square. That is, sides AB and AC in Figure 17 both have a length of 25 nm. This allows the TPB size to be increased up to a maximum dimension of $h_{act} = L_{ode} / 2$ without compromising the model geometry. Figure 64 shows impedance spectra corresponding to three such specimens with different values of h_{act} . As the plot illustrates, the reduction of the TPB size primarily manifests as an increase of the apparent electrode resistance, indicating that efforts to estimate the TPB size from impedance measurements are not likely to be fruitful. However, for very small TPB sizes, an intermediate frequency arc appears in the spectrum. In order to make the effect more apparent, the intermediate frequency region of the plot has been magnified in the inset. The intermediate frequency arc is barely apparent when $h_{act} = 1$ nm, but quite pronounced when $h_{act} = 0.1$ nm. This is consistent with the findings of Hertz et al.²⁰ that current constriction cannot cause an intermediate frequency arc at a magnitude

sufficient to explain the intermediate frequency features observed experimentally when $h_{act} \geq 1$ nm.

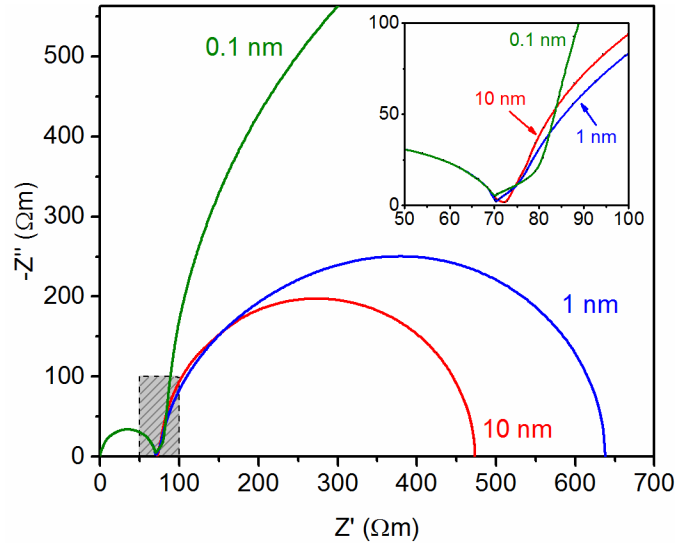


Figure 64. Simulated impedance spectra for $k_{-1}^0 = 10 \text{ m}^3/\text{mol}\cdot\text{s}$, $k_2^0 = 4.1 \times 10^{-7} \text{ mol}\cdot\text{s}/(\text{kg}\cdot\text{m}^2)$, and three different values of the TPB size h_{act} as indicated. The TPB geometry has been defined as shown in Figure 63a. The shaded portion of the spectrum is enlarged in the inset to clarify the intermediate frequency behavior.

Fleig et al.¹³² gave an analytical estimate for the constriction resistance when $h_{yte} < L_{yte} - L_{ode}$, which is valid for the present case:

$$R_{const} \approx \frac{2}{\pi\sigma} \ln\left(\frac{h_{yte}}{h_{act}}\right) \quad (74)$$

This equation predicts a constriction resistance of 34.2 Ωm for a TPB size of 1 nm and 68.2 Ωm for a TPB size of 0.1 nm. For comparison, the resistance of the intermediate frequency arc seen in Figure 64 was measured in ZView by fitting the equivalent circuit shown in Figure 11. For the TPB size of 0.1 nm, the equivalent circuit fit gave

a resistance of $69.3 \Omega\text{m}$ for the intermediate frequency arc, a difference of only 1.6% from the estimated constriction resistance. This confirms that the intermediate frequency arc is indeed caused by current constriction. (The intermediate frequency arc for specimens with $h_{act} > 0.1 \text{ nm}$ was too small to be measured accurately using the equivalent circuit.) Since 1 nm is not much larger than a single YSZ unit cell, it remains doubtful that a noticeable current constriction arc could occur in a real specimen.

It is evident from Figure 64 that varying the TPB size affects not only the intermediate frequency arc but also the low frequency arc. This is to be expected based on the model formulation, since increasing h_{act} makes more TPB volume available for the charge transfer reaction and also increases the surface layer volume for oxygen adsorption. Therefore, the reaction rates increase and the electrode resistance is reduced. Unfortunately, it is not possible to completely separate these effects from those occurring due to current constriction. However, the matter can be somewhat simplified by adopting a different formulation of the TPB extension, shown in Figure 63b. In this case, the thickness of the surface and interfacial layers is held fixed at 1 nm, and only the width of the TPB is varied. This adds another geometric parameter to the model, but makes it possible to at least minimize the influence of the adsorption reaction since the surface layer volume does not change. It is also consistent with the conventional understanding of the TPB active area as an extension along the electrode-electrolyte interface. Impedance spectra for three different values of the TPB size for such a geometry are shown in Figure 65. In this case, the charge transfer rate constant has been reduced to $1 \text{ m}^3/\text{mol}\cdot\text{s}$ in order to prevent issues with the total

charge transfer rate being too large when the TPB size is increased (see Section 3.3.2.1).

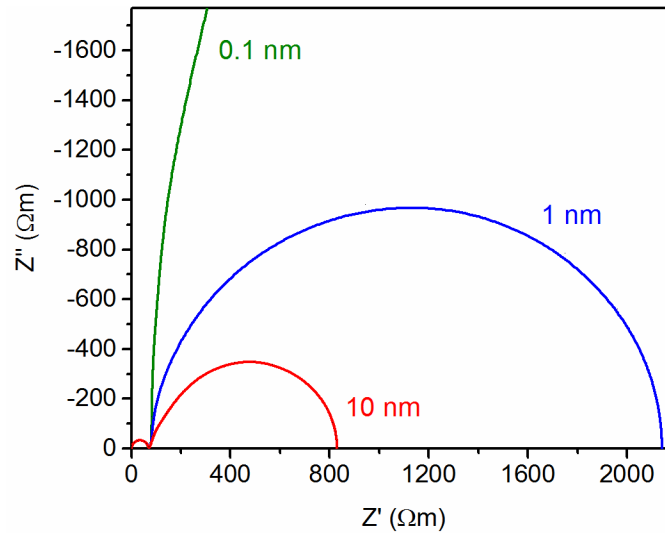


Figure 65. Simulated impedance spectra for $k_{-1}^0 = 1 \text{ m}^3/\text{mol}\cdot\text{s}$, $k_2^0 = 4.1 \times 10^{-7} \text{ mol}\cdot\text{s}/(\text{kg}\cdot\text{m}^2)$, and three different values of the TPB size h_{act} as indicated. The TPB geometry has been defined as shown in Figure 63b.

The figure shows large differences between the electrode resistances for the three cases. This is unsurprising given that increasing the TPB size also increases the total charge transfer rate. In fact, it may be more informative to vary the TPB size accompanied by a corresponding change of the charge transfer rate constant. That is, if the TPB size is increased by an order of magnitude, k_{-1}^0 should be decreased by an order of magnitude to keep the total charge transfer rate approximately the same. The 10 nm specimen shown in the figure has an electrode resistance of 760 Ωm . For comparison, if the TPB size is decreased to 1 nm and k_{-1}^0 increased to $10 \text{ m}^3/\text{mol}\cdot\text{s}$, the resistance decreases by 5% to 721 Ωm . This demonstrates that the change of TPB size

almost entirely manifests as a change of the overall charge transfer rate. The 5% decrease of resistance is probably due to more complete utilization of the active region for smaller TPB sizes. This result demonstrates the difficulty of determining the TPB size via experimental fitting with this type of model since the influence of the TPB size cannot be easily separated from the reaction rate constants.

4.3.3 Rate Constants

Parametric studies of the adsorption and charge transfer reaction rate constants were discussed in Section 3.3.2.1. Now the relative influence of these parameters will be examined in greater detail in order to determine which process dominates in various cases, and the prospects for quantifying both parameters via experimental fitting will be discussed. The resistances due to adsorption and charge transfer were separated using a procedure similar to that of Section 3.2.2. For a given combination of k_{-1}^0 , the charge transfer coefficient, and k_2^0 , the adsorption coefficient, the resistance R_1 due to charge transfer was determined by first increasing k_2^0 to a sufficiently large value that the resistance due to adsorption becomes negligible. The resistance due to charge transfer could then be determined by subtracting the electrolyte resistance from the total resistance with very large k_2^0 . Then, for a given value of k_2^0 , the resistance R_2 due to adsorption is given by

$$R_2 = R_{total} - R_{yte} - R_1 \quad (75)$$

This allows the relative effect of different combinations of k_{-1}^0 and k_2^0 to be investigated. As noted in Section 3.3.2.1, unexpected inductive effects and looping of the impedance spectrum were observed when $k_{-1}^0 \geq 100 \text{ m}^3/\text{mol}\cdot\text{s}$, so the above procedure was only considered meaningful for $k_{-1}^0 \leq 10 \text{ m}^3/\text{mol}\cdot\text{s}$.

The resistance ratio R_2 / R_1 for various values of the rate constants is shown in Figure 66. The region where R_1 and R_2 are within an order of magnitude of each other is indicated by the shaded region in the figure; this can be considered the approximate range of parameter values where the electrode reaction rate is jointly controlled by adsorption and charge transfer. It can be observed from the figure that this occurs when k_2^0 is approximately 7–8 orders of magnitude smaller than k_{-1}^0 .

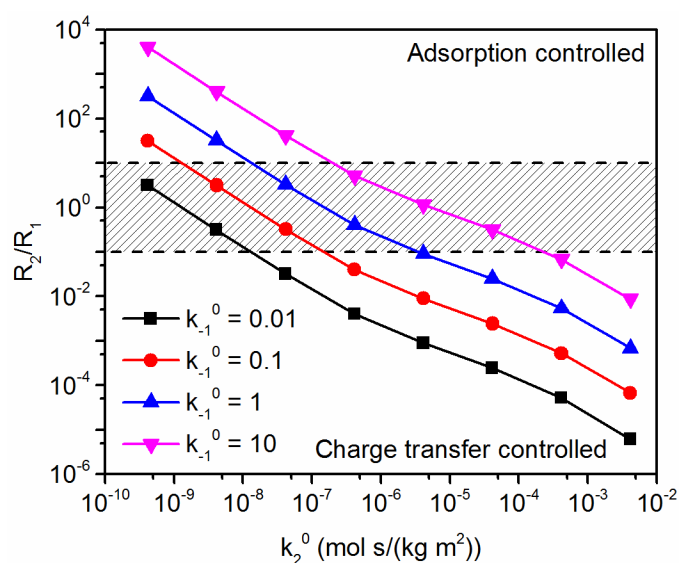


Figure 66. The resistance ratio R_2 / R_1 vs. k_2^0 for the indicated values of k_{-1}^0 , in $\text{m}^3/\text{mol}\cdot\text{s}$. The reaction can be considered to be jointly limited by adsorption/diffusion and charge transfer within the region indicated by dashed lines.

Although these results clarify the relative parameter magnitudes for which adsorption/diffusion and charge transfer contribute to the overall impedance, there is no clear way to deconvolute these contributions based on the impedance spectrum

alone. That is, an impedance spectrum for a specimen with rapid adsorption and slow charge transfer may appear identical to that of a specimen with slow adsorption and rapid charge transfer. However, if the adsorption rate can be quantified independently by experiment, then the charge transfer rate can be determined by fitting experimental impedance spectra with k_2^0 as the sole fitting parameter for the electrode impedance. Oxygen adsorption kinetics on a Pt(111) surface were studied by Bonzel et al.¹¹² using a CO titration technique, which enabled them to quantify the sticking coefficient (and thus k_2^0) as a function of oxygen coverage and temperature. (The evident coverage dependence of k_2^0 was not considered an issue in the present work since the coverage does not vary much along the electrode surface under low overpotential.) With the equilibrium oxygen coverage of 0.35 assumed in the model, a rate constant of $k_2^0 \approx 3 \times 10^{-5} \text{ mol} \cdot \text{s} / (\text{kg} \cdot \text{m}^2)$ can be estimated from their work. Although their measurements were conducted at 270–330°C, lower than those encountered in SOFC operation, their work indicated that there was negligible temperature dependence within that range. Therefore, the estimate of k_2^0 above can be cautiously adopted at higher temperatures, although conducting more titration experiments at high temperature would be preferable. In either case, the ability to independently measure k_2^0 will allow fitting the model to experimental data in order to quantify the charge transfer coefficient, a result which has not been accomplished to date.

Chapter 5

CONCLUSIONS

5.1 Grain Boundary Heterogeneity Study

In the first part of the present work, two-dimensional, time-domain numerical modeling was used to investigate the impedance behavior of polycrystalline electrolytes with heterogeneous grain boundary properties. Heterogeneous distributions of conductivity only, permittivity only, and both conductivity and permittivity were considered. The quantitative utility of CPE-based equivalent circuit fitting in such cases was of particular interest. In conjunction with a simple hexagonal grain model, such fitting enabled the mean grain boundary conductivity of all samples to be estimated within 30%. The mean permittivity was also estimated using both a well-known equation from the literature and a new empirical equation, with maximum errors of 85% and 45%, respectively. Although the empirical equation offers better accuracy in recovering the mean permittivity or grain boundary thickness from the equivalent circuit parameters, more work is required to investigate its broader applicability.

The correlation between the equivalent circuit parameters and the spread of the conductivity and permittivity values was also investigated. A nearly linear relationship was observed between the CPE exponent n and the standard deviation of the conductivity distributions, albeit with considerable scatter for large grain sizes. Similarly, the metric chosen for the spread of the permittivity distributions was found

to have a near-linear correlation with n . Based on these results, if all other grain boundary parameters can be assumed uniform, the approximate range of values of the heterogeneous parameter can be quantified. However in the case of multiple heterogeneous parameters, the individual contributions cannot yet be deconvoluted.

5.2 Microelectrode Model

In this part of the work, the two-dimensional electrolyte impedance model was extended to incorporate a phenomenological description of the electrode-electrolyte interface via the Butler-Volmer equation. The model was able to fit complex experimental impedance spectra for Pt/YSZ and Pt/GDC cells using only four adjustable parameters. This represents a substantial improvement over comparable models based on equivalent circuits, which require up to nine fitting parameters. Further, the new model was shown to be able to quantify electrode parameters more accurately than an equivalent circuit in the case of very thin films. Comparison of the fitting parameter values to literature provided evidence of the validity of the model. However, due to the sample geometry, the ability to accurately measure the permittivity of thin film electrolytes has been shown to be limited. The lack of any apparent current constriction effect at the triple phase boundary may indicate that the electrochemically active area is larger than previously thought.

A parametric study using the new model enabled the mechanism of a previously unexplained intermediate frequency impedance arc to be understood. The arc arises from spreading of current at low frequencies due to the high resistance of the electrode-electrolyte interface. At higher frequencies, the impedance of the interface is reduced by the capacitive displacement currents, allowing a shorter current path through the electrolyte. This spreading effect cannot be adequately captured by a one-

dimensional model. The magnitude of the spreading resistance was quantified and matched the expected theoretical value. In addition, a much simpler estimate of the spreading resistance was shown to be valid in many cases.

5.3 Diffusion-Reaction Model

Finally, the model was extended using the Poisson-Nernst-Planck equations to model transport and reactions of charged species. This gave the model a physical basis consistent with literature reports of the Pt, O₂|YSZ interface. Although the computational power available for modeling was not sufficient to fit the experimental results discussed in the previous section, the model was partially validated by comparison to the phenomenological model. Parametric studies demonstrated that in most cases, charge transfer and adsorption/diffusion both contribute to the overall electrode impedance, though there are not always two distinct arcs corresponding to these respective processes. The total resistance was found to be inversely proportional to the charge transfer coefficient when adsorption was very fast relative to charge transfer, and inversely proportional to the adsorption rate constant when adsorption was relatively slow. Diffusion of adsorbed oxygen on the electrode surface was observed not to be rate limiting alone, but only in conjunction with adsorption since very rapid adsorption essentially bypasses the diffusion process. These results help to explain why efforts to reduce the electrode reaction to a single limiting process have been frustrating.

Parametric studies of the TPB size reinforced the observation that current constriction resistances are negligible when the active area is on the order of 1 nm or greater. Instead, changes of the TPB size primarily affect the apparent electrode resistance. This makes it impractical to measure the TPB size using the present

modeling approach. An upper limit on the charge transfer coefficient of $10 \text{ m}^3/\text{mol}\cdot\text{s}$ was noted based on non-physical model output due to violation of the model assumptions in the case of very fast charge transfer. Also, a maximum adsorption rate coefficient of $0.028 \text{ mol}\cdot\text{s}/(\text{kg}\cdot\text{m}^2)$ was noted, corresponding to a sticking coefficient of 1. Within these limits, the model is expected to remain valid provided extremes of overpotential or P_{O_2} are not encountered. In such cases, the model can be extended in a straightforward fashion.

5.4 Future Work

The work described here suggests a number of possible future projects. The most crucial step forward will be the scaling up of the diffusion-reaction model in order to fit the available experimental data, as was done in Section 4.2.1 using the phenomenological model. This will either allow the model to be validated and the unknown parameters to be quantified, or will highlight areas in which the model needs to be extended. In particular, the model may benefit from reexamining the surface diffusion model to consider interactions between adsorbed species. Even if not necessary to fit the experimentally obtained impedance spectra, this will give the model a wider range of validity with respect to atmospheric parameters, eliminate the anomalous behavior observed in Section 3.3.2.1, and give the researcher a more confident footing for modeling DC polarization in the nonlinear range. The model can also be extended in a straightforward manner to the low P_{O_2} regime by considering diffusion in the gas phase.

The two earlier studies also suggest additional work that could be beneficial. In the grain boundary heterogeneity study, the modeling assumed very broad distributions of grain boundary conductivity and permittivity. While this gives the

researcher an idea of the “worst case” situation, the variability of grain boundary properties in actual polycrystals has not been thoroughly studied. Fleig et al. have reported a procedure whereby the impedance of individual grain boundaries may be measured using microprobes,⁶³ which would allow such a study to be conducted. This would be of considerable interest in assessing the validity of brick layer models in the future. Additionally, the empirical effective capacitance equation (70) should be studied in greater detail to be sure of its range of applicability. In the case of the phenomenological electrode modeling study, further experimental studies using different materials and electrode geometries will help clarify the role of spreading resistance and provide more evidence of this mechanism.

REFERENCES

1. P. Knauth and H. L. Tuller, *J. Am. Ceram. Soc.*, **85**, 1654–1680 (2002).
2. J. Larminie and A. Dicks, *Fuel Cell Systems Explained*, 2nd ed., John Wiley & Sons, Chichester, (2003).
3. S. Pizzini, in *Fast Ion Transport in Solids: Solid State Batteries and Devices*, W. van Gool, Editor, p. 461–475, North-Holland, Amsterdam (1973).
4. S. B. Adler, *Chem. Rev.*, **104**, 4791–4843 (2004)
<http://www.ncbi.nlm.nih.gov/pubmed/15669169>.
5. A. Schmid, *Helv. Chim. Acta*, **7**, 370–373 (1924).
6. B. C. H. Steele, *Solid State Ionics*, **86–88**, 1223–1234 (1996).
7. J. Fleig, *Solid State Ionics*, **161**, 279–289 (2003)
<http://linkinghub.elsevier.com/retrieve/pii/S0167273803002170>.
8. A. Bieberle, L. P. Meier, and L. J. Gauckler, *J. Electrochem. Soc.*, **148**, A646–A656 (2001) <http://jes.ecsdl.org/cgi/doi/10.1149/1.1372219>.
9. R. Radhakrishnan, A. V. Virkar, and S. C. Singhal, *J. Electrochem. Soc.*, **152**, A210–A218 (2005) <http://jes.ecsdl.org/cgi/doi/10.1149/1.1829415>.
10. R. Radhakrishnan, A. V. Virkar, and S. C. Singhal, *J. Electrochem. Soc.*, **152**, A927–A936 (2005) <http://www.scopus.com/inward/record.url?eid=2-s2.0-20444427201&partnerID=tZOtx3y1>.
11. L. A. Dunyushkina, Y. Lu, and S. B. Adler, *J. Electrochem. Soc.*, **152**, A1668 (2005).
12. A. K. Opitz and J. Fleig, *Solid State Ionics*, **181**, 684–693 (2010)
<http://linkinghub.elsevier.com/retrieve/pii/S0167273810001359>.
13. J. L. Hertz and H. L. Tuller, *J. Electroceramics*, **13**, 663–668 (2004).
14. W. C. Heraeus, *Zeitschrift für Elektrochemie*, **6**, 41–43 (1899).

15. Y. Zheng, U. Sauter, and R. Moos, *J. Electrochem. Soc.*, **163**, F877–F884 (2016) <http://jes.ecsdl.org/lookup/doi/10.1149/2.1081608jes>.
16. A. K. Opitz, M. P. Hörlein, T. Huber, and J. Fleig, *J. Electrochem. Soc.*, **159**, B502–B513 (2012) <http://jes.ecsdl.org/cgi/doi/10.1149/2.044205jes>.
17. N. L. Robertson and J. N. Michaels, *J. Electrochem. Soc.*, **137**, 129–135 (1990) <http://jes.ecsdl.org/cgi/doi/10.1149/1.2086347>.
18. J. Fleig and J. Maier, *J. Electrochem. Soc.*, **144**, L302–L305 (1997) <http://jes.ecsdl.org/cgi/doi/10.1149/1.1838076>.
19. J. Fleig, *Zeitschrift für Phys. Chemie*, **221**, 1149–1159 (2007).
20. J. L. Hertz and H. L. Tuller, *Solid State Ionics*, **178**, 915–923 (2007) <http://linkinghub.elsevier.com/retrieve/pii/S0167273807001397>.
21. A. K. Opitz, A. Schintlmeister, H. Hutter, and J. Fleig, *ECS Trans.*, **25**, 2783–2792 (2009) <http://ecst.ecsdl.org/cgi/doi/10.1149/1.3205840>.
22. A. K. Opitz, A. Schintlmeister, H. Hutter, and J. Fleig, *Phys. Chem. Chem. Phys.*, **12**, 12734–12745 (2010) <http://www.ncbi.nlm.nih.gov/pubmed/20737090>.
23. D. Y. Wang and A. S. Nowick, *J. Electrochem. Soc.*, **126**, 1155–1165 (1979) <http://jes.ecsdl.org/content/126/7/1155.abstract>.
24. A. J. Bard and L. R. Faulkner, *Electrochemical Methods: Fundamentals and Applications*, John Wiley & Sons, New York, (1980).
25. J. E. E. Bauerle, *J. Phys. Chem. Solids*, **30**, 2657–2670 (1969).
26. M. J. Verkerk, M. W. J. Hammink, and A. J. Burggraaf, *J. Electrochem. Soc.*, **130**, 70–78 (1983).
27. M. J. Verkerk and A. J. Burggraaf, *J. Electrochem. Soc.*, **354**, 78–84 (1983).
28. J. Mizusaki, K. Amano, S. Yamauchi, and K. Fueki, *Solid State Ionics*, **22**, 313–322 (1987).
29. J. Mizusaki, K. Amano, S. Yamauchi, and K. Fueki, *Solid State Ionics*, **22**, 323–330 (1987) <http://www.sciencedirect.com/science/article/pii/0167273887901500>.
30. C. Schwandt and W. Weppner, *J. Electrochem. Soc.*, **144**, 3728–3738 (1997) <http://jes.ecsdl.org/cgi/doi/10.1149/1.1838083>.

31. A. Mitterdorfer and L. J. Gauckler, *Solid State Ionics*, **117**, 187–202 (1999).
32. A. Mitterdorfer and L. J. Gauckler, *Solid State Ionics*, **117**, 203–217 (1999).
33. A. Mitterdorfer and L. J. Gauckler, *Solid State Ionics*, **120**, 211–225 (1999).
34. A. K. Opitz et al., *Electrochim. Acta*, **56**, 9727–9740 (2011)
<http://www.pubmedcentral.nih.gov/articlerender.fcgi?artid=3209560&tool=pmcentrez&rendertype=abstract>.
35. E. Ahlgren and F. Willy Poulsen, *Solid State Ionics*, **70–71**, 528–532 (1994).
36. J. R. MacDonald, Ed., *Impedance Spectroscopy: Emphasizing Solid Materials and Systems*, John Wiley & Sons, New York, (1987).
37. J. T. S. Irvine, D. C. Sinclair, and A. R. West, *Adv. Mater.*, **2**, 132–138 (1990)
<http://doi.wiley.com/10.1002/adma.19900020304>.
38. J. Jamnik and J. Maier, *Phys. Chem. Chem. Phys.*, **3**, 1668–1678 (2001)
<http://xlink.rsc.org/?DOI=b100180i>.
39. D. A. Harrington and P. van den Driessche, *Electrochim. Acta*, **56**, 8005–8013 (2011) <http://linkinghub.elsevier.com/retrieve/pii/S0013468611001289>.
40. W. G. Bessler, *Solid State Ionics*, **176**, 997–1011 (2005)
<http://linkinghub.elsevier.com/retrieve/pii/S0167273805000135>.
41. J. Fleig and J. Maier, *J. Eur. Ceram. Soc.*, **19**, 693–696 (1999)
<http://linkinghub.elsevier.com/retrieve/pii/S0955221998002982>.
42. T. van Dijk and A. J. Burggraaf, *Phys. Status Solidi*, **229**, 229–240 (1981)
<http://onlinelibrary.wiley.com/doi/10.1002/pssa.2210630131/abstract%5Cnpapers2://publication/uuid/668F3C84-4687-4F32-B9F2-6150D777F3B9>.
43. M. J. Verkerk, B. J. Middelhuis, and A. J. Burggraaf, *Solid State Ionics*, **6**, 159–170 (1982).
44. G. J. Brug, A. L. G. van den Eeden, M. Sluyters-Rehbach, and J. H. Sluyters, *J. Electroanal. Chem.*, **176**, 275–295 (1984).
45. B. Hirschorn et al., *Electrochim. Acta*, **55**, 6218–6227 (2010)
<http://linkinghub.elsevier.com/retrieve/pii/S0013468609013413>.
46. J. Fleig, *Solid State Ionics*, **150**, 181–193 (2002)
<http://linkinghub.elsevier.com/retrieve/pii/S0167273802002746>.

47. H. Duncan and A. Lasia, *Solid State Ionics*, **176**, 1429–1437 (2005).
48. D. Czekaj, A. Lisińska-Czekaj, T. Orkisz, J. Orkisz, and G. Smalarz, *J. Eur. Ceram. Soc.*, **30**, 465–470 (2010).
49. J. Fleig and J. Maier, *J. Electrochem. Soc.*, **145**, 2081–2089 (1998)
<http://jes.ecsdl.org/cgi/doi/10.1149/1.1838600>.
50. J. Fleig, P. Pham, P. Sztulzaft, and J. Maier, *Solid State Ionics*, **113–115**, 739–747 (1998).
51. J. Fleig, *Solid State Ionics*, **131**, 117–127 (2000)
<http://linkinghub.elsevier.com/retrieve/pii/S0167273800006275>.
52. J. Fleig, *J. Electroceramics*, **13**, 637–644 (2004)
<http://www.springerlink.com/index/10.1007/s10832-004-5170-3>.
53. J. Fleig and J. Maier, *J. Am. Ceram. Soc.*, **82**, 3485–3493 (1999).
54. J. Fleig and J. Maier, *Solid State Ionics*, **85**, 17–24 (1996)
<http://www.sciencedirect.com/science/article/pii/S0167273896000367>.
55. J. Jiang, W. Shen, and J. L. Hertz, *Solid State Ionics*, **249–250**, 139–143 (2013)
<http://dx.doi.org/10.1016/j.ssi.2013.08.003>.
56. R. S. Timsit, *IEEE Trans. Components Packag. Technol.*, **33**, 636–642 (2010)
<http://ieeexplore.ieee.org/lpdocs/epic03/wrapper.htm?arnumber=5575402>.
57. P. Zhang, Y. Y. Lau, and R. M. Gilgenbach, *J. Appl. Phys.*, **109** (2011).
58. L. R. Velho and R. W. Bartlett, *Metall. Trans.*, **3**, 65–72 (1972).
59. A. Jaccoud, C. Falgairrette, G. Fóti, and C. Comninellis, *Electrochim. Acta*, **52**, 7927–7935 (2007) <http://linkinghub.elsevier.com/retrieve/pii/S0013468607008249>.
60. R. Schmiedl et al., *Appl. Phys. A Mater. Sci. Process.*, **62**, 223–230 (1996)
<http://www.springerlink.com/openurl.asp?genre=article&id=doi:10.1007/s003390050289>.
61. J. Fleig and J. Maier, *Phys. Chem. Chem. Phys.*, **1**, 3315–3320 (1999)
<http://xlink.rsc.org/?DOI=a902839k>.
62. J. Fleig, S. Rodewald, and J. Maier, *Solid State Ionics*, **136–137**, 905–911 (2000).
63. J. Fleig, S. Rodewald, and J. Maier, *J. Appl. Phys.*, **87**, 2372–2381 (2000)

<http://link.aip.org/link/JAPIAU/v87/i5/p2372/s1&Agg=doi>.

64. N. J. Kidner, Z. J. Homrighaus, B. J. Ingram, T. O. Mason, and E. J. Garboczi, *J. Electroceramics*, **14**, 283–291 (2005).

65. N. J. Kidner, Z. J. Homrighaus, B. J. Ingram, T. O. Mason, and E. J. Garboczi, *J. Electroceramics*, **14**, 293–301 (2005).

66. N. J. Kidner, N. H. Perry, T. O. Mason, and E. J. Garboczi, *J. Am. Ceram. Soc.*, **91**, 1733–1746 (2008).

67. J. S. Dean, J. H. Harding, and D. C. Sinclair, I. Tanaka, Editor. *J. Am. Ceram. Soc.*, **97**, 885–891 (2014) <http://doi.wiley.com/10.1111/jace.12750>.

68. P. Fabry and M. Kleitz, *Electroanal. Chem. Interfacial Electrochem.*, **57**, 165–177 (1974).

69. D. Y. Wang and A. S. Nowick, *J. Electrochem. Soc.*, **704**, 55–63 (1981) <http://jes.ecsdl.org/cgi/doi/10.1149/1.2127387>.

70. H. Okamoto, G. Kawamura, and T. Kudo, *Electrochim. Acta*, **28**, 379–382 (1983).

71. A. J. A. Winnubst, A. H. A. Scharenborg, and A. J. Burggraaf, *Solid State Ionics*, **14**, 319–327 (1984).

72. J. Fleig and J. Maier, *Electrochim. Acta*, **41**, 1003–1009 (1996) <http://linkinghub.elsevier.com/retrieve/pii/0013468695004319>.

73. J. Fleig and J. Maier, *J. Electroceramics*, **1**, 73–89 (1997) <http://link.springer.com/article/10.1023/A:1009902532596>.

74. J. Fleig and J. Maier, *Solid State Ionics*, **94**, 199–207 (1997).

75. S. B. Adler, J. A. Lane, and B. C. H. Steele, *J. Electrochem. Soc.*, **143**, 3554–3564 (1996) <http://jes.ecsdl.org/cgi/doi/10.1149/1.1837252>.

76. A. M. Svensson, S. Sunde, and K. Nişancioğlu, *J. Electrochem. Soc.*, **144**, 2719–2732 (1997) <http://jes.ecsdl.org/cgi/doi/10.1149/1.1837887>.

77. P. Costamagna, P. Costa, and V. Antonucci, *Electrochim. Acta*, **43**, 375–394 (1998) <http://linkinghub.elsevier.com/retrieve/pii/S0013468697000637>.

78. S. H. Chan, K. A. Khor, and Z. T. Xia, *J. Power Sources*, **93**, 130–140 (2001) <http://linkinghub.elsevier.com/retrieve/pii/S0378775300005565>.

79. B. Kenney and K. Karan, *J. Electrochem. Soc.*, **157**, B1126–B1137 (2010) <http://jes.ecsdl.org/cgi/doi/10.1149/1.3432410>.
80. S. H. Chan and Z. T. Xia, *J. Electrochem. Soc.*, **148**, A388–A394 (2001) <http://jes.ecsdl.org/cgi/doi/10.1149/1.1357174>.
81. S. H. Chan, X. J. Chen, and K. A. Khor, *J. Electrochem. Soc.*, **151**, A164–A172 (2004) <http://jes.ecsdl.org/cgi/doi/10.1149/1.1630036>.
82. X. J. Chen, S. H. Chan, and K. A. Khor, *Electrochim. Acta*, **49**, 1851–1861 (2004) <http://linkinghub.elsevier.com/retrieve/pii/S001346860301034X>.
83. S. R. Pakalapati, I. Celik, H. O. Finklea, M. Gong, and X. Liu, *ECS Trans.*, **35**, 963–976 (2011) <http://ecst.ecsdl.org/cgi/doi/10.1149/1.3570077>.
84. Q.-A. Huang, R. Hui, B. Wang, and J. Zhang, *Electrochim. Acta*, **52**, 8144–8164 (2007) <http://linkinghub.elsevier.com/retrieve/pii/S0013468607007505>.
85. A. Bieberle and L. J. Gauckler, *Solid State Ionics*, **146**, 23–41 (2002).
86. W. G. Bessler, S. Gewies, and M. Vogler, *Electrochim. Acta*, **53**, 1782–1800 (2007) <http://linkinghub.elsevier.com/retrieve/pii/S0013468607010353>.
87. W. G. Bessler, S. Gewies, and M. Vogler, *ECS Trans.*, **7**, 1801–1810 (2007) <http://ecst.ecsdl.org/cgi/doi/10.1149/1.2729292>.
88. S. Gewies, W. G. Bessler, V. Sonn, and E. Ivers-Tiffée, *ECS Trans.*, **7**, 1573–1582 (2007) <http://ecst.ecsdl.org/cgi/doi/10.1149/1.2729264>.
89. S. Gewies and W. G. Bessler, *J. Electrochem. Soc.*, **155**, B937–B952 (2008) <http://jes.ecsdl.org/cgi/doi/10.1149/1.2943411>.
90. M. Vogler, A. Bieberle-Hütter, L. Gauckler, J. Warnatz, and W. G. Bessler, *J. Electrochem. Soc.*, **156**, B663–B672 (2009) <http://jes.ecsdl.org/cgi/doi/10.1149/1.3095477>.
91. D. G. Goodwin, H. Zhu, A. M. Colclasure, and R. J. Kee, *J. Electrochem. Soc.*, **156**, B1004–B1021 (2009) <http://jes.ecsdl.org/cgi/doi/10.1149/1.3148331>.
92. H. Zhu, R. J. Kee, V. M. Janardhanan, O. Deutschmann, and D. G. Goodwin, *J. Electrochem. Soc.*, **152**, A2427–A2440 (2005) <http://jes.ecsdl.org/cgi/doi/10.1149/1.2116607>.
93. H. Zhu and R. J. Kee, *J. Electrochem. Soc.*, **153**, A1765–A1772 (2006) <http://jes.ecsdl.org/cgi/doi/10.1149/1.2220065>.

94. Y. Shi et al., *ECS Trans.*, **7**, 1889–1899 (2007)
<http://ecst.ecsdl.org/cgi/doi/10.1149/1.2729301>.
95. Y. Shi et al., *J. Electrochem. Soc.*, **155**, B270–B280 (2008)
<http://jes.ecsdl.org/cgi/doi/10.1149/1.2825146>.
96. C. Li, Y. Shi, and N. Cai, *J. Power Sources*, **195**, 2266–2282 (2010)
<http://linkinghub.elsevier.com/retrieve/pii/S0378775309018552>.
97. P. Hofmann and K. D. Panopoulos, *J. Power Sources*, **195**, 5320–5339 (2010)
<http://linkinghub.elsevier.com/retrieve/pii/S0378775310003046>.
98. R. Mohammadi, M. Ghassemi, Y. Mollayi Barzi, and M. H. Hamed, *J. Solid State Electrochem.*, **16**, 3275–3288 (2012)
<http://www.springerlink.com/index/10.1007/s10008-012-1762-z>.
99. L. A. Barrales Mora, *2D and 3D Grain Growth Modeling and Simulation*, Cuvillier Verlag, Göttingen, (2008).
100. X. Guo and J. Maier, *J. Electrochem. Soc.*, **148**, E121 (2001)
<http://jes.ecsdl.org/cgi/doi/10.1149/1.1348267>.
101. F. E. G. Henn, R. M. Buchanan, N. Jiang, and D. A. Stevenson, *Appl. Phys. A Mater. Sci. Process.*, **60**, 515–519 (1995).
102. R. A. De Souza and J. Maier, *Faraday Discuss.*, **134**, 235 (2007)
<http://xlink.rsc.org/?DOI=b602914k>.
103. S. P. S. Badwal and J. Drennan, *J. Mater. Sci.*, **22**, 3231–3239 (1987).
104. W. Schmickler and E. Santos, *Interfacial Electrochemistry*, p. 94, Springer, Heidelberg, (2010).
105. N. L. Robertson and J. N. Michaels, *J. Electrochem. Soc.*, **138**, 1494–1499 (1991)
<http://jes.ecsdl.org/cgi/doi/10.1149/1.2085814>.
106. G. Jose La O, J. Hertz, H. Tuller, and Y. Shao-Horn, *J. Electroceramics*, **13**, 691–695 (2004).
107. J. L. Gland, *Surf. Sci.*, **93**, 487–514 (1980).
108. X. Xia, R. J. Oldman, and C. R. A. Catlow, *J. Mater. Chem.*, **22**, 8594–8612 (2012) <http://xlink.rsc.org/?DOI=c2jm16604f>.
109. J.-H. Park and R. N. Blumenthal, *J. Electrochem. Soc.*, **136**, 2867 (1989)

- <http://link.aip.org/link/JESOAN/v136/i10/p2867/s1&Agg=doi>.
110. J. O. Bockris and Z. Nagy, *J. Chem. Educ.*, **50**, 839–843 (1973)
<http://dx.doi.org/10.1021/ed050p839>.
111. J. M. Thomas and W. J. Thomas, *Principles and Practice of Heterogeneous Catalysis*, 2nd ed., John Wiley & Sons, Hoboken, (2015).
112. H. P. Bonzel and R. Ku, *Surf. Sci.*, **40**, 85–101 (1973)
<http://linkinghub.elsevier.com/retrieve/pii/0039602873900538>.
113. J. Jiang and J. L. Hertz, *J. Electroceramics*, **32**, 37–46 (2013)
<http://link.springer.com/10.1007/s10832-013-9857-1>.
114. D. R. Lide, Ed., *CRC Handbook of Chemistry and Physics*, 84th ed., CRC Press, Boca Raton, Fla., (2003).
115. P. Valentini, T. E. Schwartzenruber, and I. Cozmuta, *Surf. Sci.*, **605**, 1941–1950 (2011) <http://dx.doi.org/10.1016/j.susc.2011.07.005>.
116. R. Lewis and R. Gomer, *Surf. Sci.*, **12**, 157–176 (1968).
117. P. Zhang, Y. Y. Lau, and R. S. Timsit, *IEEE Trans. Electron Devices*, **59**, 1936–1940 (2012).
118. G. Chiodelli, L. Malavasi, V. Massarotti, P. Mustarelli, and E. Quartarone, *Solid State Ionics*, **176**, 1505–1512 (2005)
<http://linkinghub.elsevier.com/retrieve/pii/S0167273805000962>.
119. J. H. Joo and G. M. Choi, *J. Eur. Ceram. Soc.*, **27**, 4273–4277 (2007)
<http://linkinghub.elsevier.com/retrieve/pii/S0955221907001847>.
120. D. Pérez-Coll, P. Núñez, J. R. Frade, and J. C. C. Abrantes, *Electrochim. Acta*, **48**, 1551–1557 (2003)
<http://linkinghub.elsevier.com/retrieve/pii/S0013468603000276>.
121. I. Kosacki, C. M. Rouleau, P. F. Becher, J. Bentley, and D. H. Lowndes, *Electrochem. Solid-State Lett.*, **7**, A459–A461 (2004)
<http://esl.ecsdl.org/cgi/doi/10.1149/1.1809556>.
122. A. Karthikeyan, C.-L. L. Chang, and S. Ramanathan, *Appl. Phys. Lett.*, **89**, 2–5 (2006) <http://scitation.aip.org/content/aip/journal/apl/89/18/10.1063/1.2385211>.
123. M. Sillassen et al., *Adv. Funct. Mater.*, **20**, 2071–2076 (2010)
<http://doi.wiley.com/10.1002/adfm.201000071>.

124. J. Jiang, X. Hu, W. Shen, C. Ni, and J. L. Hertz, *Appl. Phys. Lett.*, **102**, 143901 (2013) <http://scitation.aip.org/content/aip/journal/apl/102/14/10.1063/1.4801649>.
125. T. Suzuki, I. Kosacki, and H. U. Anderson, *Solid State Ionics*, **151**, 111–121 (2002).
126. L. Chen et al., *Appl. Phys. Lett.*, **83**, 4737 (2003) <http://scitation.aip.org/content/aip/journal/apl/83/23/10.1063/1.1629378>.
127. J. Mizusaki, K. Amano, S. Yamauchi, and K. Fueki, in *Chemical sensors*, T. Seiyama, Editor, p. 277, Elsevier, Amsterdam (1983).
128. R. Hartung, *Zeitschrift für Phys. Chemie*, **260**, 259–272 (1979).
129. J. Fontanella and R. L. Johnston, *J. Non. Cryst. Solids*, **31**, 401–414 (1979).
130. J. Fontanella, C. Andeen, and D. Schuele, *J. Appl. Phys.*, **45**, 2852–2854 (1974) <http://scitation.aip.org/content/aip/journal/jap/45/7/10.1063/1.1663690>.
131. A. K. Harman, S. Ninomiya, and S. Adachi, *J. Appl. Phys.*, **76**, 8032–8036 (1994) <http://scitation.aip.org/content/aip/journal/jap/76/12/10.1063/1.357922>.
132. J. Fleig, H. L. Tuller, and J. Maier, *Solid State Ionics*, **174**, 261–270 (2004) <http://linkinghub.elsevier.com/retrieve/pii/S0167273804004801>.

Appendix A

MATLAB CODE

```
% Import data
filename = 'impedance.csv';
delimiterIn = ',';
headerlinesIn = 5; % Comsol files have 5 header lines
A = importdata(filename,delimiterIn,headerlinesIn);

% Find number of rows [s(1)] and columns [s(2)]
s = size(A.data);

% Find number of frequencies
nf = 1;
for b = 1:s(1)-1
    if A.data(b,1) ~= A.data(b+1,1)
        nf = nf + 1;
    end
end

% Dimension array to hold impedance output
z = zeros(nf,3);

% Set input marker
inp = 0;

for c = 1 : nf

    length = 1;

    % Find number of data points for frequency f
    while length < s(1) && A.data(length,1) == A.data(length+1,1)
        length = length + 1;
    end

    % Initialize t,v,j
    t = zeros(length,1);
    v = zeros(length,1);
```

```

j = zeros(length,1);

f = A.data(inp+1,1);

%Read in t,v,j
for a = 1 : length
    t(a) = A.data(inp+a,2);
    v(a) = A.data(inp+a,3);
    j(a) = A.data(inp+a,4);
end

tf = t(length);

%Perform FFT
jff = fft(j);
vff = fft(v);
zff = vff./jff;
zffr = real(zff);
zffi = imag(zff);
freq = zeros(length,1);

for a = 1 : length
    freq(a) = (a-1)/tf; % (a-1)*2*pi/tf for angular freq
    margin = 0.1/tf; % 10% of frequency step
    if f < freq(a)+margin && f > freq(a)-margin
        z(c,1) = f;
        z(c,2) = zffr(a);
        z(c,3) = zffi(a);
    end
end

%Plot (optional)
plot(freq,abs(zff))
hold on

inp = inp + length;

end

```

Appendix B

PERMISSIONS FOR REPRINTED MATERIAL

Portions of this dissertation were reprinted from B. E. McNealy and J. L. Hertz, *Solid State Ionics*, **256**, 52–60 (© 2014), with permission from Elsevier.

ELSEVIER LICENSE TERMS AND CONDITIONS

Aug 17, 2017

This Agreement between Benjamin McNealy ("You") and Elsevier ("Elsevier") consists of your license details and the terms and conditions provided by Elsevier and Copyright Clearance Center.

License Number	4170941050498
License date	Aug 16, 2017
Licensed Content Publisher	Elsevier
Licensed Content Publication	Solid State Ionics
Licensed Content Title	On the use of the constant phase element to understand variation in grain boundary properties
Licensed Content Author	Benjamin E. McNealy, Joshua L. Hertz
Licensed Content Date	Mar 1, 2014
Licensed Content Volume	256
Licensed Content Issue	n/a
Licensed Content Pages	9
Start Page	52
End Page	60
Type of Use	reuse in a thesis/dissertation
Intended publisher of new work	other
Portion	full article
Format	both print and electronic
Are you the author of this	Yes

Elsevier article?	
Will you be translating?	No
Title of your thesis/dissertation	Interpreting impedance spectra of thin-film electrochemical cells: A two-dimensional numerical modeling study
Expected completion date	Sep 2017
Estimated size (number of pages)	192
	Benjamin McNealy 5118 Holmes St
Requestor Location	PITTSBURGH, PA 15201 United States Attn: Benjamin McNealy
Publisher Tax ID	98-0397604
Total	0.00 USD

Portions of this dissertation were were reprinted from B. E. McNealy, J. Jiang, and J. L. Hertz, *J. Electrochem. Soc.*, **162**, F537–F546 (2015). This is an open access article distributed under the terms of the Creative Commons Attribution 4.0 License (CC BY 4.0) which permits unrestricted reuse of the work in any medium, provided the original work is properly cited.

Figure 9 was reprinted from J. Fleig, *J. Electroceramics*, **13**, 637–644 (© 2004 Kluwer Academic Publishers) with permission of Springer.

SPRINGER LICENSE
TERMS AND CONDITIONS

Aug 17, 2017

This Agreement between Benjamin McNealy ("You") and Springer ("Springer") consists of your license details and the terms and conditions provided by Springer and Copyright Clearance Center.

License Number	4170940832402
License date	Aug 16, 2017
Licensed Content Publisher	Springer
Licensed Content Publication	Journal of Electroceramics
Licensed Content Title	Impedance Spectroscopy on Solids: The Limits of Serial Equivalent Circuit Models
Licensed Content Author	J. Fleig
Licensed Content Date	Jan 1, 2004
Licensed Content Volume	13
Licensed Content Issue	1
Type of Use	Thesis/Dissertation
Portion	Figures/tables/illustrations
Number of figures/tables/illustrations	1
Author of this Springer article	No
Order reference number	
Original figure numbers	Figure 2
Title of your thesis / dissertation	Interpreting impedance spectra of thin-film electrochemical cells: A two-dimensional numerical modeling study
Expected completion date	Sep 2017
Estimated size(pages)	192
Requestor Location	Benjamin McNealy 5118 Holmes St

Billing Type	PITTSBURGH, PA 15201 United States Attn: Benjamin McNealy Invoice Benjamin McNealy 5118 Holmes St
Billing Address	PITTSBURGH, PA 15201 United States Attn: Benjamin McNealy
Total	0.00 USD

Figure 10 was reprinted from J. Fleig, P. Pham, P. Sztulzaft, and J. Maier, *Solid State Ionics*, **113–115**, 739–747 (© 1998) with permission from Elsevier.

ELSEVIER LICENSE
TERMS AND CONDITIONS

Aug 17, 2017

This Agreement between Benjamin McNealy ("You") and Elsevier ("Elsevier") consists of your license details and the terms and conditions provided by Elsevier and Copyright Clearance Center.

License Number	4170931463138
License date	Aug 16, 2017
Licensed Content Publisher	Elsevier
Licensed Content Publication	Solid State Ionics
Licensed Content Title	Inhomogeneous current distributions at grain boundaries and electrodes and their impact on the impedance
Licensed Content Author	J. Fleig,P. Pham,P. Sztulzaft,J. Maier
Licensed Content Date	Dec 1, 1998
Licensed Content Volume	113
Licensed Content Issue	n/a
Licensed Content Pages	9
Start Page	739
End Page	747
Type of Use	reuse in a thesis/dissertation
Portion	figures/tables/illustrations
Number of figures/tables/illustrations	1
Format	both print and electronic
Are you the author of this Elsevier article?	No
Will you be translating?	No
Original figure numbers	Figure 8
Title of your thesis/dissertation	Interpreting impedance spectra of thin-film electrochemical cells: A two-dimensional numerical modeling study
Expected completion date	Sep 2017

Estimated size (number of pages)	192
	Benjamin McNealy 5118 Holmes St
Requestor Location	PITTSBURGH, PA 15201 United States Attn: Benjamin McNealy
Publisher Tax ID	98-0397604
Total	0.00 USD